Independent Research

Investigation of different roof strengthening methods to gain an elastically responding roof in static and dynamic rollover tests

Alexander Schmitt

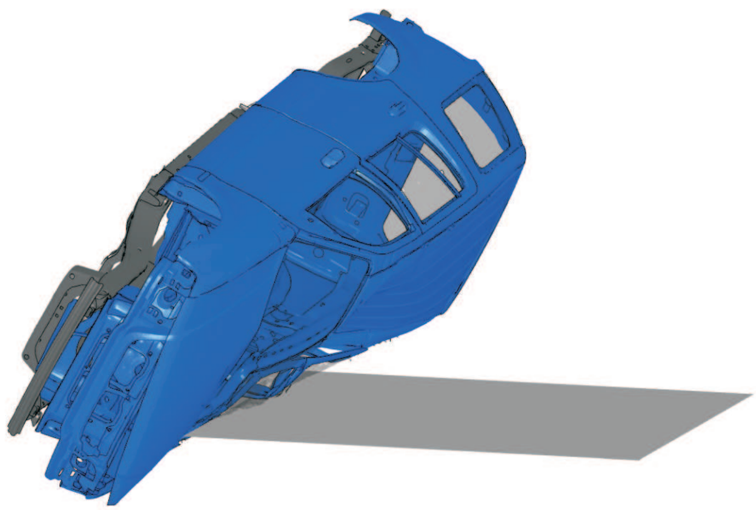

The School of Engineering and Applied Science
of The George Washington University

Advisor: Dr. Kennerly Digges

August 31, 2009

Acknowledgments

First of all, I want to thank Prof. Dr.-Ing. habil. Eberhard Roos from the Institut für Materialprüfung, Werkstoffkunde und Festigkeitslehre (IMWF) at the University of Stuttgart for the opportunity to participate in in the exchange program with the National Crash Analysis Center (NCAC) at The George Washington University. I also want to thank Dr. Cing-Dao Kan, the director of the NCAC, as the organizer of the exchange program at the GWU. They organized this integrated study abroad program with the financial support of the Deutscher Akademischer Austausch Dienst (DAAD). I learned a lot during this year, this was a great and unique experience for me.

I am especially indebted to Dr. Kennerly Digges as the advisor of my research, as well as Randa Radwan Samaha, Dr. Pradeep Mohan and Dr. Dhafer Marzougui, who always took the time for me to solve the problems I had with my research. Without your help this research report wouldn't exist in this form. Furthermore, I want to thank the whole team of the NCAC, who created a welcoming atmosphere and made the work a very enjoyable part of my stay.

I want to thank the Insurance Institute for Highway Safety for supporting my research by donating me a roof section of a Volkswagen Tiguan; and the ThyssenKrupp Steel AG for giving me material data cards, which I could apply to my reinforcement iterations.

I would also like to thank my family for their support of my stay in America, and especially my sister Katrin Schmitt for editing this report. All of you helped me making this stay a pleasant and successful one.

Last but not least I want to thank Boris Thaser and Daniel Seifert, my fellow students from the University of Stuttgart. It was a lot of fun to work together with you, and you were always helpful and supportive for my work. The time we spent together outside the university was a really great time.

Abstract

Although rollovers are a rare event – only 3 % of all car crashes are rollovers – over 10,000 people every year are killed in rollovers. SUVs are more likely to roll over, because they have a high center of gravity, so their roof has to be particularly strong to prevent occupant injuries from an intruding roof.

A good performance in dynamic rollover crashes requires an elastically responding roof during the impact of the leading side. Most contemporary vehicles' roof is too weak to withstand this impact without major plastic deformation. Various methods have been used by car manufacturers to improve the roof strength. Using the Finite Element Model of a 2003 Ford Explorer, three different methods are investigated in this research: Advanced high strength steel application in combination with continuous welding methods, rigid foam fillings and steed tube insertions.

The improved vehicle models are simulated in the quasistatic FMVSS 216 roof crush test and the dynamic Jordan Rollover System (JRS). The JRS simulations are performed with 5° pitch angle, the variation to 10° pitch angle will also be investigated. Furthermore, the roof of a Volkswagen Tiguan is investigated, material tests are performed, to determine the material properties of a state-of-the-art vehicle's roof. This material data is applied to the Finite Element model as well.

Contents

List of Figures

List of Tables

List of Graphs

1 Introduction

Rollovers are a rare event on US roads - according to the National Highway Traffic Safety Administration NHTSA [8], in 2002 only 3 % of all accidents were accidents, in which at least one of the involved vehicles rolled over [8]. An accident is called rollover, when the vehicle rolled for at least 90 degrees. Although rollovers are such a rare event, 33% of all car crash fatalities, more than 10,000, were caused in rollovers.

Despite its high fatality rate, rollovers are generally low-speed events. In only 10% of all rollover events the vehicle rolled more than one quarter-turn, the vertical speed is typically 2.5 $^{m}/_{s}$ or less [9], which would cause not more than minor injuries. On the contrary, the roofs of dynamically tested vehicles intruded into the passenger compartment with an intrusion speed exceeding 4.5 $^{m}/_{s}$, which is likely to cause fatal neck injuries. A strong roof, withstanding high forces in a rollover, would consequently reduce the risk of head and neck injuries caused by rapidly intruding roof sections.

At the present time the Federal Motor Vehicle Safety Standard 216 (FMVSS 216) regulates the roof strength of vehicles with a gross weight of less than 2,722 kg. This standard requires a vehicle's roof to withstand the force of 1.5 times the vehicle curb weight (Strength to Weight Ratio SWR = 1.5) with an intrusion of less than 127 mm when statically loaded by a rigid plate. This standard was recently updated, now the vehicle roof is to withstand 3.0 times the vehicle curb weight on both sides. However, the compliance to this standard is optional until 2012.

The Insurance Institute for Highway Safety (IIHS) performs the same tests for consumer information purposes and recently added a roof strength criterion for their safety rating. The roof crush resistance is classified similar to the other crash tests, a vehicle with a SWR of less than 2.5 receives a “poor” rating, a vehicle with a higher SWR than 4 receives a “good” rating. This is the only present rollover safety test that evaluates the strength of the roof.

The New Car Assessment Program (NCAP), the crashworthiness rating program of NHTSA, also rates vehicles in respect of rollover safety, but evaluates only the Static Stability Factor (SSF), the ratio of half the track width divided by the height of the center of gravity. This gives no information about the actual ability of the vehicle to protect the occupants in a rollover.

In addition to the static roof crush test, which neglects the influence of the dynamic behavior of the vehicle, the JRS system was developed in 2002. This system tests the vehicle by rotating and simultaneously dropping it on a moving roadbed. The vehicle sustains an impact on both roof sides, hence representing a real world crash better. Because it is a dynamic test, the cars can be equipped with crash test dummies measuring injury-related values and estimate, how well the occupants are protected by the roof structure and how well restraint systems protect the occupants. The JRS test is not yet used in safety regulations or consumer information systems.

In this research the influence of an elastically behaving roof during the near side impact will be investigated and various roof strengthening methods will be tested at the finite element model of a 2002 Ford Explorer model, which was developed at the National Crash Analysis Center’s Vehicle Modeling Laboratory. The effectiveness of the roof strengthening methods will be evaluated based on injury-related values and the improvement of stiffness, compared to the weight and amount of costly material added to the roof. Furthermore the structural components of the roof of a Volkswagen Tiguan, the best performer in the actual IIHS roof crush test series, will be investigated. Tensile tests will be performed to determine the material properties of the steels used in a state-of-the-art vehicle. The obtained material data will be applied to the Explorer roof and the strengthening effects evaluated.

2 Theory

2.1 Finite element theory

2.1.1 Basic equations of the finite element method

Most modern technical problems are too complex to find analytical solutions for them. Approximate numerical solutions have to be found instead. The probably most common method used for engineering applications is the finite element method, which dates back to the 1950s. With this method the complex problem is discretizised into many small, simple areas, for which a mathematical ansatz exists. For example, to find a solution for a complexly shaped metal part, the ansatz functions for the finite elements describe the momentum equation

$$\sigma_{ij,j} + \rho f_i = \rho \ddot{x}_i$$

with the traction boundary condition

$$\sigma_{ij} n_j = t_i(t)$$

the displacement boundary conditions

$$x_i(X_\alpha, t) = D_i(t)$$

and the contact boundary conditions

$$(\sigma_{ij}^{+} - \sigma_{ij}^{-})\, n_i = 0$$

This means, that at the boundary of each element either a traction, i.e. an external force, of a displacement is given, or, when it shares its boundary with another element, the contact boundary condition describes the stress interaction between the elements.

The ansatz functions yield to a matrix element formulation, and together with the boundary conditions the element matrices are combined to a global set of linear equations. This system is of the form

$$[M]\{\ddot{x}(t)\} = [F_{external}(t)] - [F_{internal}(t)]$$

Time discretization divides the total duration of the problem into small pieces, the time steps. Many numerical methods exist to perform the time integration of this problem. In general, they can be grouped into implicit and explicit methods. Explicit methods require only the actual state to calculate a time step, hence the next time step can be calculated explicitly. The general expression of an explicit formulation is

$$x(t + t_s) = x(t) + t_s\, f(x(t))$$

An implicit formulation would be of the form

$$x(t + t_s) = x(t) + t_s\, f(x(t + t_s))$$

which requires, applied on the problem described above, either an iterative process to solve the problem, or a matrix inversion. Both methods have their advantages and disadvantages: while the explicit formulation requires very small time steps, which can be calculated very fast, the implicit methods require less time steps, but they are expensive to calculate.

Due to the very small time step size, explicit calculation is unsuitable for static analysis, because the calculation time would get very large. Implicit analysis provides a better performance in this case. Other options to calculate static problems are mass scaling and time scaling in combination with explicit calculation method. When inertial effects get negligible, the mass can be increased without having an influence on the results. Hence the time step can be increased, and calculations of a longer duration can be calculated. Time scaling is simply running the simulation in a shorter time period, so that the calculation time becomes acceptable. This may of course result in inertial effects, but for certain applications they are negligible.

2.1.2 LS-DYNA code

LS-DYNA is a simulation software package developed by the Livermore Software Technology Corporation and was originally developed for military purposes in 1976 by John Hallquist at the Lawrence Livermore National Laboratory. Since then, the software was developed to simulate impact mechanics and highly nonlinear problems. The material library includes a large collection of non-elastic materials. The explicit calculation method, an effective contact algorithm and the capability to calculate large deformations makes this software suitable for crash analysis, which is one of its largest areas of application. The software includes many automobile crash specific elements like seatbelt accelerometers, dummies or airbag models.

2.2 Characteristics of a rollover crash

A rollover is a rare event with a high probability of injury or death, this suggests the assumption that rollovers occur a high impact velocity and high impact forces. However, real world crash statistics have shown, that only ten percent of all rollover crashes roll more than one turn; and rollovers usually occur at low impact speeds. Rollovers can be initiated by different events: The vehicle can be hit laterally in an preceding event; abrupt driving maneuvers can cause a rollover even without hitting any objects, especially vehicles with a high center of gravity and without electronic stability control are susceptible to this crash mode. However, the most frequent reason for a rollover accident is that the vehicle gets tripped, for example by a guard rail, in soft soil (when the vehicle went off road) or any other roadside obstacle, that can trip the wheels and allow the vehicle to roll over it.

When a vehicle begins rolling over, its center of gravity is lifted above the track of the wheels, and as long as the lateral speed is high enough at this point, the vehicle makes more than one quarter turn and one side of the roof has its first contact with the road. The center of gravity decreases at this point, and this impact, the near-side impact, is a less severe event, because the center of gravity can continue to decrease, when the vehicle rolls on its roof. At this point the center of gravity has to be lifted again, and because the other side, the far side, has to support the load of the vehicle and the additional force to lift the center of gravity, this impact is the more severe impact.

Because the height of the vehicle's center of gravity is so important for the likelihood to roll over, the static stability factor (SSF) is used by NCAP to evaluate the likelihood to roll over. The SSF is calculated as $\text{SSF} = \frac{0.5 \times \text{Track Width}}{\text{Height of COG}}$. Hence a high, narrow vehicle has a low SSF and a low, wide vehicle has a high SSF. However, since many contemporary cars are equipped with electronic stability control and many other factors like tires and suspension also contribute to the likelihood of rollover, this factor is only a rough estimate of the rollover probability and doesn't evaluate the roof strength at all.

The roof shape itself also contributes to the severity of the roof impact [10, p. 1]. A round-shaped roof reduces the forces of a far-side impact, because the center of gravity is kept higher between the near-side and far-side impact. A possible approach to reduce the severity of the far-side impact is the HALO-system, which was shown to improve the roof performance significantly in the JRS test [10, p. 10]. This system consists of a round-shaped framework on the vehicle roof, which ensures a certain distance between the roof and the roadbed.

2.3 The quasi-static FMVSS 216 roofcrush test

In 1971, the National Highway Safety Bureau (NHSB) proposed the FMVSS 216 standard [1], which requires the roof of a vehicle with a gross weight of less than 2,722 kg to withstand a 1.5 times its own vehicle curb weight. The test is a quasistatic test, performed with a rigidly fixed vehicle, the load is applied with a rigid plate that crushes the roof on either side of the vehicle. The test setup is shown in Figure 2.1. The loading device measures 762 mm $\times$ 1,829 mm, its middle forward edge is located 254 mm forward of the forward-most point of the roof. The plate is positioned with a 5° pitch angle and a 25° roll angle to the horizontal. Beginning with initial contact, the plate is lowered 254 mm normal to the plate surface with a maximum speed of 13 $^{mm}/_{s}$. To pass the test, the force on the plate has to exceed 1.5 times the vehicle curb weight within 127 mm of plate deflection.

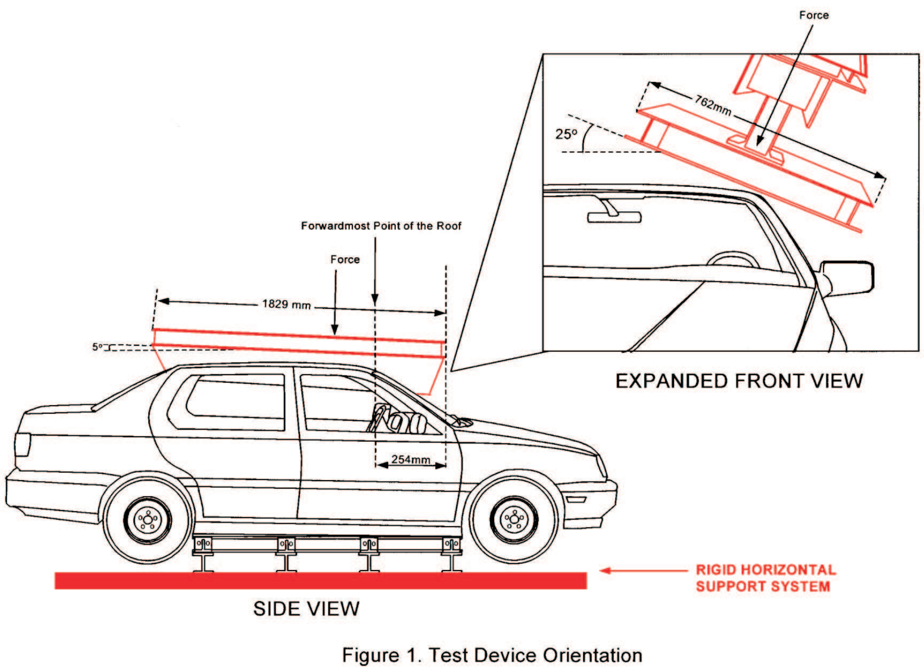

Figure 2.1: FMVSS 216 test setup [1]

The standard was upgraded on May 12, 2009, and takes effect stepwise until 2015. The standard now requires the roof to be tested on both sides, and the plate load has to exceed three times the vehicle curb weight. The vehicle is tested first on one side, then on the other side, and on both sides the plate must not lower more than 127 mm to reach the required force.

However, the plate angles were not changed in the new rule. This is considered as a too low angle [9, p. 8], because a low plate angle shifts the load to the B-pillar, and a vehicle, that has a strong B-pillar (e.g. to improve side impact performance), can pass the test with a relatively weak A-pillar. Investigations of real world crashes also have shown, that the hood and/or the bumper was damaged on vehicles that rolled over, and hence, considering the geometry of the car, the impact must have occurred at an angle of about 10 degrees.

In 2009, IIHS began to perform FMVSS 216-tests for consumer information ratings. The test setup is the same, but the vehicle has to withstand a higher force in order to earn a good rating. A roof with a higher SWR than 4 is rated as "good", a SWR between 3.25 and 4 earns an "acceptable" and between 2.5 and 3.25 a "marginal". A vehicle with a SWR below 2.5 is rated as "poor".

2.4 The Jordan rollover system (JRS)

The Jordan Rollover System was developed in 2002 to evaluate the dynamic rollover performance of vehicles. The system has been proven to be repeatable [11], which was not confirmed for other dynamic rollover test devices. The big advantage of this system is, that it is possible to equip the test with anthropometric test devices to measure injury loads directly and hence determine, how well occupants are protected in rollovers. Besides the option to measure the injury values with dummies, the dynamic intrusion and intrusion speed can be measured with string potentiometers; the load from the vehicle on the road can be measured as well, the load that actually causes the roof to crush. Intrusion speed is linked to neck injury, so the injury probability can be determined as a function of intrusion speed. An intrusion speed above 16.1 $^{km}/_{h}$ is likely to cause fatal injuries, an intrusion speed above 11.3 $^{km}/_{h}$ is likely to cause serious injury [9].

The rollover device is made of a test vehicle fixture that keeps the vehicle fixed laterally and longitudinally, and a laterally moving roadbed that is mechanically connected to the rotating vehicle. A picture and a drawing of the test setup are shown in Figure 2.2 and Figure 2.3. The vehicle and the roadbed are inertially matched, and the roadbed is driven pneumatically. The towers on each side of the vehicle keep the car above the roadbed prior to the test, as soon as the roadbed starts to go under the vehicle, the vehicle is released, rolls over and is afterwards caught again by the towers to prevent further damage to the vehicle. The roadbed is equipped with load cells, which measure the force from the vehicle on the roadbed.

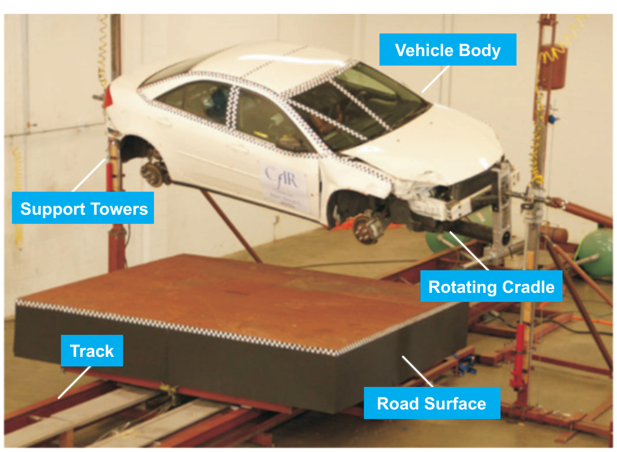

Figure 2.2: Picture of the JRS setup prior to test [2]

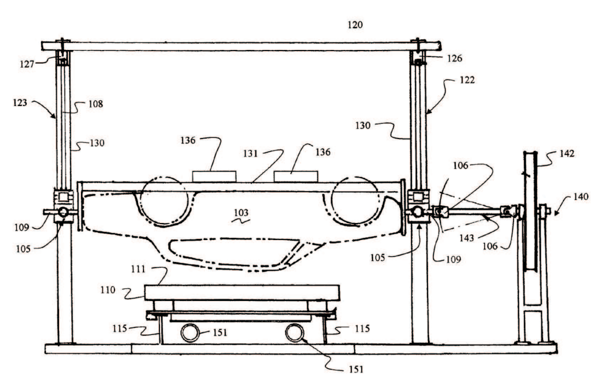

Figure 2.3: Drawing of the JRS setup [3]

Table 2.1: JRS initial conditions

Initial condition	Value	High Pitch Simulation
Rotational Speed	190 $^{deg}/_{sec}$	190 $^{deg}/_{sec}$
Vertical Drop Distance	10 cm	10 cm
Roadbed Speed	24.2 $^{km}/_{h}$	24.2 $^{km}/_{h}$
Roll Angle at Impact	145°	145°
Pitch Angle	5°	10°
Yaw Angle	10°	10°

2.5 Actual approaches to increase the roof strength of cars

2.5.1 High-strength steel solution

The structural components of a contemporary car is mostly made of advanced high strength steels (AHHS), which provide a high yield strength combined with high plasticity to absorb crash energy, and are usable in automotive production processes. The most important steels developed during the last decades are TRansformation Induced Plasticity (TRIP) steels, Dual Phase (DP) steels, Complex Phase (CP) steels, martensitic phase steels, manganese-boron steels, interstitial free (IF) steels and high strength low alloy (HSLA) steels. Especially martensitic phase steels and manganese-boron steels are used in roof strengthening applications due to their very high yield strength (>1000 MPa).

Martensitic Phase Steels

Martensitic steels are hot-rolled steels, which can be cold-formed and are mainly used in crash-relevant structures like bumper beams, door beams, and pillar reinforcements. The yield strength of these steels is usually above 900 MPa and the tensile strength above

1200 MPa. Since the fracture elongation is only around 5 %, these steels are applied rather to prevent intrusion than to absorb crash energy, which makes them suitable for roof strengthening applications.

Manganese Boron Steels

Manganese boron steel is another martensitic steel with a very high tensile strength. With addition of small amounts of boron (<0.003 %) the temperability increases and the presence of boron-atoms in the crystal lattice cause precipitation hardening, thus increasing the tensile strength. This steel requires different processing than the martensitic phase steels: While MS-steels are hot-rolled and cold-formed at room temperature, manganese boron steels reqire hot stamping. In this process the steel is heated above austenitizing temperature prior to forming, and quenched while in the forming tool. Cold forming prior to the hot stamping can be performed to realize more complex part geometries. This process allow adjusting the material properties to the required values and also allows to have different material properties in one part by realizing different cooling rates within the stamping tool. The typically achievable mechanical properties after processing are a yield limit of 1100 MPa and a tensile strength of above 1500 MPa, the fracture elongation is around 5 %.

2.5.2 Laser welding technology

Laser welding technology is a welding method using a focused, continuous laser beam to join different parts of sheet metal. This laser beam melts the layers of sheet metal in a tube-shaped section, and since the laser beam is moving continuously, the sheet metal is welded together when the molten metal solidifies.

Compared to conventional resistance spot welding, laser welding technology has several advantages:

- A continuous weld seam is possible, thus larger joint surfaces are possible.
- The parts have to be accessible only from one side, compared to resistance spot welding, which requires access to the parts from both sides. This makes laser welding suitable for box-shaped parts, for example at the side roof rails, as shown in Figure 2.4.
- The laser beam can weld with less room, that makes it easier to weld hardly accessible parts.
- Laser welding requires no contact between the tool (The focusing unit) and the parts.

2.5.3 Application of roll cages

Another approach to reinforce the roof is the application of a roll cage to the vehicle body. Although complete roll cages are usually only used in cars prepared for professional racing sport, many contemporary production vehicles have components reinforced with tube-shaped structures. Especially the windshield of convertibles is reinforced, because it has to withstand high forces during a rollover due to the missing connection between the A-pillar and the B-pillar. The B-pillars of a convertible usually end at the side windowsill, so

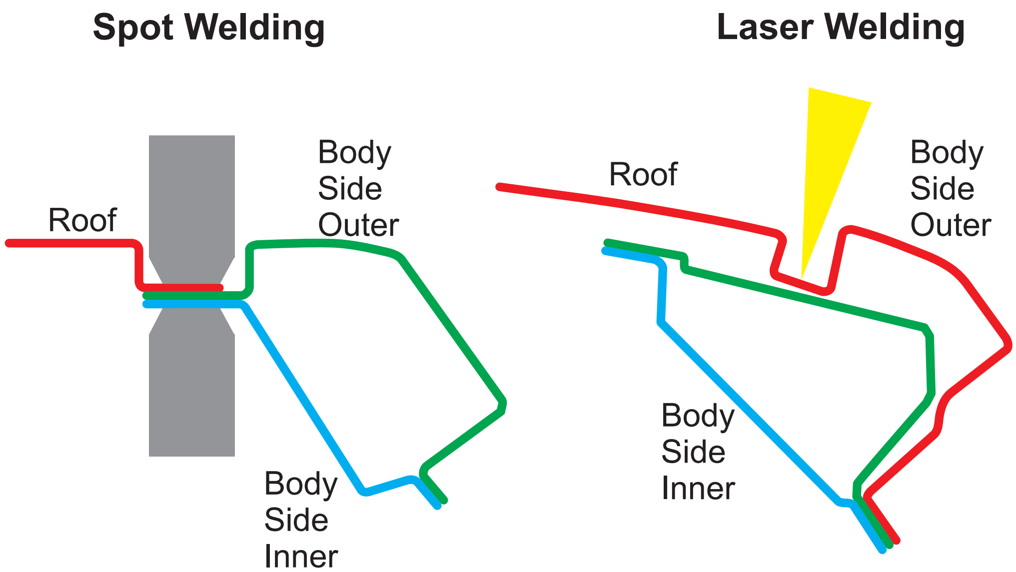

Figure 2.4: Laser welding application at a side roof rail [4]

most convertibles of all price ranges have roll hoops installed, which automatically deploy during a rollover crash. A very high vehicle with a high rollover probability may also profit from an installation of a roll cage, and it may be an attractive and inexpensive solution to reinforce the roof or at least parts of it.

A typical roll cage as it is purchasable for almost all currently sold cars, is made of either heat-treated 25CrMo4-steel or conventional construction steel. These materials are used, because roll cages are usually made of tubular semi-finished parts and welded or screwed. Since these roll cages are built into cars to either prepare them for racing purposes or only for optical purposes, they are assembled completely inside the vehicle as a separate structure and not integrated into the structure of the car.

2.5.4 Rigid foam solution

Rigid foams can be applied into the supporting structures of the roof to prevent collapsing of these parts. Rigid foam fillings have proven to increase the roof strength significantly with a moderate increase of the vehicle weight [12]. Two commonly used types of rigid foam fillings are polyurethane foam fillings or nylon-composite structures. The application can be performed either as a bulk solution or as preformed structural foam inserts. Bulk foam is a convenient method for small cavities, because it can be injected through small holes; and since the density can be adjusted by the composition of the material, various stiffness grades can be reached. Structural foam inserts are preformed parts, so they have to be included during the assembly of the surrounding body parts. A positive fitting is gained during the bake-hardening process, when the expandable outer layer of the insert fills the gap between the insert and the surrounding sheet metal. The advantage of foam inserts is the option to create non-uniform shapes like a rib-structure, which was used for this study.

3 Applied Software

3.1 LSTC LS-PrePost 2.4 and 3.0 beta

LS-PrePost is a free preprocessor and post-processor especially designed to create keyword input files for LS-DYNA. It is developed by the Livermore Software Technology Corporation, the developer of the LS-DYNA-code used for the simulations of this research. The 2.4 release is the current final release of the software, but for this report the 3.0 beta version was preferably used. The 3.0 version offers a new, more intuitive user interface instead of the keyword management interface of the former versions, as well as a new geometry processing environment. LS-PrePost is proprietary freeware and can be retrieved from LSTC's FTP download server.

3.2 Altair HyperWorks 9.0

Mainly for mesh creation and mesh editing the HyperWorks 9.0 Suite from Altair Engineering was used. The finite element pre-processor HyperMesh provides powerful meshing tools as well as quality index tools and was preferably used to create and edit the finite element model. A LS-DYNA I/O-interface is included in the software, so HyperMesh can be used parallel to other pre-processors.

3.3 CorelDRAW Graphics Suite X4

To visualize the simulation results and to optimize pictures and graphs, the vector graphics editor CorelDRAW from Corel Corporation was used. This is a common software used for vector-based illustrations. Corel PHOTO-PAINT, the bitmap editor included in this software suite, was used for bitmap editing and optimization.

3.4 Notepad++

Notepad++ is a powerful GNU-licensed source editor. Since a lot of input file editing had to be done manually, and the standard Windows XP Notepad is unusable for such applications, this software was used instead. It provides syntax-highlighting, which is very useful for the LS-DYNA keyword format; and also includes efficient macro-tools.

4 The 2003 Ford Explorer and its FE-Model

After the production of the Ford Bronco II was terminated in 1990, Ford introduced the Ford Explorer as a mid-sized Sport Utility Vehicle (SUV) in 1990. Since then, the Ford Explorer became a highly sold vehicle in the United States and is a commonly seen vehicle on US streets. The 2003 model is the third generation of the Ford Explorer, which was introduced in 2002 and replaced by the fourth generation in 2006.

The Ford Explorer is a light truck based car, and is built on a ladder frame. The ladder frame supports the engine and suspension, the vehicle body is connected to the ladder frame with ten body mounts. The vehicle gross weight with a 4.0 l-V6 engine and rear wheel drive is 2323 kg, the curb weight is 1863.2 kg. The dimensions are: length: 4800 mm, width: 1828 mm, height: 1803 mm.

Figure 4.1: Ford Explorer 2002 - 2005 model

4.1 The roof structure of the Ford Explorer

The Ford Explorer is a conventional 4-door vehicle, so the roof is supported by A-pillars and B-pillars that are connected with side roof rails. The side structures are connected with five roof rails; the most forward roof rail, the window header, is made of two layers of sheet metal, all other roof rails are single sheet metal pieces, except the most rearward roof rail, which also acts as a support for the hatch. The A-pillar consists of two layers as well, the B-pillar has an additional third reinforcement layer. The roof structure with the baseline material grades and gages is shown in Figure 4.2.

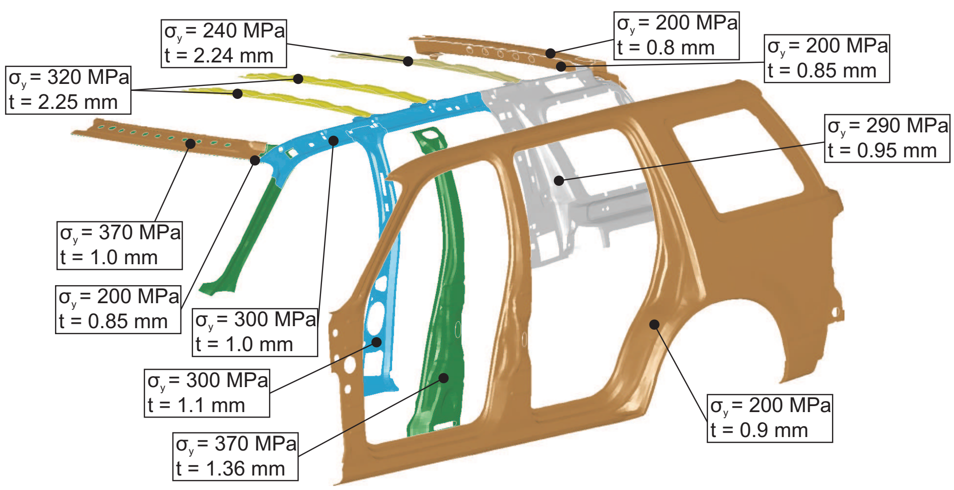

Figure 4.2: Material grades and gages of the Ford Explorer roof

4.2 The FE model developed by NCAC

In 2007, NCAC released a detailed finite element model of the 2003 Ford Explorer, which was digitized at its Virtual Modeling Laboratory. The model contains the car body, including all drive train, engine and suspension parts and the ladder frame, but no interior model. The full model is shown in Figure 4.3, the finite element mesh in Figure 4.4.

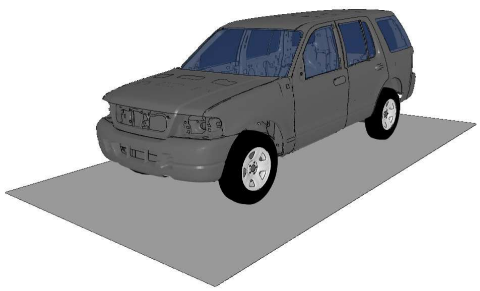

Figure 4.3: Full model of Ford Explorer NCAC-FE-model

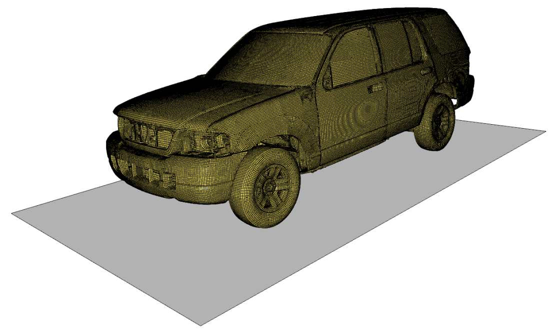

Figure 4.4: Full model of Ford Explorer NCAC-FE-model, elements shown

An overview of the characteristic values of the model is given in Table 4.1. The average element size is 12 mm - 15 mm, and the vehicle weight of the FE model is 2237.8 kg. The vehicle body is mounted to the ladder frame with ten body mounts, which are simulated with nonlinear springs in the model and calibrated to component tests performed at NCAC's Federal Outdoor Impact Laboratory. Their behavior is important in dynamic crash tests, because it affects the accelerations within the vehicle.

Table 4.1: Properties of the original Finite Element model [7]

Number of Parts	791
Number of Nodes	632166
Number of Elements	619161
Number of Shells	585418
Number of Beams	48
Number of Solids	33695

4.2.1 Original purpose of the model

The original purpose of the model is the simulation of frontal crash tests, and it is verified for the full frontal NCAP crash test at 55 km/h (35 mph). But since the geometry and the mesh are also detailed for the roof and pillar sections, roof crush studies are possible with this model. The material data for the FE model was derived from coupon tests, so the FE model of the roof should also be close to realistic behavior.

4.2.2 Model changes for rollover simulations

Further improvements have been made at the model to enhance its behavior and performance in rollover tests.

Material model improvements

Different material properties and gauges have been applied to the model in order to improve the realistic roofcrush performance:

Table 4.2: Material changes applied to the FE model

Part Number	Description	Original Gauge	New Gauge	Original Yield Strength	New Yield Strength
2000013	Roof cross member front	0.793 mm	0.85 mm	320 MPa	200 MPa
2000118	Roof rail reinforcement	0.98 mm	1.00 mm	200 MPa	370 MPa

Another improvement relates to the glass model used for all windows of the car. In the NCAP model the glass is simulated with an elastic material model without failure; this has of course little influence on the results since the window sections hardly deform in a frontal crash. However, the windows and the window frames experience large deformation in a roofcrush test, in most cases the windshield and the side windows break during the tests and hence no longer support the structure. The differences between these material models are listed in Table 4.3.

Table 4.3: Differences between glass model of original NCAP model and improved roofcrush model

Property	**Original Model**	**New Model**
Material Model	Elastic	Piecewise Linear Plastic
Failure Criteria	N/A	1% Plastic Strain
Young's Modulus Windshield	76 GPa	70 GPa
Poisson's Ratio Windshield	0.3	0.22
Young's Modulus Side and Rear Windows	76 GPa	74 GPa
Poisson's Ratio Side and Rear Windows	0.3	0.242
Yield Limit	N/A	50 MPa
Thickness of Windshield	4 mm	2×3 mm
Thickness of Side and Rear Windows	3.9 mm	3.9 mm

Although glass is a brittle material, the piecewise linear plastic material in combination with a low plastic failure strain was chosen for the improvements, because the elastic material model in LS-DYNA doesn't support failure of the material. The windshield is made of laminated glass, but was simulated without a polymer layer and only with the two outer glass layers. A polymer layer was experimentally included in the model and was removed after it behaved unstable when the windshield failed. It was assumed that a polymer layer with less than 1 mm thickness doesn't support the structure significantly.

Performance improvements

In contrast to a frontal crash, many parts can be removed or simplified in the finite element model of a rollover crash to improve the performance of the model and hence run faster simulations. It was assumed that the suspension, drivetrain and engine compartment do not influence the strength of the roof, so these parts were removed for the static roofcrush test. The removal of these parts reduced the number of elements from 619161 to 420517 and reduced the simulation time from about 35 hours to about 24 hours on a 2 $\times$ 3 GHz Intel Core2Duo System.

The weight and inertia of the vehicle has of course a great influence on the behavior in a dynamic rollover test. Therefore the mass and inertia was calibrated by adding concentrated mass and inertia to six points at the ladder frame. LS-DYNA provides the element *ELEMENT_INERTIA_OFFSET for this purpose. The inertial properties of the removed parts was determined and divided into an engine / front suspension, transmission and rear suspension section. These sections were applied to nodes at the mounting points of the engine, transmission and rear suspension. Then the nodes were fixed to the ladder frame using rigid bodies. A comparison between the full model and the reduced model are shown in Figure 4.5 and Figure 4.6.

After removal of the parts the vehicle weight was reduced from 2237.8 kg to 719.7 kg, the moment of inertia dropped by around 50 %. The exact values of the vehicle inertias and the added inertial elements are listed in Table 4.4. After calibration of the inertial properties the vehicle were very close to the properties of the original model, and hence it can be assumed, that the original model and the reduced model behave equally in the dynamic rollover test.

Table 4.4: Inertial properties of the original and reduced vehicle model

<table>
<tr><th colspan="2">Description</th><th>Mass</th><th>I_{11}</th><th>I_{22}</th><th>I_{33}</th></tr>
<tr><td colspan="2">Full vehicle model</td><td>2237.8 kg</td><td>725.97 kg m^2</td><td>3805.4 kg m^2</td><td>4063.8 kg m^2</td></tr>
<tr><td colspan="2">Reduced vehicle model</td><td>719.7 kg</td><td>374.5 kg m^2</td><td>1291.6 kg m^2</td><td>1419.3 kg m^2</td></tr>
<tr><td rowspan="6">Added Masses</td><td>Front Left</td><td>303 kg</td><td colspan="3">Coordinates:
x = -112 mm; y = -315 mm; z = 79 mm
Inertia:
$\begin{pmatrix} 80.4 & & \\ -1.03 & 23.72 & \\ -1.95 & -2.25 & 56.9 \end{pmatrix}$ kg m^2</td></tr>
<tr><td>Front Right</td><td>303 kg</td><td colspan="3">Coordinates:
x = -112 mm; y = 375 mm; z = 108 mm
Inertia:
$\begin{pmatrix} 80.4 & & \\ -1.03 & 23.72 & \\ -1.95 & -2.25 & 56.9 \end{pmatrix}$ kg m^2</td></tr>
<tr><td>Middle Left</td><td>112.5 kg</td><td colspan="3">Coordinates:
x = 164 mm; y = 57 mm; z = 162 mm
Inertia:
$\begin{pmatrix} 22.8 & & \\ 9.52 & 93.96 & \\ -10.43 & 3.66 & 10.3 \end{pmatrix}$ kg m^2</td></tr>
<tr><td>Middle Right</td><td>112.5 kg</td><td colspan="3">Coordinates:
x = 156 mm; y = -13 mm; z = 161 mm
Inertia:
$\begin{pmatrix} 22.8 & & \\ 9.52 & 93.96 & \\ -10.43 & 3.66 & 10.3 \end{pmatrix}$ kg m^2</td></tr>
<tr><td>Rear Left</td><td>352 kg</td><td colspan="3">Coordinates:
x = 331 mm; y = -337 mm; z = -7 mm
Inertia:
$\begin{pmatrix} 81.3 & & \\ 47.27 & 160.1 & \\ -12.1 & -6.33 & 222.6 \end{pmatrix}$ kg m^2</td></tr>
<tr><td>Rear Right</td><td>352 kg</td><td colspan="3">Coordinates:
x = 344 mm; y = 302 mm; z = -11 mm
Inertia:
$\begin{pmatrix} 81.3 & & \\ 47.27 & 160.1 & \\ -12.1 & -6.33 & 222.6 \end{pmatrix}$ kg m^2</td></tr>
<tr><td colspan="2">Calibrated model</td><td>2254.7 kg</td><td>604.9 kg m^2</td><td>3884.0 kg m^2</td><td>4073.7 kg m^2</td></tr>
</table>

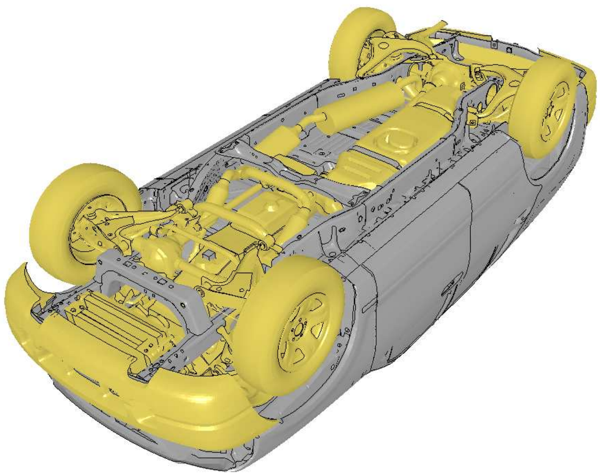

Figure 4.5: Full model of the Ford Explorer

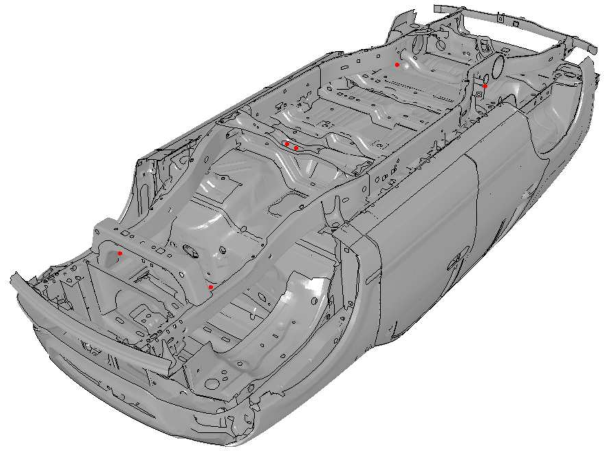

Figure 4.6: Reduced model of the Ford Explorer. The added masses and inertias are shown red

Ladder Frame Fixation

To gain more reproducible results and to run stable simulations, the ladder frame was rigidly fixed to the vehicle body. Since most of the weight is mounted at the ladder frame, the forces on the body joints tend to be very high, which may lead to an unstable behavior of the simulation. However, the deflections between the vehicle body and the ladder frame are small and hence it can be assumed that the fixation of the body joints has no influence on the simulation results. The FMVSS 216 rule already requires a rigidly fixed vehicle body, see Section 2.3. The fixation was realized by adding a rigid body to the body joints, at the same nodes where the nonlinear springs of the body joints are fixed to the body and ladder frame. A detailed view of a body joint is shown in Figure 4.7.

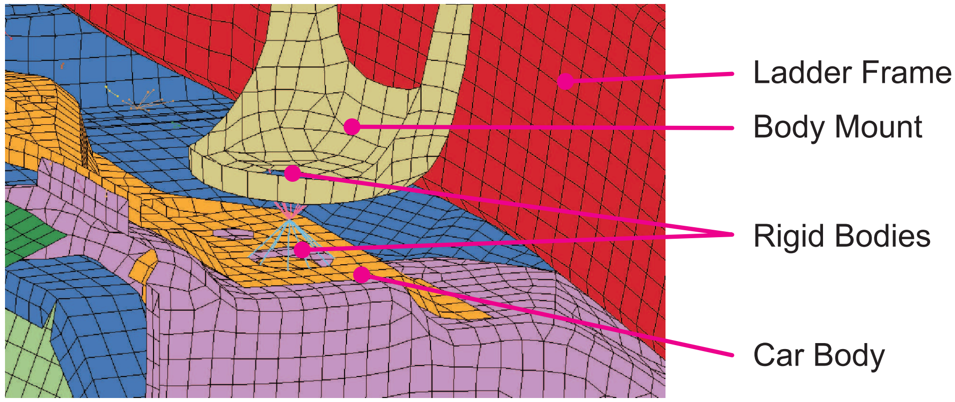

Figure 4.7: Fixed body joint between car body and frame rail

4.2.3 Realization of the rollover tests, simulation setup

4.2.3.1 The quasistatic test simulation

For the quasistatic roofcrush simulations the car was fixed in space at four points of the ladder frame, using the *BOUNDARY_SPC_SET keyword in LS-DYNA. This keyword fixes all nodes listed in the associated nodal set. This is similar to the test setup of test 0139 (see Section 4.2.4); for this test four vehicle stands were welded to the frame rails, and the vehicle movement was prevented by chains attached to the ladder frame. Test and simulation are compared in Figure 4.8 and Figure 4.9.

The loading device was simulated as a rigid wall moving with constant speed, using the LS-DYNA keyword option *RIGIDWALL_GEOMETRIC_FLAT_MOTION. The wall speed was set to 1 $^{m}/_{s}$, which leads to a simulation time of 254 ms; and had the dimensions given in FMVSS 216 (see Section 2.3). The plate did not have contact in the initial state to prevent initial penetration of car parts with the wall, which can lead to high nodal velocities and

Figure 4.8: Vehicle Stand in Roofcrush Test 0139 [5]

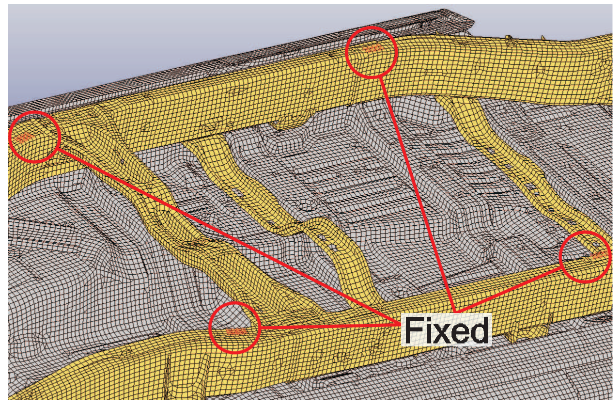

Figure 4.9: Fixed Nodes in FE-Simulation

hence instabilities during the first step. The simulation setup with the rigid wall is shown in Figure 4.10.

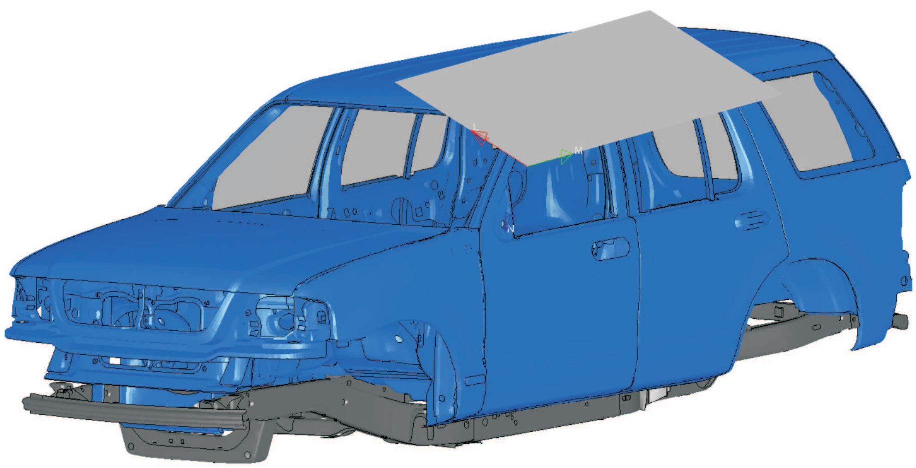

Figure 4.10: FMVSS 216 simulation setup, rigid wall shown

Time-shifting was used to simulate this quasi-static test, because it was the only stable solution method for this problem. The other two options terminated during the first calculation step, hence turning out to be unusable:

- The most common option for quasi-static simulations is the so-called mass-scaling. This method adds mass to the model to allow longer time steps without making the simulation unstable. This option terminated right after initialization with out-of-range velocity errors in some solid parts, probably caused by the contact algorithm, because the errors occurred, where solid elements and contact elements (null-material elements [13, p. 1446]) share the same nodes.

- Another option is the implicit calculation method, which requires much less time steps than the explicit calculation method, usually about 100 to 10000 times less. The calculation time per time step is unknown beforehand and depends on the convergence of the problem, but since the static roofcrush test is a low speed event, a good convergence would have been very likely. Unfortunately the solver terminated even with the baseline model, after some memory allocation errors occurred. The reasons for such errors are of course not resolvable for the user, so the option of implicit calculation was not pursued further.

To determine the influence of the time-shifting, four different simulations with a duration of 0.254 s, 0.5 s, 1.0 s and 2.5 s were performed with adjusted wall speed in each case. A possible influence of the time-shifting should lead to different simulation results. The rigidwall force of the load plate was used to compare the simulations, and the rigidwall force showed only minor differences between the simulation time. A longer simulation time tends to a slightly lower rigidwall force, which is caused by the strain rate effects included in the material model. However, the simulation is closer to the real force-displacement curve with the strain rate effects included in the model (see Section 6.1.3, so they were retained in the model and the simulation time was also retained at 0.254 s.

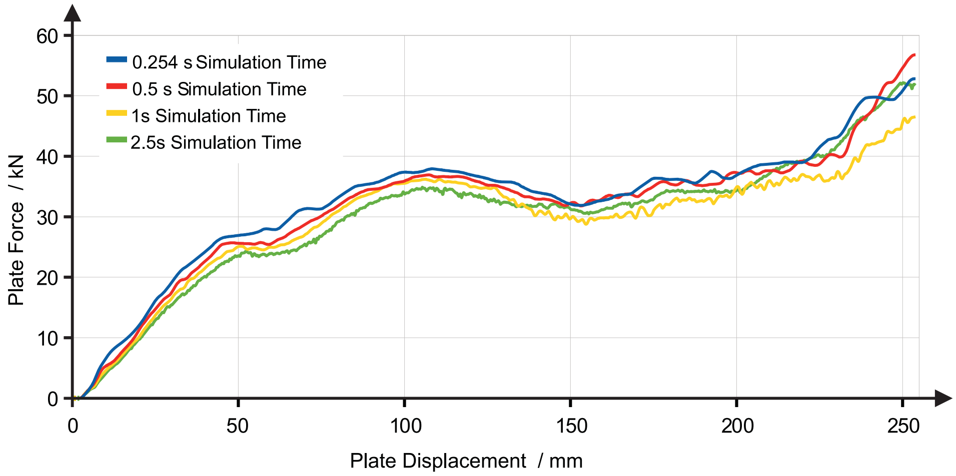

Graph 4.1: Comparison of different simulation times

4.2.3.2 The JRS test simulation

The JRS rollover test was set up according to the standard initial conditions, given in Table 2.1. The drop height was transformed into an initial vertical velocity and the gap between the vehicle roof and the roadbed was minimized to reduce calculation time, but a small gap was allowed to prevent initial penetration. The roadbed was also simulated using the *RIGIDWALL_GEOMETRIC_FLAT_MOTION-keyword, the rigid wall was given a initial velocity along its surface. The simulation time was set to 350 ms, at this time the vehicle has undergone its second impact, reached a roll angle of about 240 degrees and rolled over the end of the roadbed, hence no further load is applied to the roof. In the real test, the vehicle is afterwards caught by brakes at the fixation towers to prevent further damage to the roof and the test device. The full simulation setup is shown in Figure 4.11.

Longitudinal and lateral fixations were not implemented in this simulation, although the JRS rollover system includes them [3, p. 1]. The main purpose of these fixations is to support the vehicle in the initial state and to ensure that the vehicle remains within the test system and causes no damage after the rollover test by stopping the vehicle movement. It was assumed that these fixations have only minor influence on the vehicle behavior and this effect can be neglected in the simulations.

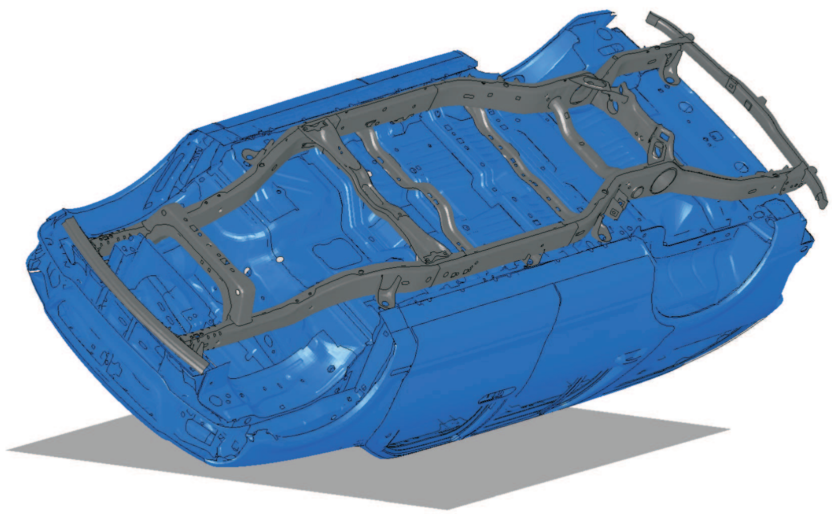

Figure 4.11: JRS rollover test setup, with roadbed shown

4.2.4 Validation of the FE model with the FMVSS 216 test 0139 (TRC)

On January 22, 2003 a FMVSS 216 roofcrush test was performed at the Transportation Research Center in East Liberty, Ohio. Subject was a 2002 Ford Explorer with a 4.0l - V6 engine, automatic transmission and rear wheel drive. The test was conducted according to the FMVSS 216 rule, the vehicle was rigidly fixed on the ground and the vehicle body was rigidly connected with the ladder frame. The load was applied with a hydraulic loading device at a plate speed of 7 $^{mm}/_{s}$, the plate was positioned with 5° pitch angle and 25° roll angle. The pre-test and post-test plate position is shown in Figure 4.12 and Figure 4.13

Ten test channels were recorded during the test. This includes the most important ones, the loading device force and the load plate displacement, as well as eight displacement transducers, which were positioned at either edge of the car and the opposite side sill, three transducers were attached to the roof, measuring the displacement of the roof point over a Hybrid III-50th male dummy in reference to a three-potentiometer array located at the place of the seat cushion of the driver's seat.

Figure 4.12: Pre-test load plate position [5]

Figure 4.13: Post-test load plate position [5]

5 Tensile Tests

The Insurance Institute for Highway Safety (IIHS) provided a roof section of a 2009 Model Volkswagen Tiguan, which was tested in a side impact crash test in July 2008. The roof section experienced only minor deformation during this crash test, hence the roof was usable for material testing. The post-test vehicle is shown in Figure 5.1, the roof as received at NCAC in Figure 5.2.

Figure 5.1: VW Tiguan side impact crash test vehicle, post test view, doors removed. [6]

Figure 5.2: Roof section used for material testing at the NCAC. [6]

5.1 The VW Tiguan roof strength

5.1.1 Reasons for testing the materials used in the VW Tiguan roof

In March 2009, IIHS launched a new roof strength rating system. The test for this rating is the same as the FMVSS 216 test (see Section 2.3). The first series of tests included ten small SUVs, and the VW Tiguan was proven to have the strongest roof among the tested vehicles, having a SWR of 5.6. A SWR of higher than 4 is rated as “good” by IIHS. Hardly any deformation was visible when the VW Tiguan was loaded with four times the vehicle weight, see Figure A.1. The method of failure was also a reason for testing the Tiguan roof: All vehicles failed with buckling of the A- and B-Pillar, except the VW Tiguan, its A- and B-Pillar remained stable and the roof began buckling, Figure A.2.

One reason for the high roof strength of the VW Tiguan may be the laser welded sections of the roof and A- and B-Pillars. The joint around the door (the seam that is covered by the rubber sealing of the door) is completely laser welded. All other cars have spot welds at these sections, and at failure the layers of sheet metal separated between the spot welds, as shown in Figure A.3, that shows the buckling point of the KIA Sportage B-Pillar, the only car with the worst rating (“poor”) in the test series.

5.1.2 Localization of specimens, manufacturing

21 tensile test specimens were retrieved from the roof section to gain material data, which were later applied to several reinforcements of the Ford Explorer roof. Specimens were taken from the A-pillar, B-pillar, window header and middle roof rail, if possible, three specimens were retrieved from each steel layer. The Sections used for the specimens are shown in Figure 5.3. After removing the weld joints, the specimens were laser cut, the specimen size was 0.6 mm according to ASTM E8M [14]. Except for the B-pillar all specimens were taken from flat parts of the metal layers; the three inner layers of the B-pillar

had many contours, which resulted in only six specimens of the B-pillar. An overview of the detailed specimen locations is given in Figure 5.4, and details about the performed tests in Table 5.1.

Table 5.1: List of tested specimens

Specimen no.	Location	Thickness	Notes
111, 112, 113	A-Pillar outer layer	0.7 mm - 0.8 mm	Specimen 113 contracted at two positions, which lead to higher fracture elongation
121, 122, 123	A-Pillar reinforcement layer	1.76 mm	
131, 132, 133	A-Pillar inner layer	1.5 mm	
211, 212, 213	B-Pillar outer layer	0.71 mm	
221, 222	B-Pillar outer reinforcement layer	1.74 mm - 1.78 mm	
231, 232	B-Pillar reinforcement, both layers	4.33 mm	Specimen 231 partially burned by laser cutter, not tested. Specimen 232 was partially cut through a spotweld, only tested to estimate the material grade of inner reinforcement layer
241	B-Pillar inner layer	1.69mm	
311, 312, 313	Roof front rail	1.01mm	
411, 412, 413	Roof B-Pillar rail	0.98mm - 0.99mm	

5.2 Test equipment and data acquisition

The tensile tests were performed with the universal testing machine “810 Material Test System” from MTS (Figure B.1). The system is hydraulically operated and allows tension tests with loads up to 100 kN. The measurable variables were the load force measured by a load

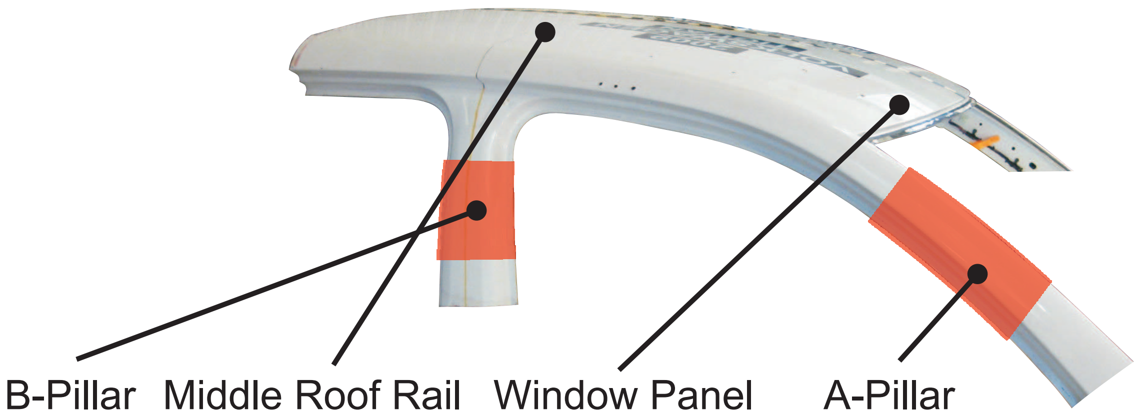

<u>Figure 5.3:</u> Location of sections used for tensile tests

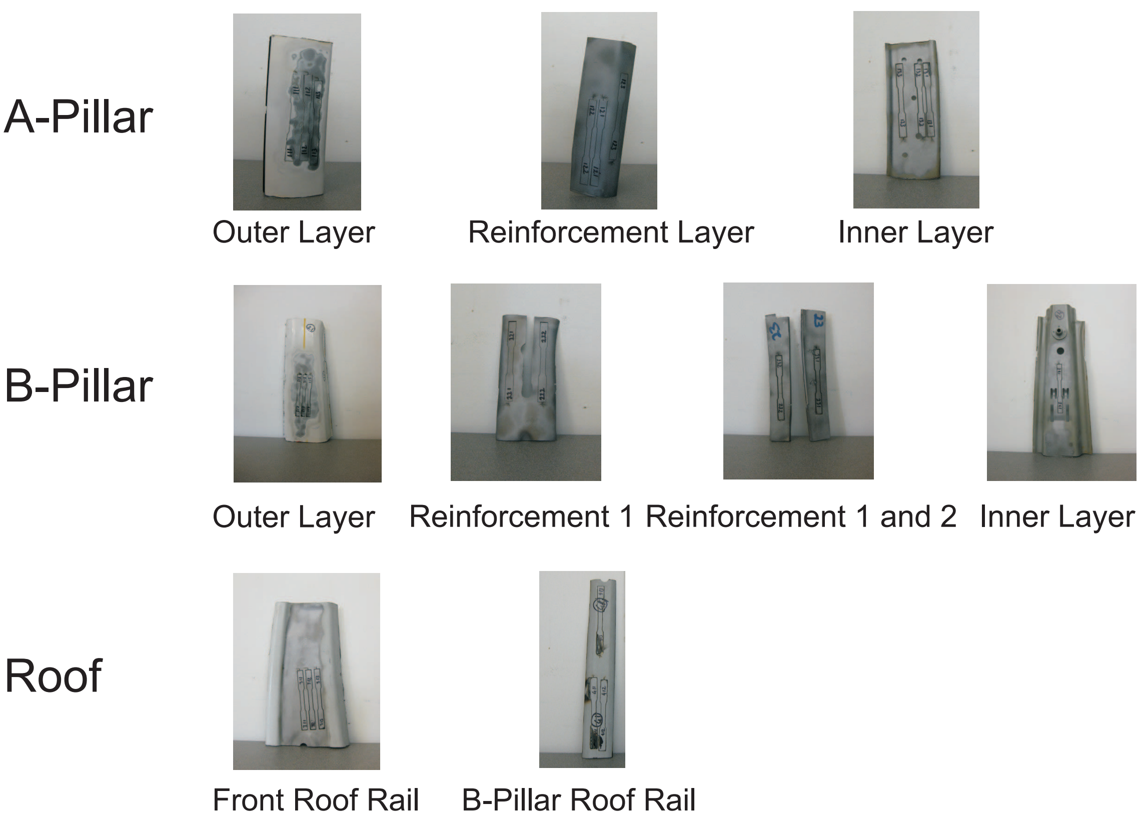

<u>Figure 5.4:</u> Location of specimens in the metal layers

cell above the specimen, and the displacement of the hydraulic actuator. Unfortunately no extensometers were available, so the specimen elongation could not be measured directly. The data was recorded by a multichannel data acquisition system and recorded with the test software "Teststar 2" from MTS.

All tests were performed with a constant actuator head speed of 0.05 $^{mm}/_{s}$ to ensure the quasistatic behavior of the materials. The load cell force and actuator displacement was recorded in 0.01 sec-steps. The initial gauge length of $l_0 = 2.54$ mm was marked on all specimens prior to testing to measure the fracture elongation.

5.2.1 Calculation of the specimen elongation

To calculate the correct actual gauge length of the specimen during the test, which is usually measured by a extensometer, the elongations of the machine, the grips and the sections of the specimen, that don't belong to the tested length, were subtracted from the measured displacement of the actuator. It was assumed that all parts except the tested section of the specimen behaved elastically. Hence follows for the specimen length:

$$l_1 = s_{\text{Actuator}} - \frac{F_{\text{Load Cell}}}{R_{\text{Machine}}} \tag{5.1}$$

Since R_{Machine} is different for every test, it has to be calculated out of the test data. Therefore it was assumed that the specimen behaves elastically during the first recorded steps, and that Young's modulus of steel is E = 210 GPa. Hence R_{Machine} can be calculated using Hooke's law:

$$\frac{F_{\text{Load Cell}} \cdot l_0}{A_{\text{Specimen}} \cdot E} + l_0 = s_{\text{Actuator}} - \frac{F_{\text{Load Cell}}}{R_{\text{Machine}}} \tag{5.2}$$

$$R_{\text{Machine}} = \frac{F_{\text{Load Cell}}}{s_{\text{Actuator}} - \frac{F_{\text{Load Cell}} \cdot l_0}{A_{\text{Specimen}} \cdot E} - l_0} \tag{5.3}$$

R_{Machine} was averaged for the first few steps, in which elastic behavior of the specimen can be certainly assumed. Then the actual gauge length of the specimen was calculated using Equation 5.1.

5.3 Test results

All performed tests showed valid and plausible results. No slip between the specimens and the grips occurred during the tests, and all specimens failed within the gauge length. The tested specimens are shown in Figure B.2. However, some factors may have caused errors in the results:

- The calculation of the actual gauge length may have caused errors, since the calculation of a constant machine resistance may neglect factors like plastic deformation of the specimen clamping, settling of the connection between the specimen and the grips, and play in different parts of the machine.
- The calibration of the machine and the test equipment was overdue, so the machine may not have been calibrated properly.
- The laser cutting of the specimens may have caused a heat treatment near the cut.

- The roof was taken apart with a disc cutter, this also may have caused heat treatment.

- The manually measured fracture elongation may be erroneous due to human error, especially since many specimens failed with a nearly pure shear fracture. This didn't result in a specified point of fracture in the recorded data. In this case the failure of the specimen was assumed at a drop of 20% of the tensile strength.

Since the measured data seems plausible and different tests of the same material showed similar results, the errors in these tests may be small.

5.3.1 Properties of tested materials

The material grades of the tested material varied from very high strength steel used in the reinforcements to medium strength steel used for the unibody. The characteristic values for all specimens are listed in Table 5.2.

Specimen 231 was tested like every other specimen. Since this specimen was cut through a spotweld, this is of course no valid tensile test. The specimen broke at the outer heat affected zone, which can be expected, since this is the weakest zone of a weld. But the maximum force achieved in this test can be used to estimate the steel grade of the second reinforcement layer of the B-pillar, since the steel grade of the other reinforcement layer is known. A maximum force of 32.3 kN was reached, so the second reinforcement layer has a similar steel grade as the first reinforcement layer.

Table 5.2: Results of Tensile Tests

Test no.	Location	Yield stress	Tensile Strength	Measured Fracture strain	Calculated Fracture strain	Uniform strain
111	A-Pillar outer layer	180 MPa	270 MPa	42.5%	46.8%	33%
112	A-Pillar outer layer	200 MPa	300 MPa	45.7%	52.2%	33%
113	A-Pillar outer layer	190 MPa	290 MPa	50.0%	56.9%	33%
121	A-Pillar reinforcement layer	1040 MPa	1420 MPa	10.2%	10.9%	6%
122	A-Pillar reinforcement layer	940 MPa	1420 MPa	10.2%	10.4%	5.5%
123	A-Pillar reinforcement layer	1010 MPa	1280 MPa	6.3%	8.4%	4%
131	A-Pillar inner layer	370 MPa	460 MPa	30.7%	30.9%	18%
132	A-Pillar inner layer	330 MPa	450 MPa	31.9%	32.5%	18%
133	A-Pillar inner layer	350 MPa	450 MPa	31.9%	31.0%	18%
211	B-Pillar outer layer	250 MPa	280 MPa	39.8%	39.8%	20%
212	B-Pillar outer layer	250 MPa	290 MPa	42.5%	42.4%	18%
213	B-Pillar outer layer	250 MPa	290 MPa	41.3%	40.4%	22%
221	B-Pillar outer reinforcement layer	1100 MPa	1460 MPa	3.5%	8.6%	4.8%
222	B-Pillar outer reinforcement layer	940 MPa	1430 MPa	3.2%	9.2%	5%
241	B-Pillar inner layer	380 MPa	430 MPa	29.9%	33.3%	22%
311	Roof front rail	380 MPa	470 MPa	29.5%	31.9%	18%
312	Roof front rail	390 MPa	470 MPa	29.9%	30.7%	20%
313	Roof front rail	370 MPa	460 MPa	30.3%	30.8%	18%
411	Roof B-Pillar rail	360 MPa	440 MPa	18.1%	19.4%	10%
412	Roof B-Pillar rail	390 MPa	480 MPa	18.9%	20.1%	10%
413	Roof B-Pillar rail	390 MPa	480 MPa	26.0%	27.3%	16%

The engineering stress-strain curves of all tested specimens are shown in Appendix B. The stress-strain curves of specimens taken from the same sections coincide very well in most cases, but the curves had a significantly lower tensile strength or different fracture elongation in three cases (Test 111, Test 123 and Test 413). The reason for the difference may be the the different locations of the specimens in the parts: Specimen 123 was located on a different side of the part (Figure 5.4), Specimen 413 was also located seperatly from the specimens 411 and 412. Specimen 111 may have a different tensile strength caused by higher plastic deformation during cold forming of the sheet metal.

The unibody (which is the A-pillar outer layer and the B-pillar outer layer) is made of a relatively soft high strength steel with a tensile strength of around 300 MPa, which may be a commonly used interstitial free (IF-) steel (e.g. the EN-standardized [15] HX160 steel), used for very deep-drawn parts like the unibody of a car.
The reinforcements of the A-pillar and B-pillar showed similar properties and may be made of the very high strength steel 22MnB5 or a MS steel like the standardized HDT1200M steel [16].

The inner layers of the A-pillar and B-pillar and both roof rails showed a behavior similar to a microalloyed steel like the HX340LA (standardized in [15]), which is a commonly used steel grade for body-in-white applications like pillars and rails.

5.4 Application of material data in LS-DYNA

To gain material data usable for finite element simulations, the true stress-strain curve has to be calculated. The engineering stress-strain curve cannot be used for finite element simulations, since it is related to the initial cross section of the specimen and hence doesn't represent the actual stress occurring in the material.

The true stress can be calculated with

$$\sigma_{\text{true}} = \text{k}_{\text{f}} = \sigma_{\text{eng}} \cdot (1 + \epsilon) \text{ [17, p. 4]}$$

and the true strain with

$$\epsilon_{\text{true}} = \varphi_{\text{f}} = \ln(1 + \epsilon) \text{ [17, p. 4]}$$

Since these equations are true only for uniform elongation, values above uniform elongation were not used for the material models. For implementation in LS-DYNA, the material model *MAT_PIECEWISE_LINEAR_PLASTICITY [13, p. 1504] was used. This material model allows the definition of an arbitrarily shaped stress-strain curve after yield limit by defining a stress-strain curve, the definition of a strain-based failure limit and strain-rate effects with the Cowper and Symonds model. This model uses two parameters to scale the yield stress depending on the strain rate. The equation is given as

$$1 + \left(\frac{\dot{\epsilon}}{\text{C}}\right)^{\frac{1}{\text{p}}} \tag{5.4}$$

Since the tensile tests were performed quasistatically, the Cowper and Symonds parameters were adopted from literature, Table 5.3.

Table 5.3: Cowper and Symonds parameters used for LS-DYNA material model

Steel Grade	TRIP Steel [18, p. 719]	DP Steel [18, p. 719]	MS / Boron Steel [19, p. 3]	IF steel [20]
C	11410.6	2211.9	6.2 e9	252.5
p	3.28	2.38	4.28	3.89

6 Simulation results and roof reinforcement

Based on the simulation setup described in Section 4.2.3 the baseline simulations were verified and relevant baseline simulation data acquired. Based on the verified model several reinforcements to the A-pillar, B-pillar and roof with different material grades and foam fillings were developed and their effectiveness tested. An improvement can be considered as effective, when the injury-related values, for example the loading-device force in the static roofcrush test or the intrusion speed in the JRS rollover test, increase or decrease significantly compared to the baseline results.

6.1 Baseline simulations and acquired simulation data

6.1.1 Static roofcrush simulation

The simulation described in Section 4.2.3.1 was run with 0.254 s simulation time and relevant simulation data acquired. The probably most important result of this test is the rigid wall force, which can be compared with the loading device force of the real test. The force-time curve was filtered using a SAE 60 Hz filter, and since the wall speed was chosen as 1 $^{m}/_{s}$, the resulting curve is automatically the force-displacement curve. A peak force of 37.96 kN was reached at a plate displacement of 108.8 mm. The force-displacement curve is shown in Graph 6.1. The curve decreases after a first peak force is reached and constantly increases afterwards to forces higher than 37.96 kN, but relevant is the first peak force, since the required roof strength in the FMVSS 216 rule is determined with the maximum force of the first 127 mm of plate displacement.

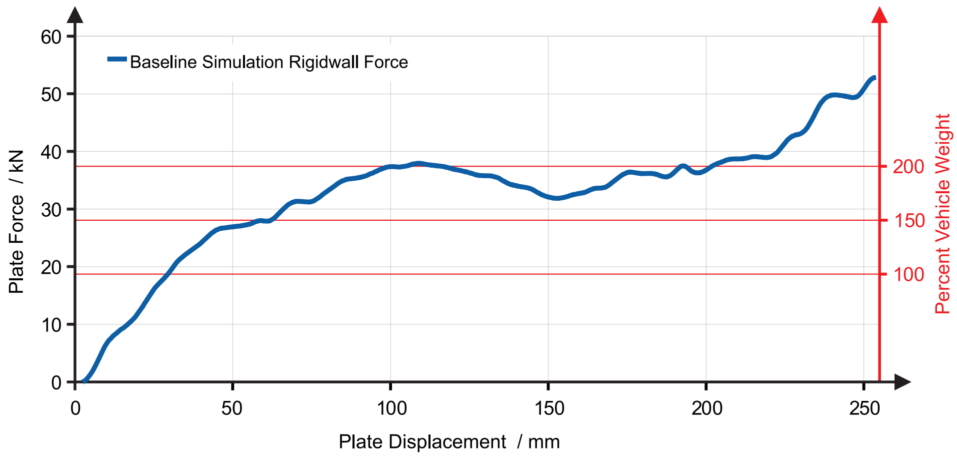

Graph 6.1: Rigidwall force of the baseline simulation

In addition to the rigidwall force section forces of the A-, B-, C- and D-pillars and the roof rails were acquired to determine, which parts of the roof structure support the roof and how these forces change during the test. For example, a buckling of the A- or B-pillar may yield to a drop of the rigidwall force, since the pillar(s) don't support the roof any more. Graph 6.2 shows very well that the normal section force curve of the A-pillar has the same shape like the rigidwall force until a plate displacement of about 150 mm. The B-pillar takes very little of the plate force, and already reaches a maximum at about 50 mm rigidwall displacement.

6.1.2 JRS simulation

The same vehicle as in the static roofcrush test has undergone the JRS simulation as described in Section 4.2.3.2. To determine the roof intrusion and intrusion speed, which are directly linked to head and neck injury, the nodal displacement and velocity of the near

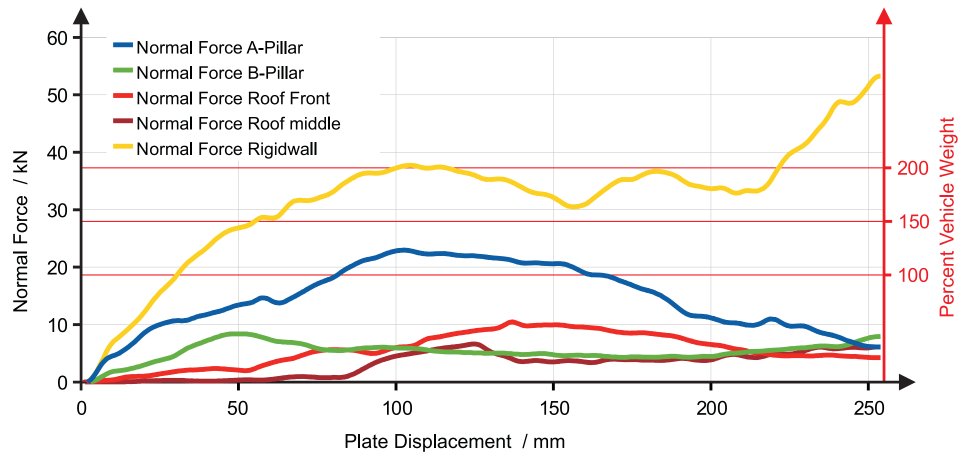

Graph 6.2: Section forces of the baseline simulation

side and far side roof line were generated. The resultant intrusion and intrusion speed of the far side and near side A-pillar and B-pillar was derived from this data, similar to the string potentiometer attachment points in the JRS test [10, p. 4]. This may result higher intrusion values, because the resultant intrusion is measured as the total deflection of a few nodes at the roof, whereas string potentiometers measure the distance between the attachment point and the potentiometer location. The resultant intrusion is always positive, since it is the absolute value of the nodal displacement vector. The normal force on the roadbed was also recorded, since it contains useful information about the actual load on the vehicle, as well as the height of the center of gravity, which provides the vertical movement of the vehicle. Like in the static test section forces of the A-pillar and B-pillar were generated during the simulation to determine, how much load was supported by the structural components of the roof. The intrusion, intrusion speed graphs are shown in Graph 6.3 and Graph 6.4, the roadbed normal force vs. center of gravity and the section forces are shown in Graph 6.5 and Graph 6.6.

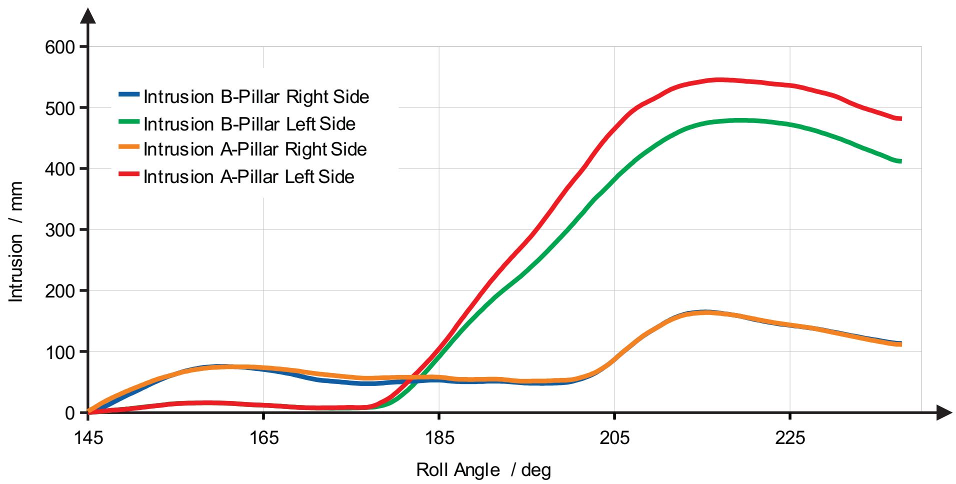

Graph 6.3: Resultant A-pillar and B-pillar intrusion of the baseline JRS simulation

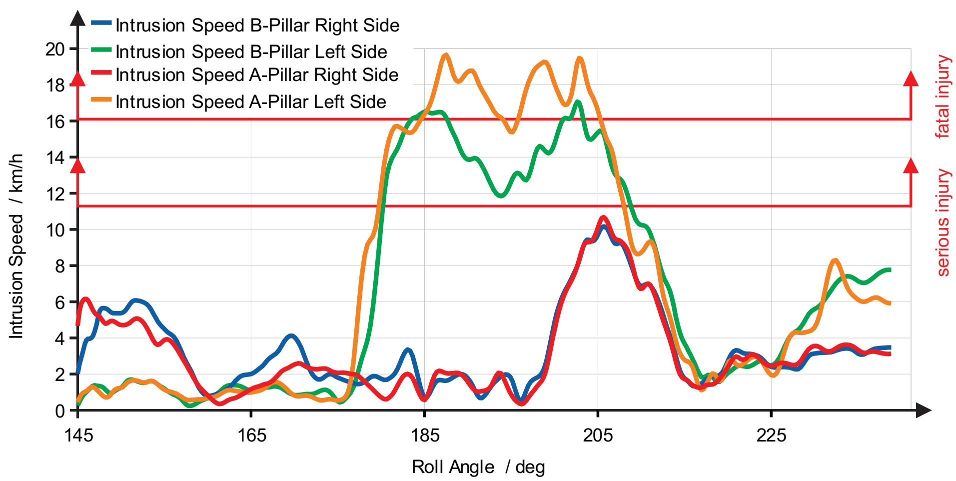

Graph 6.4: Resultant A-pillar and B-pillar intrusion speed of the baseline JRS simulation

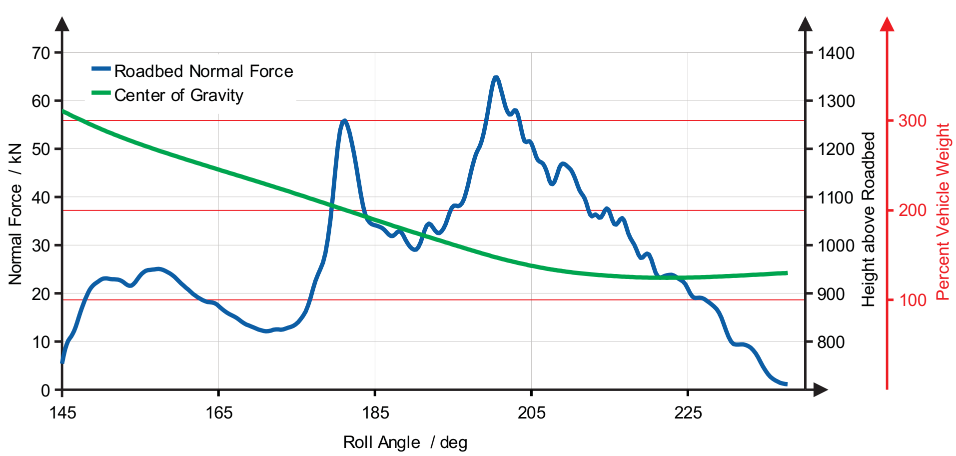

Graph 6.5: Roadbed force of the baseline JRS simulation

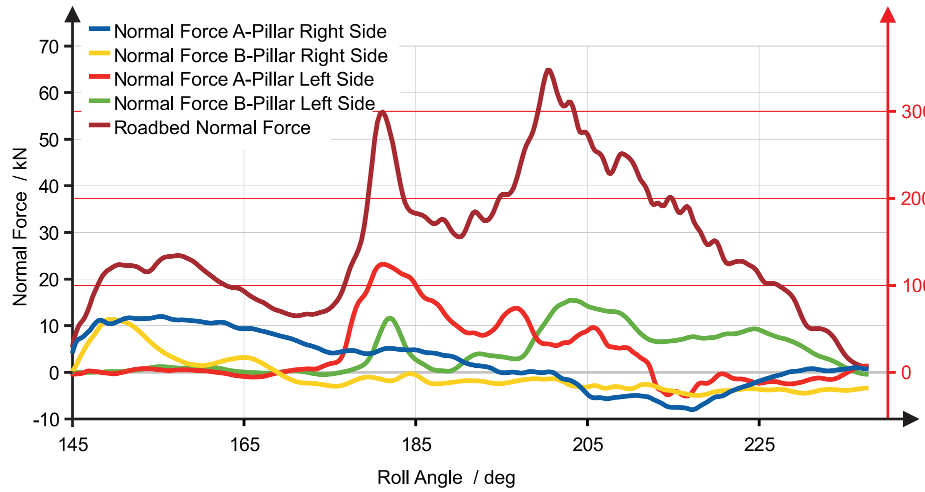

Graph 6.6: A-pillar and B-pillar section forces of the baseline JRS simulation

The roof shows very large intrusions at the impact of the driver side, the far side impact, going above 500 mm for the A-pillar at 215 degree roll angle. The passenger side (near side impact) shows less intrusion during the impact, going up to 80 mm at 160 degree roll angle. These intrusions appear to be very large, other vehicles that were tested in the JRS system and have a comparable low static roof crush resistance showed intrusions up to 213 mm (Jeep Grand Cherokee, [10, p. 9]) A-pillar intrusion during the first roll. Unfortunately the 2002 Ford Explorer model was not yet tested in the JRS system, so the results can not be compared to real test values. However, the way the roof crushes appears realistic, compared to other vehicles tested by the Center for Injury Research [2]; during the far side impact both the A-pillar and the B-pillar begin to buckle and the roof rail collapses into the headroom of the passengers. The post-simulation vehicle is shown in Figure 6.1, with the original shape of the vehicle shown in red. The largest intrusion appear around the far side A-pillar and windshield header connection, where the roof intrudes below the belt line of the vehicle. The B-pillar buckle point is similar to the buckle point of the static roof crush test (Figure 6.2) in the middle of the side windows. The window header does not buckle, however, the connections between the A-pillars and the window header allow the window header to intrude together with the left A-pillar and the roof rail. At the end of the rollover simulation the whole car body began to skew at the firewall, this is visible at the difference between the original shape and the post-test location of the left front fender. This effect may be smaller in a real rollover test, because the FE-model does not include the interior of the vehicle, but especially around the dashboard the interior parts may support the structure and result in a less skewed firewall.

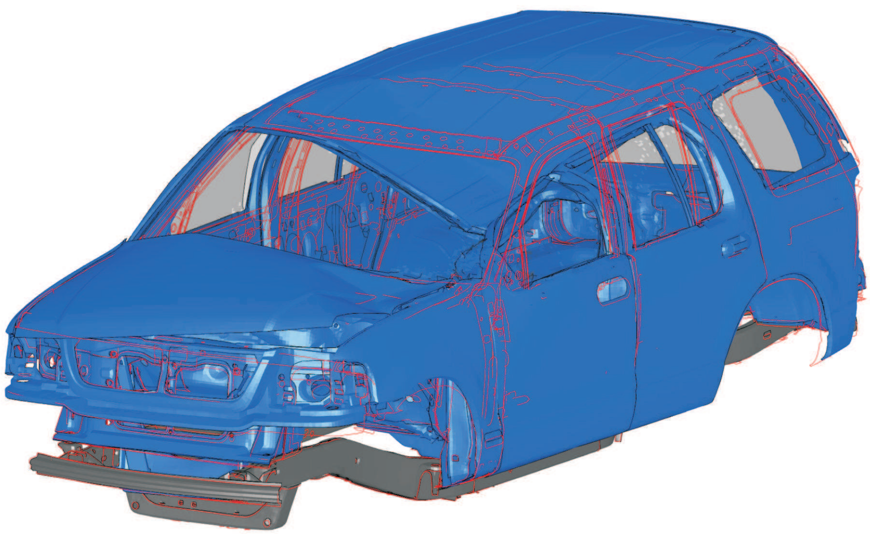

Figure 6.1: Deformed vehicle body after JRS rollover simulation, original shape red

A view of only the structural components is shown in Figure D.1, the interior view with the skewed firewall in Figure D.2. A comparison of the pre- and post-simulation car body shapes at the driver's body position is given in the section cut in Figure D.3, allowing a detailed view on the intrusion directions and roof buckling.

6.1.3 Verification of the static simulation with the test 0139 (TRC)

To determine, whether the simulation gives realistic results, the simulation data of the static roof crush test was compared with the test results of the FMVSS 216-test no. 0139 [5]. The loading device force over device displacement of the test was compared with the rigid wall force over rigid wall displacement of the simulation and are shown in Graph 6.7. The roof point displacement of the test was compared with the displacement of the corresponding node of the simulation in Graph 6.8. To gain comparable results for the roof displacement, the relative displacement of the node to the fixed points located at the potentiometer array mounted at the driver's seat cushion.

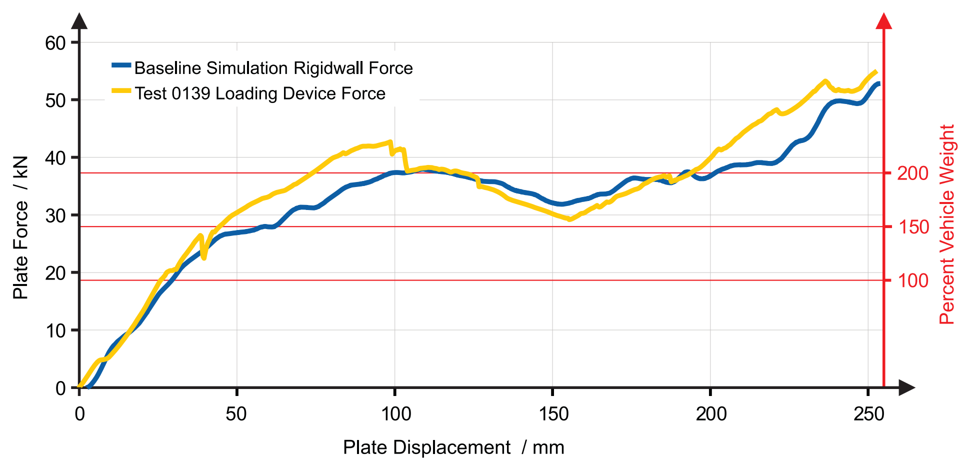

Graph 6.7: Rigidwall force vs. loading device force

The rigidwall force shows a good correlation with the loading device force, with a slightly lower force between 50 mm displacement and 100 mm displacement. This may be caused by too mild material properties or by the glass model, which results in continuous failure of the windshield between 50 mm displacement and 100 mm displacement, although the

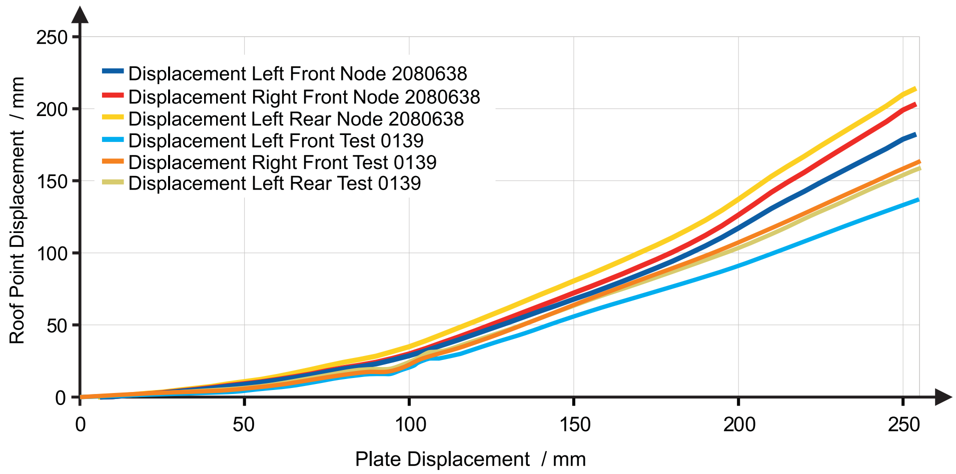

Graph 6.8: Roof point displacement, simulation vs. test

windshield in the real test begins to fail at about 50 mm displacement. A better glass model may lead to better results, but would require determining the exact properties of the used glass materials and their mountings.

The roof point displacement shows about 25% less displacement in the test than in the simulation, but the shapes of the curves are very similar. The higher displacement of the simulation is very likely resulted by different buckling modes in the simulation, as visible in Figure 6.2 and Figure 6.3. The roof is made of thin mild steel that has only a small resistance, and hence the different buckling behavior may easily occur, but has very little influence on the simulation results.

To compare the deformed roof visually, the left front view of the test vehicle and the simulation are shown in Figure 6.2 and Figure 6.3. Both test and simulation show similar behavior in the side sections, the buckling points of the A-pillar and b-pillar are in the same area, and the window sill also buckled at the same area. The roof itself buckled slightly different in the simulation, showing a relatively straight buckling line in the test, but a skewed buckling line in the simulation, going from the center of the window header to the right rear end of the car.

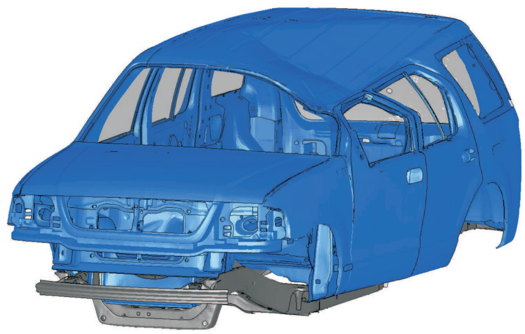

Figure 6.2: Deformed vehicle of baseline simulation

Figure 6.3: Deformed vehicle of test 0139 [5]

The simulation results coincide very well with the test results: The roof collapses in a similar way, and the rigid wall force coincides with the loading device force. The differences have few influence on the simulation results, and the model can be considered as verified for the FMVSS 216 roof crush test.

6.2 Evaluation of various roof strength improvements

Based on the baseline roof crush simulations, several roof strengthening methods were applied to the model and their effectiveness on the static and dynamic roof strength was evaluated. The three principal ideas of roof strengthening evaluated in this report are:

- High strength steel solution
    - Application of high-strength steel to various sections of the roof

  - Adding high strength steel reinforcements to the roof
  - Geometrical changes / enlargement of roof sections combined with high strength steel solution
  - Influence of laser welding technology on the roof section

- Application of a roll cage with various material gauges

- Rigid foam solution, application of foam fillings to various roof sections

A complete overview of the simulated improvements is given Design of Experiments Matrix in Table 6.1. All improvements have been simulated statically and dynamically to evaluate their effectiveness. The graphs and additional pictures of the simulation results are listed in Appendix D.

6.3 Influence of elastic behavior during the near side impact

An elastically responding roof on the near side impact is assumed to cause a less severe impact on the far side. To determine the influence of the elastic behavior without changing the properties of the roof structure on the far side, the near side was modeled with elastic materials. Therefore, the material models of all structural components on the right side of the car were replaced with non-yielding steel material, using the *MAT_ELASTIC-material of LS-DYNA. The Young's modulus was set to E = 210MPa and the Poisson's ratio to μ = 0.3. The elastic parts are marked red in Figure 6.4.

Table 6.1: Design of Experiments (DOE)

Method	Iteration	Changed Part Properties					Added Parts / Annotations
		A-Pillar	B-Pillar	C-D-Pillar	Roof Rails	Side Rails	
First impact elastic		Elastic	Elastic	Elastic	baseline	Elastic	Right doors elastic
High Strength Steel Solution	Material upgrade	1.75 mm 22MnB5	1.75 mm 22MnB5	1.75 mm 22MnB5	none	1.75 mm 22MnB5	B-Pillar inner layer and midlayer upgraded
	A-Pillar reinforced	upgrade	none	none	none	upgrade	A-Pillar and Side rail reinforcement layer added, 1.75 mm 22MnB5
	B-Pillar reinforced	none	upgrade/ upgage	none	none	none	B-Pillar midlayer 1.4 mm 22MnB5, additional layer, 2.5mm, MS-Steel
	A/B-Pillar reinforced	upgrade	upgrade/ upgage	none	none	none	Combination of A-Pillar- and B-Pillar reinforcement
	Enlarged window header	upgrade	upgrade/ upgage	none	1.75 mm 22MnB5	none	Enlarged window header support + A-Pillar- and B-Pillar reinforcement
	Enlarged A-Pillar	upgrade/ enlarged	upgrade/ upgage	none	none	none	Enlarged A-Pillar crossection + A-Pillar- and B-Pillar reinforcement
	VW Tiguan Material Data	change	change	none	change	change	A-Pillar- and B-Pillar reinforcement, material data from tensile tests
	Baseline + Laser welds	Laser-welded	Laser-welded	none	none	Laser-welded	Baseline Simulation, Spotwelds replaced with laser welds
	Reinforced + Laser welds	upgrade	upgrade/ upgage	none	none	none	A-Pillar- and B-Pillar reinforcement, Sections laser welded
Foam Solution	Baseline + Foam	Foam filling	Foam filling	none	none	Foam filling	Baseline simulation with foam insertions
	A/B-Pillar reinf. + Foam	upgrade	upgrade/ upgage	none	none	none	A-Pillar- and B-Pillar reinforcement, B-Pillar foam filling
Rollcage	2mm Rollcage	Rollcage 20 mm	Rollcage 30 mm	none	Rollcage 30 mm	Rollcage 20 mm	Steel with 370 MPa yield strength
	4mm Rollcage	Rollcage 20 mm	Rollcage 30 mm	none	Rollcage 30 mm	Rollcage 20 mm	Steel with 370 MPa yield strength

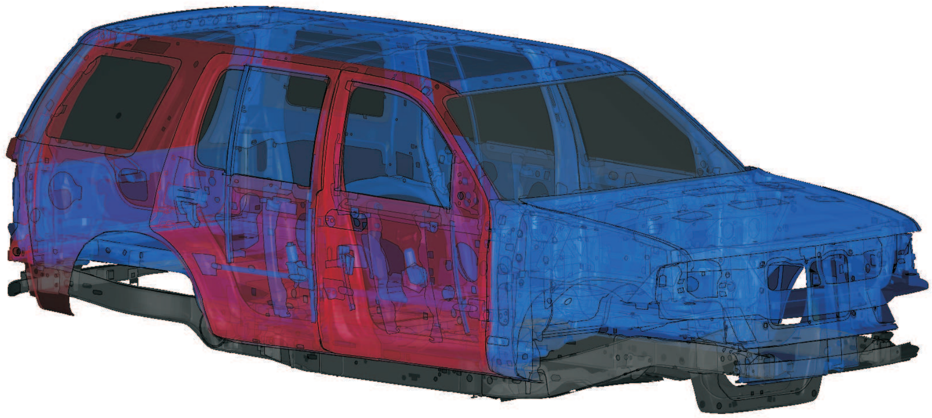

Figure 6.4: Elastically modeled parts for elastic near-side impact

Results

The simulation resulted in a clear difference compared to the baseline simulation. The elastic roof showed significant less intrusion, and the intrusion speed of the roof was also reduced significantly. The deformed vehicles of the baseline simulation and the first elastic simulation are shown in Figure 6.5 and Figure 6.6.

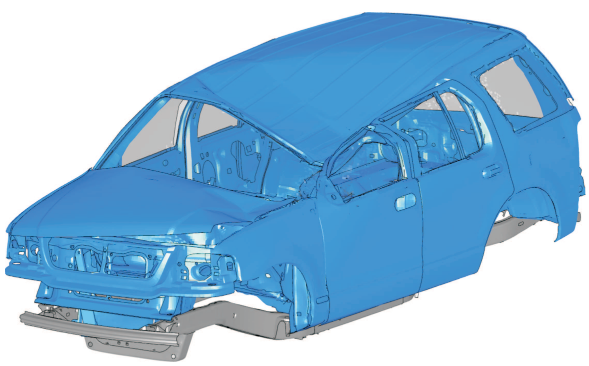

Figure 6.5: Baseline simulation vehicle

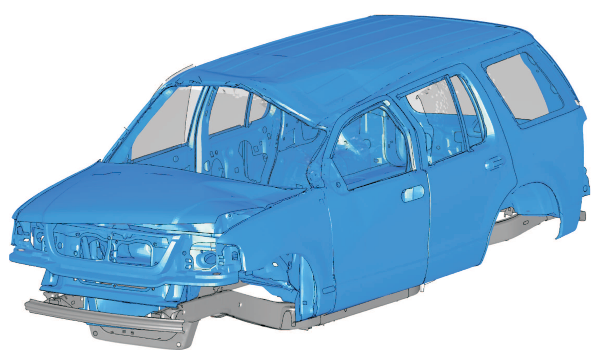

Figure 6.6: First elastic impact vehicle

The roadbed force and the behavior of the center of gravity (Graph D.3) show the reason for the less severe impact: The peak roadbed load during the near side impact is about 20 kN higher than in the baseline simulation, and beginning at this peak the center of gravity decreases less fast. This means, that a greater amount of kinetic energy is absorbed during the near side impact, resulting in less vertical kinetic energy to be transformed in the far side impact. Hence the peak load of the far side impact is smaller, remaining below 50 kN while the baseline simulation exceeds 60 kN. The center of gravity dropped less in the near side elastic impact, having its minimum at 815 mm compared to 750 mm for the baseline simulation. The difference of the drop height is compared in Figure 6.7: At a roll angle of 180° the baseline vehicle is much lower than the elastic vehicle, which means, that the far side has to rise the car a smaller distance. And since the vehicle of the elastic simulation is higher above the ground, the roadbed force drops below 10 kN and its minimum is about 10 kN lower than in the baseline simulation.

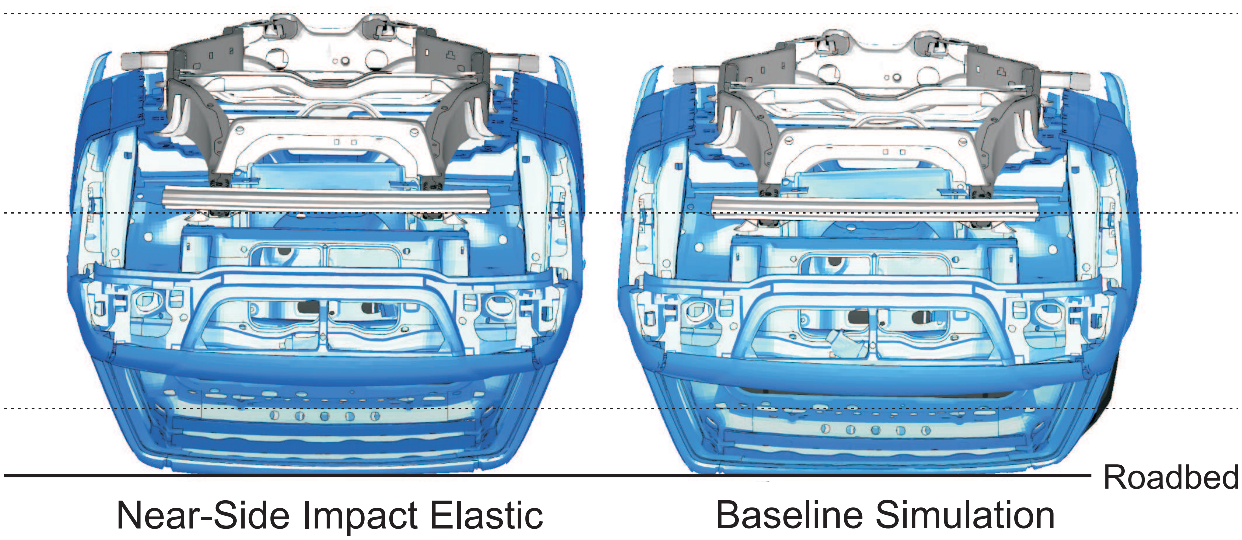

Figure 6.7: Front view of baseline and near side elastic simulation at 180° roll angle

Figure D.4 shows the von Mises stress fringe plot during the near side peak load. The elastic material has to withstand forces of 3000 MPa for the outer unibody and 1500 MPa for the structural components on the inside. This is of course way above the yield strength of actual materials, so the use of stronger material alone will not result in an elastically responding roof. So the material gauge has to be increased and additional reinforcement layers have to be added to make the near side impact elastic.

Because less vertical kinetic energy has to be transformed in the far side impact, the intrusions decreased significantly, although no part properties were changed at the far side. The intrusions dropped by 200 mm for the A-pillar and by 250 mm for the B-pillar, and the intrusion speed reaches a maximum of 15 km/h at the far-side A-pillar, hence remaining below the fatal injury limit of 16 km/h. Thus can be concluded that an elastically responding roof in the near side impact indeed reduces the severity of the far side roof impact and hence less injury risk for the occupants. Also remarkable is the fact that the peak load for the far side impact appears at a higher roll angle than in the baseline simulation (Graph D.3), which means that the load involves the window header more than in the other tests; the rotation speed is also higher than in the baseline simulation, the first elastic vehicle rolled about 10° more. This may of course lead to more rollovers in a real world crash, hence being a disadvantage of an elastically behaving roof.

6.4 High Strength Steel Solution

6.4.1 Material Upgrade Solution

The first improvement method was to apply stronger materials to the existing roof structure. Therefore the A-pillar inner layer, the side rails, the B-pillar midlayer and inner layer, the window header rail and the B-pillar roof rail have been upgaged and upgraded with the ultra high strength hot-stamping steel 22MnB5 and 1.75 mm thickness, with material data from [21]. This is a commonly used material and material gauge used for strong reinforcements like pillars and rails, see Section 2.5.1. The upgraded parts are shown in Figure D.5

Results

In both static and dynamic simulation the roof behaved much stiffer and was able to take more load than in the baseline simulation (Graph 6.9). The static roof strength increased by around 50 % to three times the vehicle curb weight. Both A-pillar and B-pillar were able to sustain a higher force, and the window header normal force increased by over 100 %. The intrusions in the JRS simulation dropped from over 500 mm to less than 300 mm, the intrusion velocities were reduced to a maximum of 14 $^{km}/_{h}$, hence remaining below the threshold of fatal injuries. The mass, a critical value since the mass is added above the center of gravity, increased moderately by 8.2 kg to 2262.9 kg.

However, a SWR of 3 is still considerably smaller than the SWR of most contemporary cars, as well as the dynamic intrusions and intrusion velocities. So a sole upgrade of the material is not sufficient and further roof strength improvements have to be performed.

6.4.2 A-Pillar Reinforcement

The A-Pillar and the side rail of the baseline simulation consists only of the thin, mild steel layer of the outer unibody and an inner reinforcement layer made of high strength steel with a yield strength of 370 MPa for the A-pillar and 300 MPa for the side rail. Considering the structure as a box-shaped tube, only the inner half of the box is made of high strength steel,

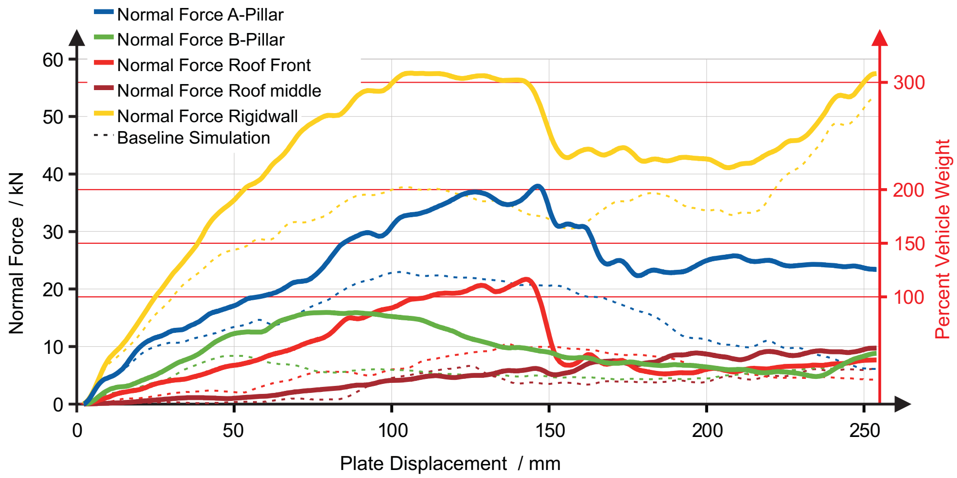

Graph 6.9: Section forces and rigidwall force of the upgraded model

the outer half is made of mild steel, hence the tube has little resistance against buckling. To reinforce the structure without making the outer unibody of a thicker and stronger steel, which would decrease its formability in deep-drawing and increase the weight significantly, some cars like the Volvo XC90 and also the VW Tiguan have an additional reinforcement layer, which is located between the inner and outer layer.

Such an additional reinforcement layer was added to the FE-model, going from the A-pillar support in the front to the C-pillar. The layer was placed below the outer unibody layer and connected to the other layers at the welding flanges, sharing the same spotwelds. The material was simulated with the 22MnB5-ultra high strength steel [21] and 1.75 mm thickness. All other parts were the same as in the baseline simulation. The reinforcement is shown in Figure 6.8.

Results

The reinforcement strengthened the roof significantly, the static rigidwall force (Graph D.14) increased from 200 % vehicle weight to 240 % vehicle weight, and the load taken by the A-

Figure 6.8: Reinforcement of A-pillar and side rail

pillar increased by around 10 kN, hence showing that the reinforcement indeed increases the strength of the A-pillar. The intrusions and intrusion velocities decreased the same way, the far side intrusions decreased by 150 mm (Graph D.9) and the peak intrusion velocities were reduced just below the limit of fatal head injuries (Graph D.10). Howwever, the near side impact was not fully elastic, because some intrusion remained after the near side impact. The geometry of the A-pillar showed less deformation and didn't buckle, and the crosssection did not deform as much as in the baseline simulation, especially the relatively thin outer layer. A comparison of the structural roof components is shown in Figure D.7, and the crosssectional geometries are compared in Figure D.6.

But the increased strength of the A-pillar–side rail section moved the weakest point of the roof to the window header: Figure 6.9 shows, that the window header buckled right next to the connection between window header and A-pillar–side rail section, which led to a V-shaped collapsed roof. This is probably even more dangerous than a collapsing roof itself, because the intruding parts are sharp edges of the roof that can cause more injuries than a flat intruding surface; and the occupant head may get trapped between the intruded window header and the side rail, which may lead to some more even worse injury scenarios. The weight increased by 9.13 kg.

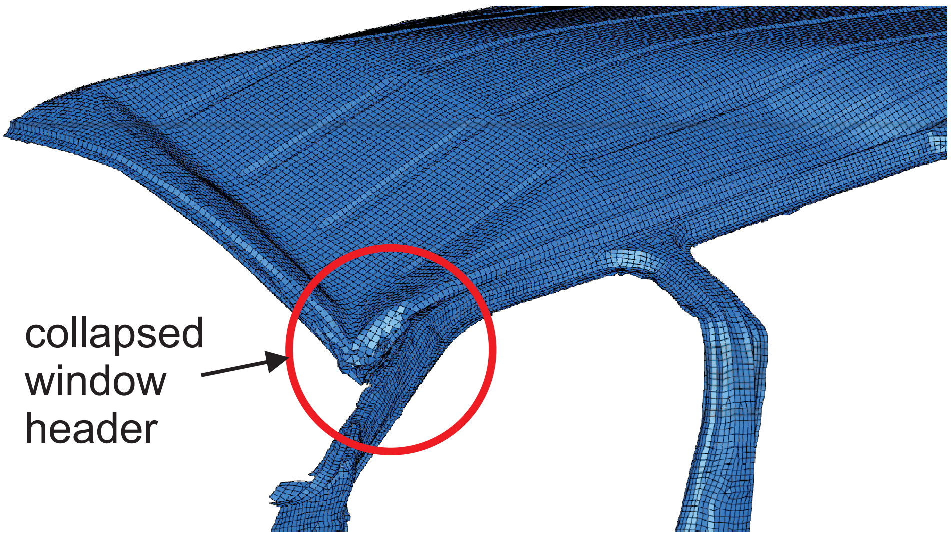

Figure 6.9: Collapsed window header in JRS rollover test

6.4.3 B-Pillar Reinforcement

Another weak point of the Ford Explorer roof is the B-Pillar. It bends about 20 cm above the side window belt line, and thus allows the side rail to intrude into the passenger compartment. The Explorer roof is made of three layers, the outer unibody layer, the inner layer and one reinforcement layer that is placed under the unibody layer. To improve the strength of the B-Pillar, the existing reinforcement layer was upgraded with 22MnB5-ultra high strength steel and an additional U-shaped reinforcement layer was added and connected to the existing reinforcement layer with spotwelds, using the *CONSTRAINED_NODAL_RIGID_BODY-keyword. 2.5 mm-martensitic phase steel from [22] was used for this reinforcement, because the shape of the reinforcement is relatively simple and may be manufactured by cold-rolling, which is much cheaper than hot-stamping. The crosssection of the reinforced B-pillar is shown in Figure 6.10, an exploded view of the B-pillar in Figure D.8. The weight increase through the reinforcement was 4.2 kg

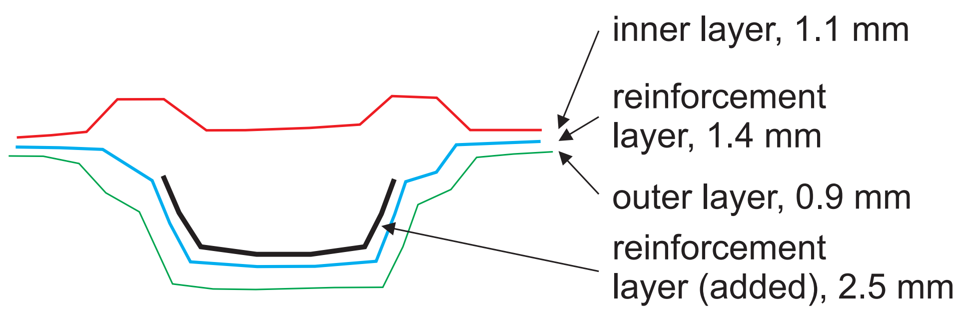

Figure 6.10: Crosssection of B-pillar reinforcement

Results

The reinforcement of the B-pillar showed little improvement in the dynamic simulation. The intrusion of the far side B-pillar were reduced by 100 mm, but the intrusions of the A-pillar decreased only by 50 mm and the far side intrusion speed changed insignificantly (Graph D.15 and Graph D.16). However, the static test showed a strength increase of 6 kN; Graph D.20 shows that this additional load is mainly taken by the B-pillar, especially between 50 mm and 100 mm plate displacement. This shows that 5° pitch angle of the static roof crush test indeed lead to a higher load of the B-pillar than in dynamic rollover crashes; so a higher pitch angle, as mentioned in other studies [9, p. 8], which would load the vehicle closer to the A-pillar, would indeed be closer to a dynamic rollover test.

6.4.4 Combination of A-Pillar and B-Pillar Reinforcement

For further improvement the A-pillar reinforcement and B-pillar reinforcement were combined, and the existing reinforcement layer in the B-pillar was upgaged to 1.75 mm. All other parts remained unchanged. The changed structure is shown in Figure 6.11. The mass increase caused by the reinforcements was 17.1 kg.

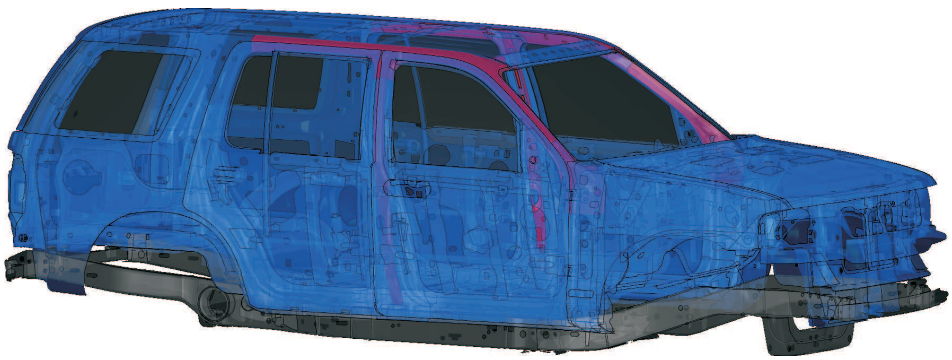

Figure 6.11: Upgraded parts in A-pillar and B-pillar reinforced simulation

Results

The roof performance profited more by the combination of A-pillar reinforcement and B-pillar reinforcement than by the individual tests: The far side intrusions were reduced by almost 300 mm, the intrusion velocities were reduced significantly, but exceeded the serious injury threshold during a approximately 150 ms-peak and went up to 13.8 $^{km}/_{h}$. Graph 6.10 compares the A-pillar intrusion of the three reinforcement methods, and the combination of both reinforcements reduces the intrusion by almost an additional 100 mm. The near side intrusions in Graph D.21 tend to zero after the near side impact, and the roadbed force in Graph D.23 also tends to zero after a near side peak of 20 kN more than in the baseline simulation. So through these reinforcements an elastic behavior of the roof can be gained.

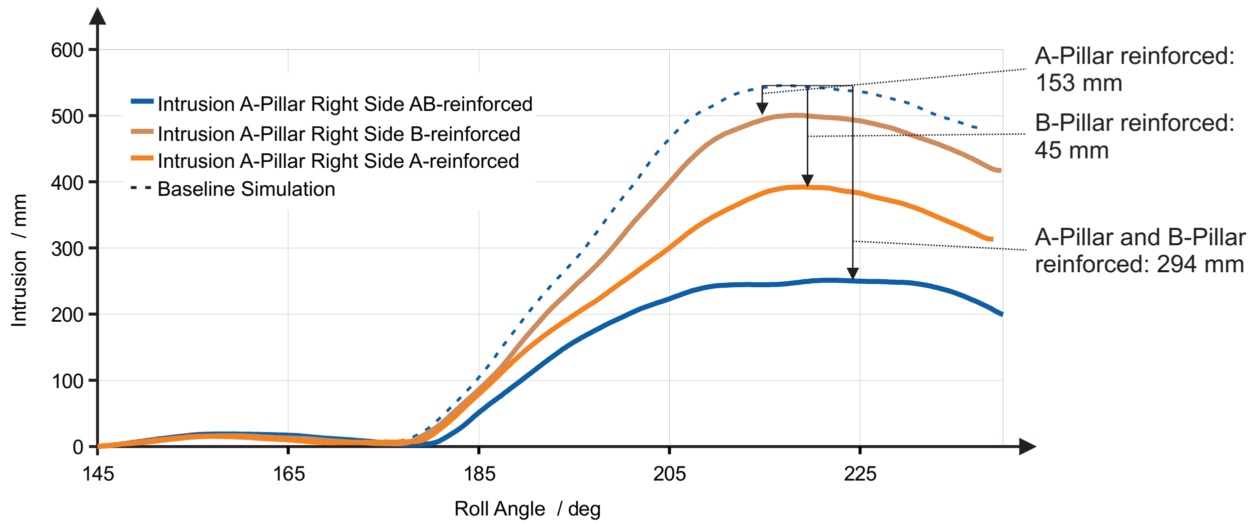

Graph 6.10: Comparison of A-pillar intrusion

The post-simulation interior view of the baseline simulation and the reinforced simulation is shown in Figure 6.12. The reinforced roof results in much less intrusion, but therefore the window header buckled at the end of the A-pillar–window header connection, which is obviously now the weakest point in the roof. The firewall still skews during the rollover, the reinforcements do not improve the strength of the lower car body. Because the center of gravity is kept higher during the rollover (see Graph D.23), the hood is also less involved in the damage pattern; while the hood buckles significantly in the baseline simulation, no damage is visible in the interior view of the reinforced simulation.

6.4.5 Reinforcement of the Window Header

The stronger sides of the vehicles resulted in a significantly stronger roof and hence decreased the injury probability, but resulted in a buckling window header that intrudes into the passenger compartment. To prevent such a dangerous buckling, the window header

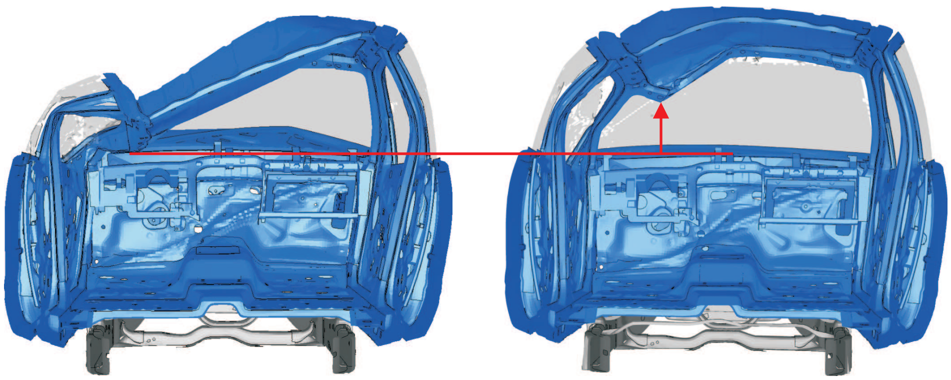

Figure 6.12: Comparison of roof intrusion

was strengthened and the connections between the window header and the A-pillars enlarged. The window header consists of two parts, one U-shaped part made of mild steel and one relatively flat part made of high strength steel; the U-shaped part was used for the improvement. The material grade and gauge was changed to the hot-stamping steel 22MnB5 and 1.75 mm thickness. This led to an additional weight of 19.3 kg compared to the baseline simulation, and the weight of the window header itself increased by 2.2 kg. The enlarged header is compared to the original header in Figure 6.13.

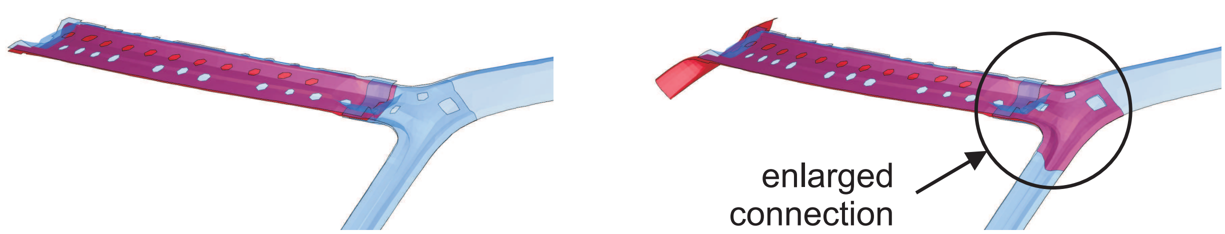

Figure 6.13: Comparison of the original header and the improved header

Results

Although the buckling behavior was not completely removed, the window header buckled less than without the reinforcement and the intrusions and intrusion velocities decreased

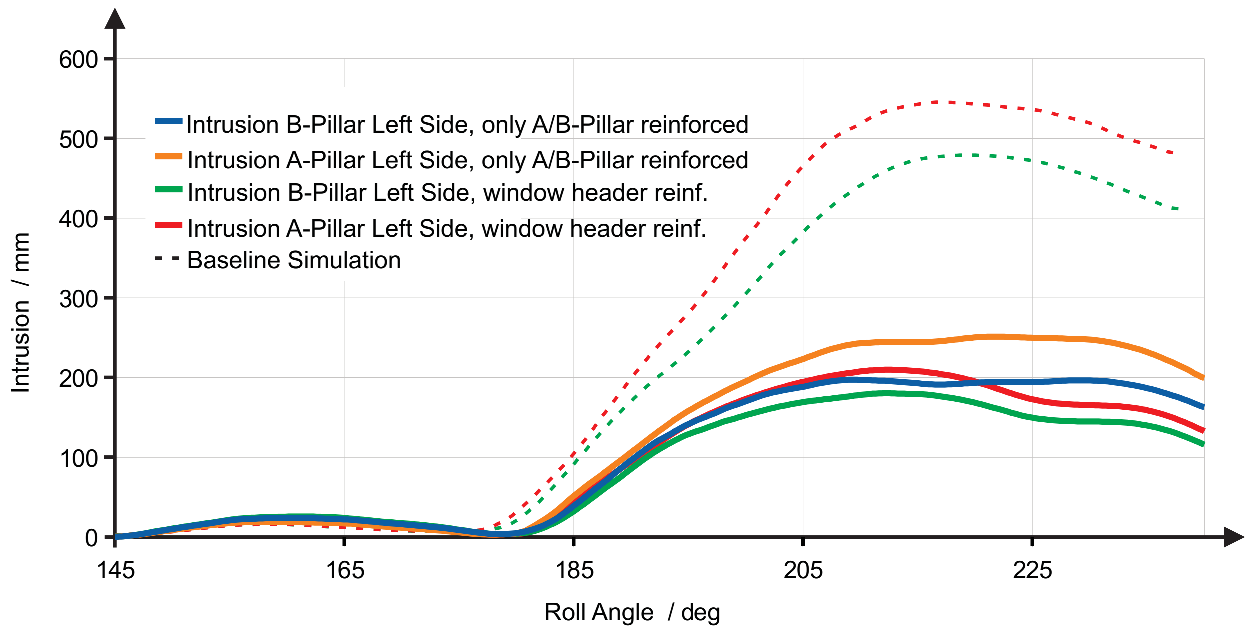

Graph 6.11: Comparison of far side intrusions

further. Graph 6.11 shows the far side intrusions of the simulation with the original window header (Section 6.4.4) and of the simulation with the improved window header. The intrusions decreased to a little above 200 mm maximum A-Pillar intrusion, compared to 550 mm in the baseline simulation and 250 mm in the reinforced simulation without the strengthened window header. Figure 6.14 shows the difference between the intrusion profiles of the baseline simulation compared with the A-/B-pillar reinforced simulation and the simulation with the reinforced window header.

6.4.6 A-Pillar Enlargement

One disadvantage of the Ford Explorer roof is its weak A-pillar, which can not sustain high forces and buckles during the static and dynamic roof crush tests. Compared to other currently sold cars, the Explorer's A-pillar is much smaller than the A-pillars of cars

Baseline | A-Pillar and B-Pillar reinforced | A- / B-Pillar and window header reinforced

Figure 6.14: Comparison of intrusion profiles

that perform better in roof crush tests. This arises when the exterior view of the Explorer is compared to a better vehicle – Figure 6.15 shows the Explorer's A-pillar and the VW Tiguan's A-pillar, the visible part of the Tiguan's A-pillar is about four times as large as the Explorer one's. The crosssectional comparison of both A-pillars shows a similar result: The crosssection of the Ford Explorer is much smaller and above all not as box-shaped as the Tiguan's A-pillar.

To enlarge the whole A-pillar–side roof rail section, parts of the doors have been decreased in size and the corresponding sections of the roof enlarged, as well as the reinforcement, that was adopted from the A-pillar reinforced simulation in Section 6.4.2. All other properties of the model were equal to the simulation of Section 6.4.4.

Results

The enlargement did neither reduce the intrusion values nor the intrusion speed in the dynamic test, but the the A-pillar was indeed able to sustain a higher load during the far-side impact. While the A-pillar took about 38 kN load in the solely reinforced simulation Graph D.36, it reached a normal force of about 43 kN in the reinforced and enlarged simu-

Figure 6.15: Exterior view of Ford Explorer (left) and Volkswagen Tiguan (right)

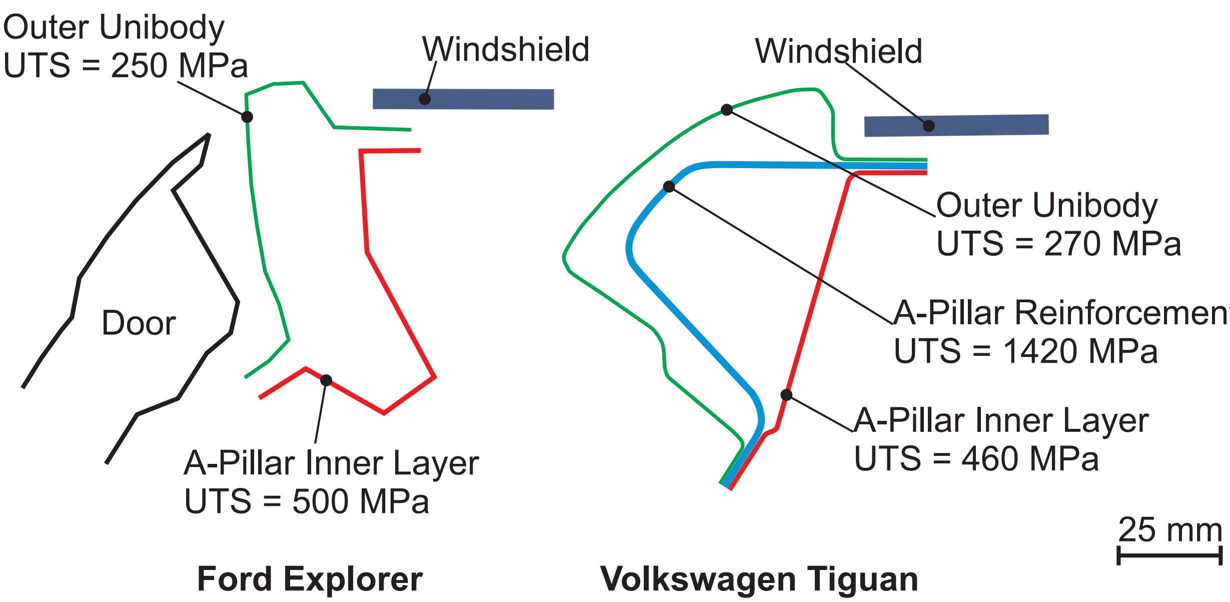

Figure 6.16: Crosssection of A-pillars – Ford Explorer and VW Tiguan (true to scale)

lation, leading to a about 3 kN higher roadbed force, while the other crosssectional forces remained constant. However, the enlargement resulted in a rather small improvement in the static roof crush test: The rigidwall force increased from 53 kN to 58 kN, but the A-pillar crosssectional force grew from 32 kN in the solely reinforced simulation to 41 kN in the reinforced and enlarged simulation, but on the other side the B-pillar normal force was reduced by 4 kN.

6.4.7 Tensile Test Material Data

The material data gained in the tensile tests of chapter 5 has been transformed into LS-DYNA material cards and applied to the reinforced roof of the Ford Explorer. The reinforced roof of Section 6.4.4 was chosen because the VW Tiguan has a similar, three-layered A-pillar- and side rail structure and also a four-layered B-pillar. For an application to the baseline model the strongest material would have been left out, hence a much weaker performance was to be expected in the simulation. The material cards derived from the tensile test data are listed in Appendix C. The changed materials at the roof are shown in Figure 6.17, all materials except the MS-Steel from [22] were derived from the tensile tests.

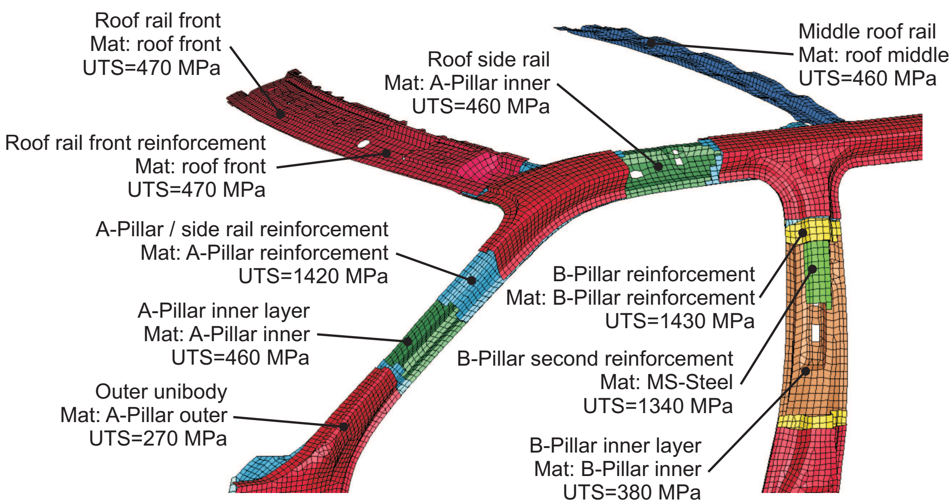

Figure 6.17: Applied materials from tensile tests

Results

The changed material grades didn't result in a stronger roof, the intrusion values are about the same as in the A+B-Pillar reinforced simulation of Section 6.4.4, only the near side intrusion was reduced during the far side impact by around 30 mm, which means, that less crush force was transfered through the roof rails to the near side. The SWR actually dropped by 20 %, the section forces and roadbed force were similar to the forces in the A+B-Pillar reinforced simulation.

6.5 Influence of laser welded roof sections

Laser welded roof sections are standard in many contemporary cars, for various reasons described in Section 2.5.2. Since the Ford Explorer is joined exclusively with spotwelds, a possible improvement of laser welded roof sections will be analyzed. Spotwelds are simulated in LS-DYNA either with the *CONSTRAINED_SPOTWELD – keyword or, since the failure option is not used for the roof sections, with the *CONSTRAINED_NODAL_RIGID_BODY – keyword option. When the failure option is not significant, the *CONSTRAINED_NODAL_RIGID_BODY – keyword can be used instead of the *CONSTRAINED_SPOTWELD – keyword. The laser welds are also simulated with the *CONSTRAINED_NODAL_RIGID_BODY – option, but instead of placing one rigid body at each spotweld, each node in line of the laser welding is constrained with a rigid body. An exemplary section of a laser weld is shown in Figure 6.18. Two simulations were tested with the laser welded sections: The baseline simulation and the A-pillar/ B-pillar reinforced simulation of Section 6.4.4. The location of the laser welds in the baseline simulation is shown in Figure 6.19. The A-pillar/ B-pillar reinforced simulation was equipped at the same sections, and additionally at the welding edge between the roof and the side sections, because the reinforcement is attached to this welding edge.

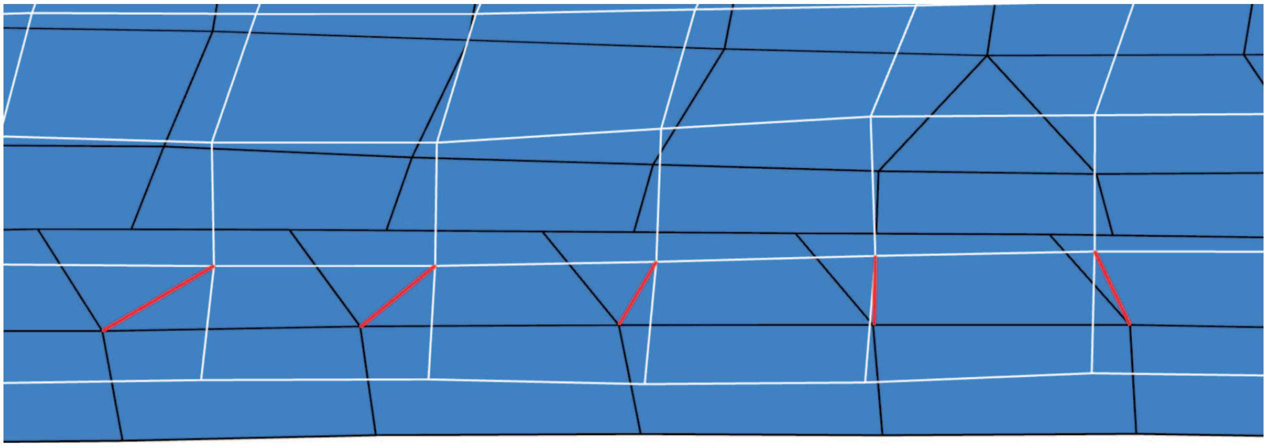

Figure 6.18: Exemplary section of a laserweld

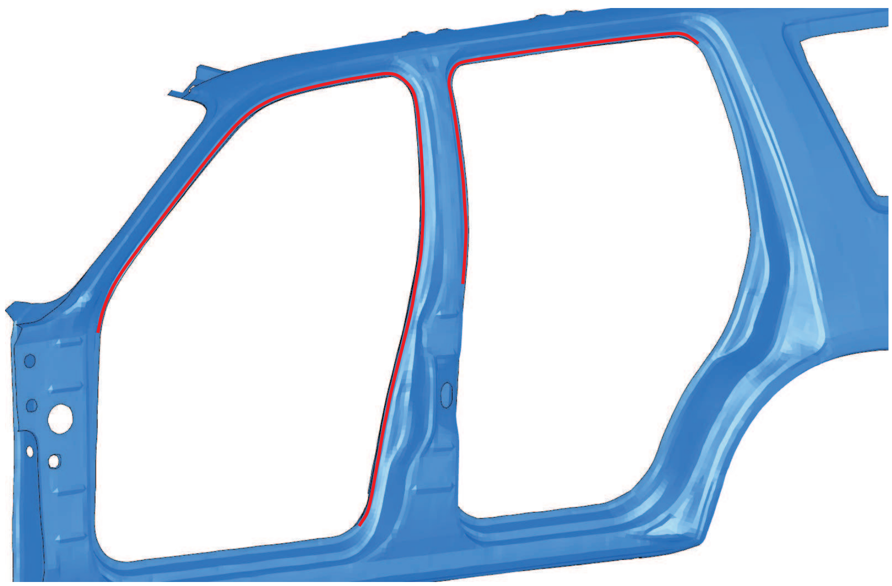

Figure 6.19: Locations of laserwelds in baseline simulation

Results

The laser welded sections resulted in a moderate improvement in intrusion and intrusion speed. The baseline roof profited more from the laser welded sections than the reinforced roof. The maximum intrusion of the baseline laser welded roof decreased by 60 mm, the maximum intrusion speed was reduced by 3 $^{km}/_{h}$; the reinforced and laser welded roof had a maximum intrusion reduced by 10 mm and a maximum intrusion speed reduced by 1 $^{km}/_{h}$ compared to the spotwelded, reinforced simulation (Graph 6.12, Graph 6.13). For the static simulation, the baseline laser welded roof didn't show a significant difference to the spotwelded baseline simulation, the reinforced laserwelded roof had a 5 kN higher roof strength than the spotwelded reinforced roof, which resulted similarly from a higher load of the A-pillar and B-pillar.

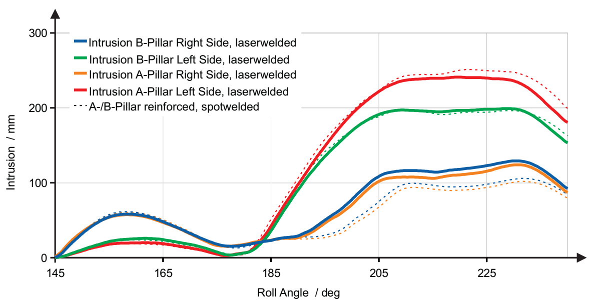

Graph 6.12: Comparison of intrusion of laserwelded, reinforced roof with the spotwelded version

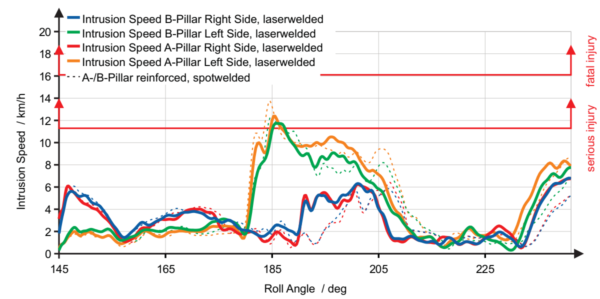

Graph 6.13: Comparison of intrusion speed of laserwelded, reinforced roof with the spotwelded version

6.6 Rigid Foam Enhancement Solution

Besides the classical strengthening method with high strength steel, the effectiveness of rigid foam fillings is investigated. Previous studies have shown, that rigid foam fillings are a lightweight and effective method to reinforce the roof of a car [12]. The rigid foam solution chosen for this study consisted of a rib-structure made of structural foam and was applied to sections of the A-pillar, B-pillar and side roof rail; the foam reinforcements are shown in Figure 6.20. Two different variations were tested: The baseline simulation was upgraded with foam enhancements in A-pillar, B-pillar and side roof rail, and the A-/B-pillar reinforced simulation of Section 6.4.4 was upgraded with a foam reinforcement in the B-pillar. Other reinforcements were not included in the A-/B-pillar reinforced simulation, because the steel reinforcement would have reduced the usable area for the foam enhancement and hence limited its effectiveness. The mass increase of the upgraded baseline simulation was 10.1 kg, the mass increase of the A-/B-reinforced simulation was 2.9 kg for the foam reinforcement and 17.1 kg for the steel reinforcement in A-pillar/side roof rail and B-pillar.

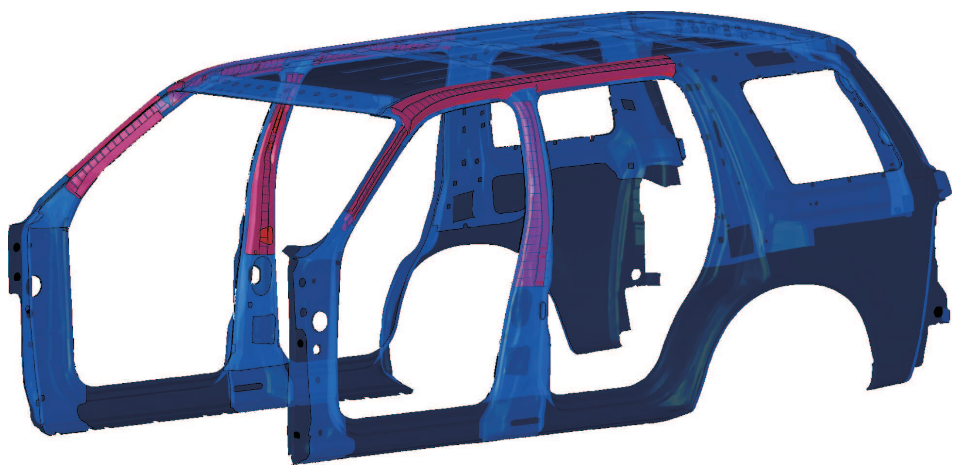

Figure 6.20: Rigid foam reinforcements

Results

The upgraded baseline simulation resulted in a decent improvement of the intrusion and intrusion speed values. The maximum intrusion was reduced by 170 mm and the maximum intrusion speed was reduced by 5.5 $^{km}/_{h}$, hence dropping below the fatal injury threshold for intrusion speed (see Graph D.57 and Graph D.58). The static roof strength increased significantly by 50 %, the majority of the increased load was taken by the B-pillar, which took 10 kN more load, while the A-pillar load increased only by 5kN.

The upgraded reinforced simulation profited only marginally from the foam enhancement: The maximum intrusion didn't change at all, the maximum intrusion speed was slightly reduced by 0.8 $^{km}/_{h}$. On the contrary, the static simulation profited significantly from the foam reinforcement: The SWR was increased by 60 % to 340 % vehicle weight, and the section forces show again that the majority of the additional load is taken by the B-pillar. The comparison of the A-/B-pillar reinforced simulation with the foam enhanced simulation is shown in Graph 6.14, Graph 6.15 and Graph 6.16. Graph D.57 shows a significant residual near side intrusion of both A-pillar and B-pillar after the near-side impact, so the foam enhancement solution is not a sufficient method to gain an elastic response in the near side impact.

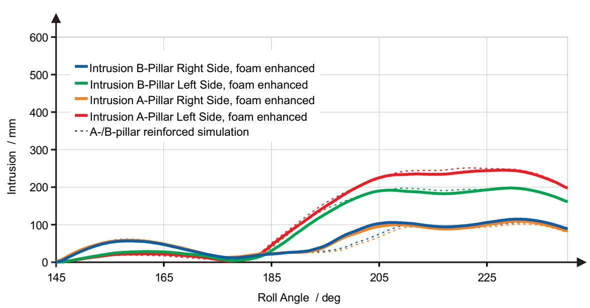

Graph 6.14: Comparison of intrusion of A-/B-pillar reinforced simulation with foam enhanced simulation

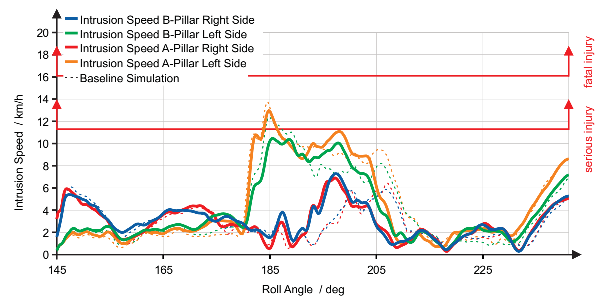

Graph 6.15: Comparison of intrusion speed of A-/B-pillar reinforced simulation with foam enhanced simulation

6.7 Roll cage application

The baseline vehicle was equipped with a roll cage that spans around the A-pillar- and side roof rail section, around the B-pillar section and around the window header. The roll cage

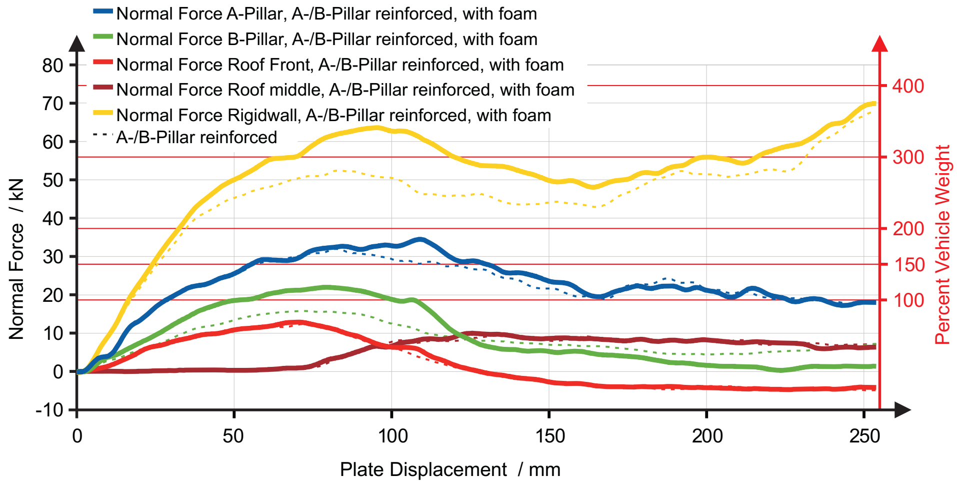

Graph 6.16: Comparison of static section forces of A-/B-pillar reinforced simulation with foam enhanced simulation

was made of three components: One tube is integrated in the B-pillars and the middle roof rail, a second tube begins at the lower A-pillar and runs through the A-pillar and the side roof rail to the B-pillar tube. A third tube connects both A-pillar tubes at the window header. Figure 6.21 shows the roll cage within the car structure. The roll cage was completely integrated into the existent structure of the car: Inside the A-pillar, inside the B-pillar and inside the side roof rails. The window header tube fits between front window header and windshield. This method was chosen because this would be a applicable method used as a standard equipment in a series production car, and not as a customizing option for racing or tuning purposes. Since the roll cage was integrated in the structure, the tube diameters were chosen relatively small as 30 mm for the B-pillar/middle roof rail section and 20 mm for the A-pillar/side roof rail tubes and the window header tube. The tubes reached into the lower A-pillar and to the rockerpanels, and were fixed there with nodal rigid bodies. Two simulation series were performed with 2 mm and 4 mm shell thickness.

Material data for 25CrMo4-steel was not available, so a 370 MPa-steel from the baseline Explorer model was chosen as the tube material. The roll cage was attached to the body with rigid bodies, using the *CONSTRAINED_NODAL_RIGID_BODY–option, at the lower A-pillar and B-pillar. Some smaller sections at the B-pillar-side roof rail connection and at the lower part of the A-pillar had to be removed to prevent penetrations of the roll cage and the car body. However, the influence of the removal was assumed to be small. The total weight increase was 8.9 kg for the 2 mm-rollcage and 18.9 kg for the 4 mm-rollcage.

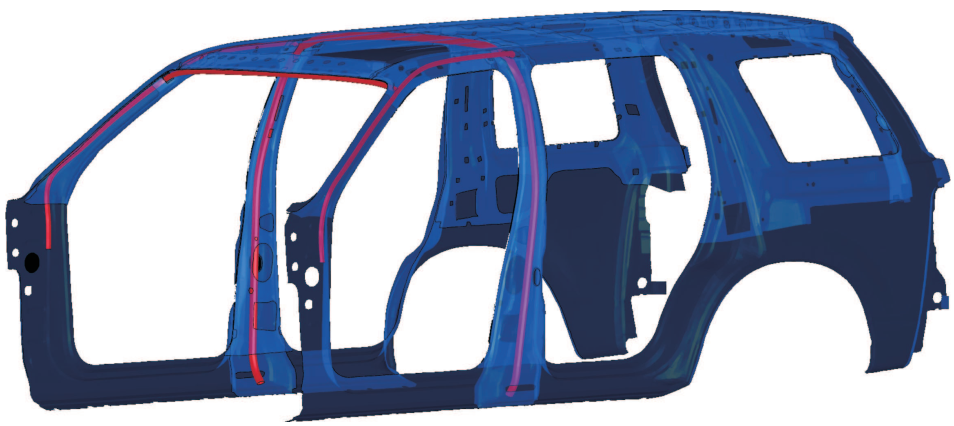

Figure 6.21: Roll cage structure

Results

Both the 2 mm-roll cage and the 4 mm-roll cage improved the roof significantly. The intrusions decreased to 286 mm (2 mm-roll cage) and 214 mm (4 mm-roll cage), the intrusion speed was reduced to around 15 $^{km}/_{h}$. The 2 mm-roll cage is a quite attractive solution: A relatively low mass increase of 8.9 kg and easily producible parts result in a decent decrease of intrusion and intrusion speed, but the decrease of intrusion speed was higher at the high strength steel solution. The 4 mm-roll cage lowered the intrusions again, but showed no improvement for the intrusion speed. However, the static roof strength increased significantly by 0.8 compared to the 2 mm-roll cage simulation. But with a mass increase twice as much as for the 2 mm-roll cage, the 4 mm-roll cage is not as effective as the 2 mm-roll cage.

6.8 Variation of the initial conditions

The pitch angle of 5° was increased to 10° to determine, whether the improved vehicle roof performs well under the tightened initial conditions. A higher pitch angle is considered to cause a more severe impact to the roof, because it shifts the load from the B-pillar to the A-pillar, but also as more realistic, based on statistical evaluations. Both the baseline simulation and the A-/B-pillar reinforced simulation with reinforced window header were simulated with a 10°-pitch angle and otherwise unchanged initial conditions.

Results

The higher pitch angle had little influence on the baseline simulation: For both pitch angles, the high intrusion on the far side A-pillar is limited by the contact of the roadbed with the hood, so hardly any difference between the crash patterns in Figure 6.22 is visible. This is the same for the intrusions shown in Graph D.81: the A-pillar intrusion remains at the same high level, the B-pillar intrusion is actually reduced. A possible explanation for this behavior is the fact, that the A-pillar intrusion is limited by the hood contact, and that the hood takes a higher force in the high-pitch simulation. While the maximum intrusion remains the same, the intrusion speed increases significantly from 19 $^{km}/_{h}$ to almost 24 $^{km}/_{h}$, making the impact even more fatal.

The reinforced vehicle reacts different on the higher pitch angle: While the vehicle didn't touch the roadbed with the hood in the 5°-pitch simulation, the hood contacted the roadbed in the 10°-pitch simulation. The intrusion values increased for the reinforced vehicle by 50 mm for the maximum A-pillar intrusion, and the intrusion speed increased slightly by 1.5 $^{km}/_{h}$ to 13.5 $^{km}/_{h}$. However, the reinforced roof is still way better than the baseline roof, an it can be concluded that a higher pitch angle indeed is more severe and leads to higher intrusion values. Graph D.81 shows, that the near side intrusions still tend to zero after the near side impact, so the higher pitch angle did not result in major plastic deformation during the near side impact.

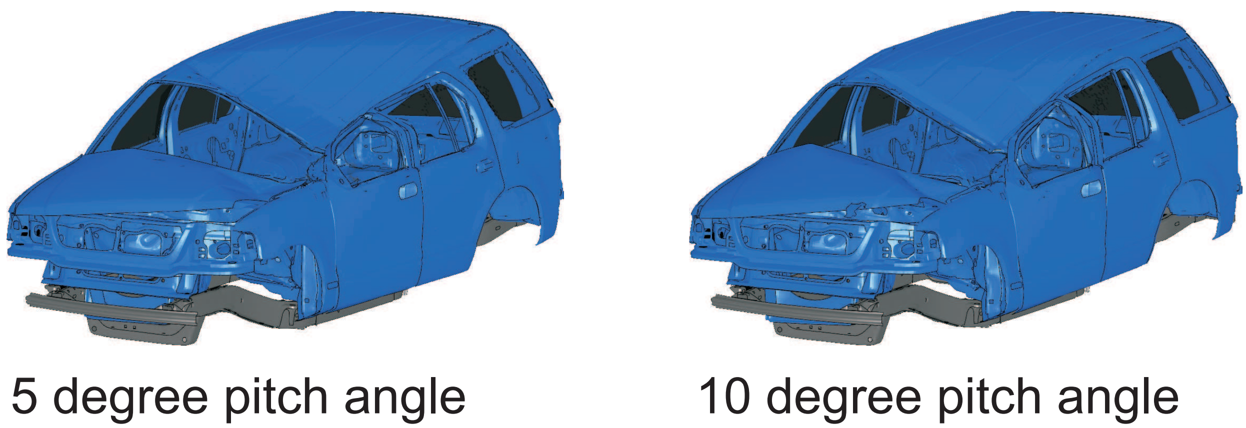

Figure 6.22: Comparison of post-simulation damage, baseline simulation

6.9 Vertical drop tests

In addition to the JRS simulations, the baseline model and the A-/B-pillar reinforced model with reinforced window header were simulated in vertical drop tests. Due to the lack of repeatability of dynamic rollover tests, drop tests were an alternative to perform repeatable roof strength tests that regard the geometry of the roof and the vehicle, although dynamic

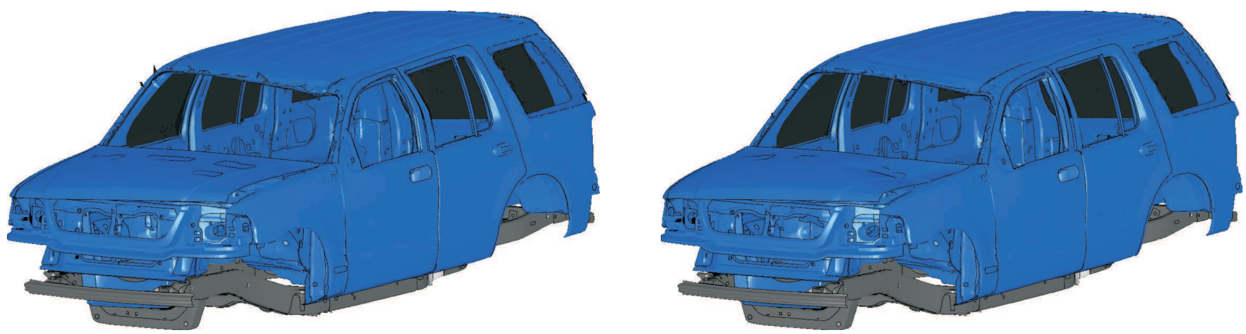

5 degree pitch angle 10 degree pitch angle

Figure 6.23: Comparison of post-simulation damage, A-/B-pillar, window header reinforced simulation

factors are still neglected.

The drop test simulations were performed with the same setup and initial conditions as the JRS simulations, except that there was no initial rotational speed and the roadbed did not move. The tests were run with 280 ms simulation time, at this time the vehicle began moving from the roadbed and the roadbed force went down significantly.

Results

The reinforced roof remained stable in the drop test simulation, while the roof of the baseline simulation collapsed, and A-pillar and B-pillar buckled. So the drop test simulation revealed the same weak points of the roof as the JRS simulation. Figure 6.24 and Figure 6.25 show the vehicle at maximum intrusion, with significant damage in the baseline simulation. Graph D.92 shows very well, that the stiffer roof of the reinforced drop test simulation the vehicle is stopped much faster than the baseline simulation, resulting in a much earlier peak load of the roadbed force.

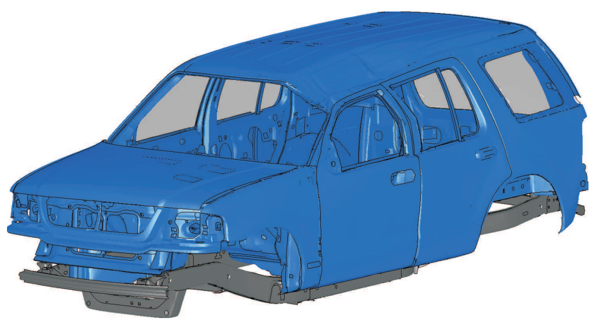

Figure 6.24: Crushed roof at maximum intrusion in baseline simulation

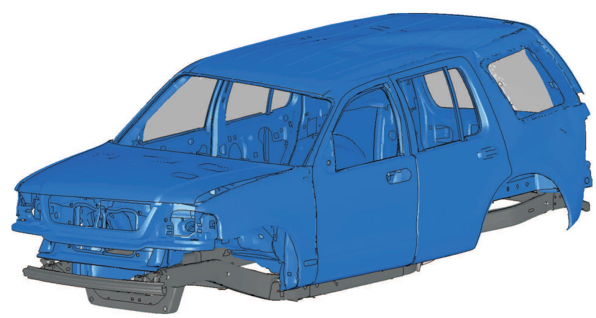

Figure 6.25: Crushed roof at maximum intrusion in A-/B-pillar + window header reinforced simulation

7 Discussion and Outlook

The focus of this research was to design an elastically responding roof in the near side impact. Three different reinforcement methods have been tested to improve the otherwise very weak Ford Explorer roof, and an elastically responding roof was found to be producible with high strength steel reinforcements and an integrated roll cage. Foam enhancement as a stand-alone solution was not proven to be a sufficient reinforcement method to gain elastic response in an otherwise extremely weak roof. A higher pitch angle results indeed in a higher load of the A-pillar and hence in more roof intrusion into the occupant compartment, but a contact of the hood with the roadbed limits the intrusion, so geometrical circumstances have to be considered when a vehicle is subject to a rollover test.

7.1 Effectiveness of the reinforcement methods

A contemporary vehicle will only be successful on the highly competitive car market, when it represents an attractive offer for a potential customer in terms of purchase price, maintenance costs, fuel economy, safety and durability. So a roof reinforcement method has to be cost-effective as well as lightweight, and it has to be sufficient enough to meet the new federal safety requirement and perform well in consumer information ratings. Table 7.1 lists all tested reinforcement methods with their resultant improvement and weight increase.

All simulations showed, that the weak roof of the Ford Explorer can be reinforced with a reasonable amount of weight increase and production expenditure, which would reduce

Table 7.1: Effectiveness evaluation

Method	Iteration	Improvement			Added Parts	Weight Increase
		Maximum Intrusion	Max. Intr. velocity	SWR		
baseline simulation		546 mm	19.7 km/h	2.06	N/A	N/A
High Strength Steel Solution	Material upgrade	285 mm	14.3 km/h	3.09	N/A	8.2 kg
	A-Pillar reinforced	392 mm	16.0 km/h	2.31	2	9.13 kg
	B-Pillar reinforced	501 mm	18.1 km/h	2.35	2	4.2 kg
	A/B-Pillar reinforced	251 mm	13.8 km/h	2.81	4	17.1 kg
	Enlarged window header	210 mm	12.3 km/h	3.42	4	19.3 kg
	Enlarged A-Pillar	255 mm	13.3 km/h	3.12	4	18.5 kg
	VW Tiguan Material Data	257 mm	13.4 km/h	2.70	4	17.2 kg
	Baseline + Laser welds	480 mm	16.5 km/h	1.96	N/A	0 kg
	Reinforced + Laser welds	241 mm	12.4 km/h	3.06	4	17.1 kg
Foam Solution	Baseline + Foam	374 mm	14.1 km/h	2.55	6	10.1 kg
	A/B-Pillar reinf. + Foam	245 mm	13.0 km/h	3.41	6	20 kg
Rollcage	2mm Rollcage	286 mm	15.0 km/h	2.96	3	8.9 kg
	4mm Rollcage	214 mm	14.9 km/h	3.76	3	18.9 kg

the intrusion and intrusion speed values significantly and would increase the occupant protection in case of a rollover. Even a change of the material grade, which would be a rather inexpensive reinforcement solution, provided a significantly better roof strength than the baseline condition. However, since the roof structure is only made of two layers, the thin outer unibody and the inner structure, the achievable roof strength by material grade and material gage change is very limited. Hence a reinforcement layer in the A-pillar and side roof rail section is indispensable to gain further roof strength improvement. Such a reinforcement layer provides together with the inner layer a box-shaped structure that has a high moment of inertia of area and is resistant against buckling.

The pillar crosssection itself turned out to be inadequately small to prevent buckling, even with the reinforcement layer. The A-pillar crosssection of the VW Tiguan shows a different, more box-shaped structure than the Ford Explorer and is hence less likely to buckle. An enlargement of the A-pillar didn't prove to be very effective, however, the geometrical circumstances didn't allow substantial changes of the A-pillar crosssection, hence a complete redesign would be necessary.

The foam solution as a stand-alone solution did result only in moderate increase of the roof strength, but a combination of steel reinforcements and foam inserts may be a good combination to maximize roof strength and minimize weight. The roll cage application also improved the roof strength and is definitely an easy way to strengthen the roof, but it is not as effective as an integrated solution, and the reinforcement is limited by the surrounding structure. Laser welded roof sections were marginally stiffer than the corresponding spot welded structure, but the biggest advantage of the laser welding technology may be the option to create much more complex geometries than it would be possible with conventional spot welding.

An near side elastically responding roof showed indeed to cause less damage on the far side, but it takes much effort to realize such a roof. Only the simulations with reinforced A-pillar and B-pillar and the 4 mm-roll cage had an elastically responding near side. The window header was not the weakest point of the baseline roof, but with reinforced A-pillars the window header buckled into the occupant headroom. Such a behavior must be prevented, because it is a very harmful event for the occupants. A reinforced window header showed a better behavior, but the source for the dangerous buckling mode was the connection between the A-pillar and the window header, with a section of the A-pillar protruding from the side structure. This design is very disadvantageous and should be changed as soon as the roof is reinforced.

7.2 Outlook

With the upgraded FMVSS 216 standard and with the growing importance of roof strength in customer information, the roof strength of vehicles like the Ford Explorer has do be improved significantly. Various reinforcement methods have been shown to increase the roof strength significantly, but of course with the cost of additional material and parts. However, an integrated design that is considered at the design of the roof may lead to much less weight increase and even better results. A stronger roof could also increase the strength in other crash configurations, especially in side and frontal crashes, and therefore the strength and weight of other structural components could be reduced. Many contemporary vehicles have shown that a strong roof with good occupant protection is practicable and affordable, and the number of vehicles with strong roofs is likely to increase in future.

Bibliography

[1] Standard no. 216: Roof crush resistance. Code of Federal Regulations, Title 49, Part 571.

[2] Center for Injury Research. http://www.centerforinjuryresearch.org/.

[3] D. Friedman and A. Jordan. Vehicle Rollover Test Fixture, Patent No. 7,373,801 B2, May 2008.

[4] K. Mori. Laser Welding Application of Car Body in Nissan. SAE technical paper series, 2003.

[5] Transportation Research Center Inc. 2002 ford explorer roof crush research with 5° pitch, 25° roll trc inc. test number: F030122. Technical report, Transportation Research Center Inc., 10820 State Route 347, East Liberty, OH 43319, February 2003.

[6] Insurance Institute for Highway Safety. Technical data file repository. http://www.iihs.org.

[7] D. Marzougui, P. Mohan, and S. Kan. Finite element model of ford explorer model year 2003 version 2. Technical report, National Crash Analysis Center, 2007.

[8] NHTSA Safety Information Website. Safercar.gov. http://www.safercar.gov/.

[9] D. Friedman and C. E. Nash. Advanced roof design for rollover protection. Proceedings of the 17th International Technical Conference on the Enhanced Safety of Vehicles, 2001.

[10] D. Friedman and R. Grzebieta. Vehicle roof geometry and its effect on rollover roof performance. 21st International Technical Conference on the Enhanced Safety of Vehicles, June 2009.

[11] Repeatability testing of a dynamic rollover test fixture. 19th International Technical Conference on the Enhanced Safety of Vehicles, (05-0362), 2005.

[12] P. Mohan, V. Nagabhushana, C. D. Kan, and R. Riley. Innovative approach for improving roof crush resistance, 2006.

[13] Livermore Software Technology Corporation. LS-DYNA Keyword User's Manual Volume 1, version 971 edition, May 2007.

[14] ASTM E8M - 00, Standard Test Methods for Tension Testing of Metallic Materials (Metric), 2000.

[15] EN. En 10292:2007 - continuously hot-dip coated strip and sheet of steels with high yield strength for cold forming – technical delivery conditions. Standard, 2007.

[16] En 10336:2007 - continuously hot-dip coated and electrolytically coated strip and sheet of multiphase steels for cold forming – technical delivery conditions. Standard, 2007.

[17] R. Hertzberg. Deformation and Fracture Machanics of Engineering Materials. John Wiley & Sons, Inc., 4 edition, 1996.

[18] N. Peixinho, N. Jones, and A. Pinho. Experimental and numerical study in axial crushing of thin walled sections made of high-strength steels. Journal de Physique, 4(110), 2003.

[19] A. Shapiro. Using LS-DYNA for hot stamping. Technical report, DYNAmore GmbH, 2009.

[20] C. Cady, S. Chen, and G. Gray. Final Report Auto/Steel Partnership Phase II. Technical report, Materials Science and Technology Division, Los Alamos National Laboratory, 1999.

[21] Material Data MB-W1500. Communication with ThyssenKrupp Steel AG.

[22] Material Data MS-Steel. Received from Mathias Büttner, MPA Stuttgart.

A Additional photos of the IIHS roof crush tests

Figure A.1: VW Tiguan after loaded with 4 times the vehicle weight

Figure A.2: VW Tiguan after 25.4 cm roof crush

Figure A.3: Buckle point of the B-Pillar of the KIA Sportage

B Tensile tests

Figure B.1: Universal testing machine used for tension tests

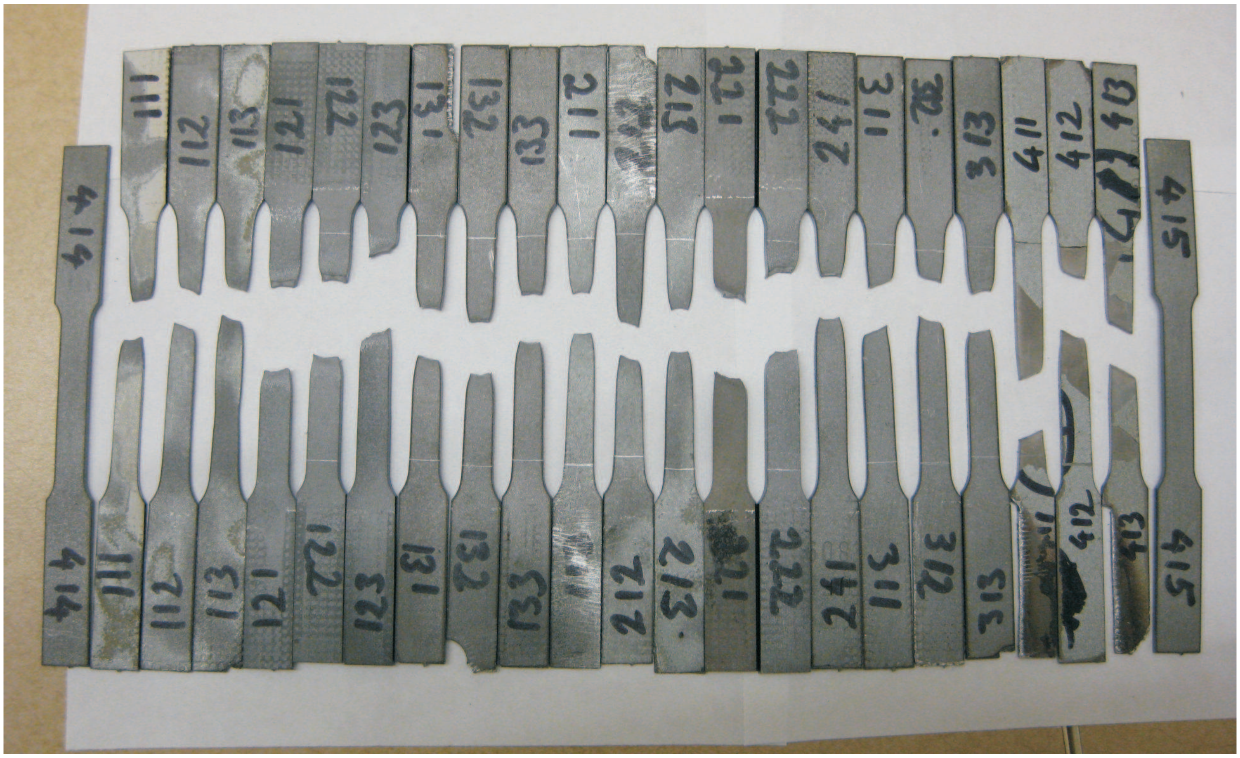

Figure B.2: Overview over all tested specimen, two outer specimen show original length

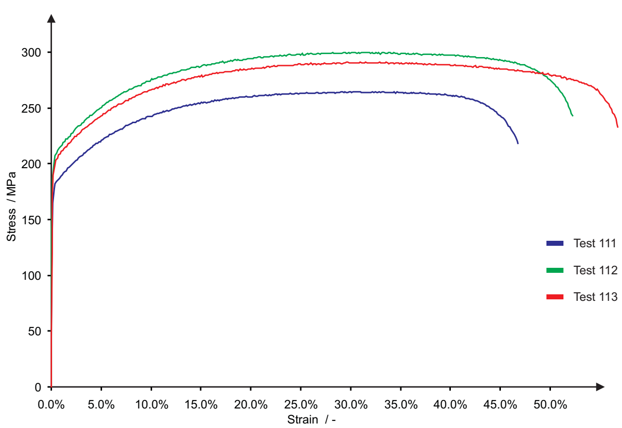

Graph B.1: Engineering Stress-Strain Curves of Tensile Tests 111 - 113

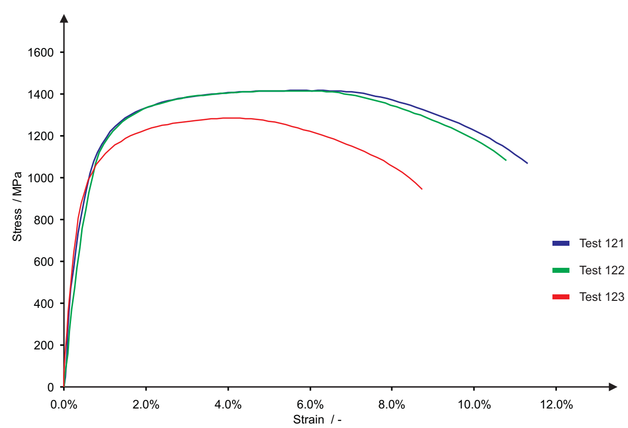

Graph B.2: Engineering Stress-Strain Curves of Tensile Tests 121 - 123

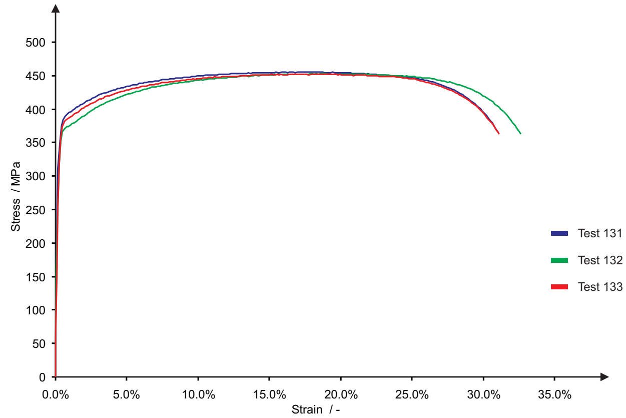

<u>Graph B.3:</u> Engineering Stress-Strain Curves of Tensile Tests 131 - 133

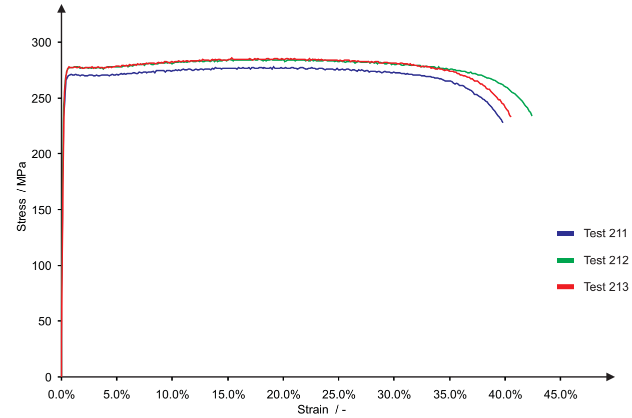

<u>Graph B.4:</u> Engineering Stress-Strain Curves of Tensile Tests 211 - 213

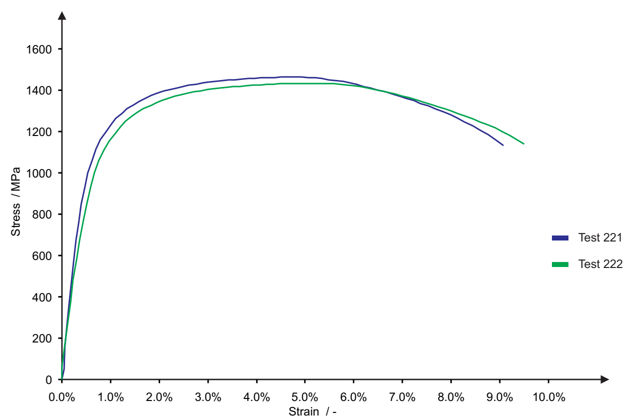

<u>Graph B.5:</u> Engineering Stress-Strain Curves of Tensile Tests 221 and 222

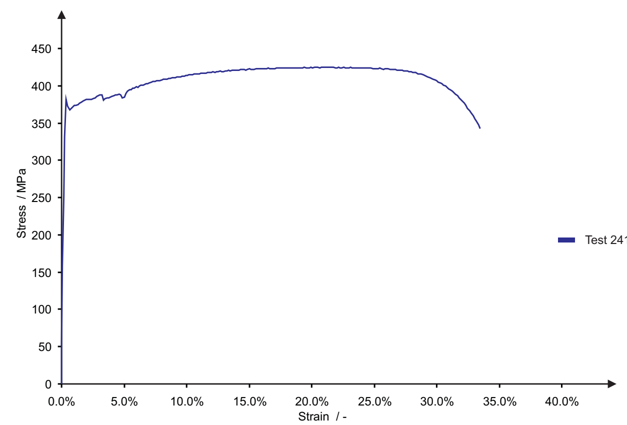

<u>Graph B.6:</u> Engineering Stress-Strain Curve of Tensile Test 241

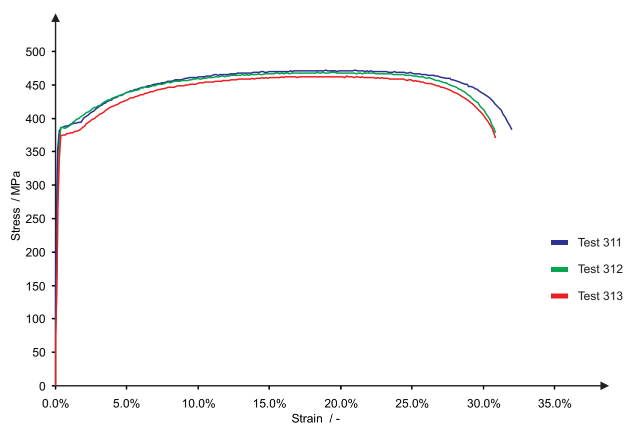

<u>Graph B.7:</u> Engineering Stress-Strain Curves of Tensile Tests 311 - 313

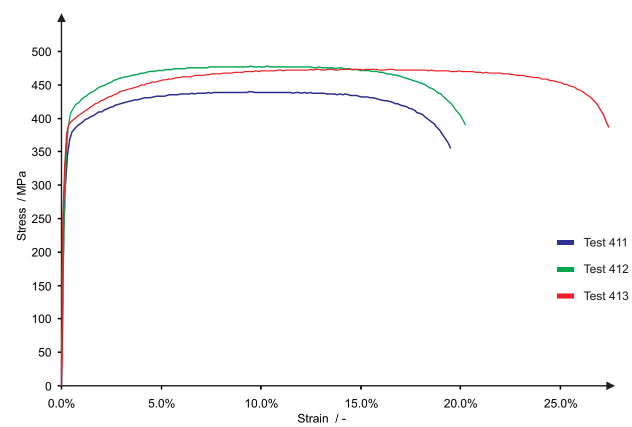

<u>Graph B.8:</u> Engineering Stress-Strain Curves of Tensile Tests 411 - 413

C Derived material cards from tensile tests

A-Pillar outer layer

```
*MAT_PIECEWISE_LINEAR_PLASTICITY_TITLE
Apillar outer
$#     mid        ro         e        pr      sigy      etan      fail      tdel
   4000000 7.8900E-9 2.1000E+5  0.300000       180     0.000  0.560000     0.000
$#       c         p      lcss      lcsr        vp
     252.5      3.89   4000000         0     0.000
$#    eps1      eps2      eps3      eps4      eps5      eps6      eps7      eps8
     0.000     0.000     0.000     0.000     0.000     0.000     0.000     0.000
$#     es1       es2       es3       es4       es5       es6       es7       es8
     0.000     0.000     0.000     0.000     0.000     0.000     0.000     0.000
*DEFINE_CURVE
$#    lcid      sidr       sfa       sfo      offa      offo    dattyp
   4000000         0  1.000000  1.000000     0.000     0.000         0
$#                a1                  o1
               0.004             182.627
               0.021             204.362
               0.039             222.309
               0.055             237.017
               0.072             250.883
               0.088             262.537
               0.104             272.216
               0.120             281.998
               0.135             289.885
               0.150             297.778
               0.165             305.641
               0.180             311.510
               0.195             317.545
               0.209             323.239
               0.223             329.201
               0.238             334.130
               0.251             338.858
               0.265             344.741
               0.278             348.790
               0.292             353.087
               0.305             356.772
               0.318             361.119
               0.331             364.575
               1.000             365.000
```

A-Pillar reinforcement layer

```
*MAT_PIECEWISE_LINEAR_PLASTICITY_TITLE
Apillar reinforcement
$#     mid        ro         e        pr      sigy      etan      fail      tdel
   4000001 7.8900E-9 2.1000E+5  0.300000  940.0000     0.000  0.100000     0.000
$#       c         p      lcss      lcsr        vp
    6.2E+9      4.28   4000001         0     0.000
$#    eps1      eps2      eps3      eps4      eps5      eps6      eps7      eps8
     0.000     0.000     0.000     0.000     0.000     0.000     0.000     0.000
$#     es1       es2       es3       es4       es5       es6       es7       es8
     0.000     0.000     0.000     0.000     0.000     0.000     0.000     0.000
*DEFINE_CURVE
$#    lcid      sidr       sfa       sfo      offa      offo    dattyp
   4000001         0  1.000000  1.000000     0.000     0.000         0
$#                a1                  o1
               0.000             940.000
```

```
                  0.006            943.575
                  0.007           1038.296
                  0.008           1114.898
                  0.010           1171.574
                  0.011           1214.892
                  0.012           1251.855
                  0.014           1281.989
                  0.016           1307.831
                  0.017           1330.398
                  0.019           1349.538
                  0.020           1365.284
                  0.022           1379.685
                  0.024           1391.715
                  0.025           1402.687
                  0.027           1412.415
                  0.029           1421.650
                  0.030           1429.461
                  0.032           1436.974
                  0.034           1443.084
                  0.035           1449.632
                  0.037           1455.423
                  0.039           1461.098
                  0.040           1465.240
                  0.042           1470.148
                  0.044           1474.236
                  0.045           1478.285
                  0.047           1481.878
                  0.049           1485.422
                  0.051           1488.470
                  0.052           1491.385
                  0.054           1494.211
                  0.056           1496.573
                  1.000           1500.000
```

A-Pillar inner layer

```
*MAT_PIECEWISE_LINEAR_PLASTICITY_TITLE
Apillar inner
$#     mid        ro         e        pr      sigy      etan      fail      tdel
   4000002 7.8900E-9 2.1000E+5  0.300000  450.0000     0.000  0.210000     0.000
$#       c         p      lcss      lcsr        vp
    2211.9      2.38   4000002         0     0.000
$#    eps1      eps2      eps3      eps4      eps5      eps6      eps7      eps8
     0.000     0.000     0.000     0.000     0.000     0.000     0.000     0.000
$#     es1       es2       es3       es4       es5       es6       es7       es8
     0.000     0.000     0.000     0.000     0.000     0.000     0.000     0.000
*DEFINE_CURVE
$#    lcid      sidr       sfa       sfo      offa      offo    dattyp
   4000002         0  1.000000  1.000000     0.000     0.000         0
$#                  a1                  o1
                 0.000             450.000
                 0.049             455.716
                 0.065             471.142
                 0.082             484.286
                 0.098             496.121
                 0.114             506.758
                 0.129             516.452
                 0.145             525.449
                 0.160             533.769
                 0.175             541.619
                 1.000             550.000
```

B-Pillar reinforcement layer

```
*MAT_PIECEWISE_LINEAR_PLASTICITY_TITLE
Bpillar reinforcement
$#     mid        ro         e        pr      sigy      etan      fail      tdel
   4000003 7.8900E-9 2.1000E+5  0.300000  940.0000     0.000  0.090000     0.000
$#       c         p      lcss      lcsr        vp
    6.2E+9      4.28   4000003         0     0.000
$#    eps1      eps2      eps3      eps4      eps5      eps6      eps7      eps8
     0.000     0.000     0.000     0.000     0.000     0.000     0.000     0.000
$#     es1       es2       es3       es4       es5       es6       es7       es8
     0.000     0.000     0.000     0.000     0.000     0.000     0.000     0.000
*DEFINE_CURVE
$#    lcid      sidr       sfa       sfo      offa      offo    dattyp
   4000003         0  1.000000  1.000000     0.000     0.000         0
$#                a1                  o1
               0.000             940.000
               0.006             948.346
               0.007            1034.992
               0.008            1107.066
               0.010            1165.686
               0.011            1213.453
               0.013            1254.464
               0.014            1288.228
               0.015            1316.471
               0.017            1340.805
               0.019            1361.427
               0.020            1379.353
               0.022            1394.260
               0.024            1408.418
               0.025            1419.579
               0.027            1430.575
               0.029            1440.411
               0.030            1448.422
               0.032            1456.375
               0.034            1462.832
               0.035            1469.252
               0.037            1475.293
               0.039            1480.976
               0.041            1485.982
               0.042            1490.471
               0.044            1494.633
               0.045            1498.077
               0.047            1501.897
               0.049            1504.366
               0.050            1507.106
               1.000            1510.000
```

B-Pillar inner layer

```
*MAT_PIECEWISE_LINEAR_PLASTICITY_TITLE
Bpillar inner
$#     mid        ro         e        pr      sigy      etan      fail      tdel
   4000004 7.8900E-9 2.1000E+5  0.300000  380.0000     0.000  0.330000     0.000
$#       c         p      lcss      lcsr        vp
    2211.9      2.38   4000004         0     0.000
$#    eps1      eps2      eps3      eps4      eps5      eps6      eps7      eps8
     0.000     0.000     0.000     0.000     0.000     0.000     0.000     0.000
$#     es1       es2       es3       es4       es5       es6       es7       es8
     0.000     0.000     0.000     0.000     0.000     0.000     0.000     0.000
*DEFINE_CURVE
$#    lcid      sidr       sfa       sfo      offa      offo    dattyp
   4000004         0  1.000000  1.000000     0.000     0.000         0
$#                a1                  o1
               0.000             380.000
```

```
                 0.014           381.210
                 0.026           393.090
                 0.038           399.748
                 0.050           408.649
                 0.061           426.126
                 0.073           436.887
                 0.084           446.838
                 0.096           455.520
                 0.107           463.504
                 0.118           470.923
                 0.129           478.539
                 0.139           485.699
                 0.150           491.600
                 0.161           498.007
                 0.171           503.319
                 0.182           508.929
                 0.192           514.640
                 0.202           519.134
                 0.212           523.692
                 1.000           530.000
```

Roof rail front

```
*MAT_PIECEWISE_LINEAR_PLASTICITY_TITLE
roof front
$#     mid        ro         e        pr      sigy      etan      fail      tdel
   4000005 7.8900E-9 2.1000E+5  0.300000  380.0000     0.000  0.300000     0.000
$#       c         p      lcss      lcsr        vp
    2211.9      2.38   4000005         0     0.000
$#    eps1      eps2      eps3      eps4      eps5      eps6      eps7      eps8
     0.000     0.000     0.000     0.000     0.000     0.000     0.000     0.000
$#     es1       es2       es3       es4       es5       es6       es7       es8
     0.000     0.000     0.000     0.000     0.000     0.000     0.000     0.000
*DEFINE_CURVE
$#    lcid      sidr       sfa       sfo      offa      offo    dattyp
   4000005         0  1.000000  1.000000     0.000     0.000         0
$#                a1                  o1
                 0.000           380.000
                 0.009           391.293
                 0.021           416.904
                 0.033           437.865
                 0.045           455.522
                 0.057           468.422
                 0.068           480.859
                 0.080           492.303
                 0.091           501.250
                 0.102           510.196
                 0.113           518.204
                 0.124           526.806
                 0.135           533.645
                 0.146           540.351
                 0.157           546.367
                 0.167           552.881
                 0.178           559.203
                 0.188           564.354
                 0.198           569.687
                 1.000           575.000
```

Roof rail middle

```
*MAT_PIECEWISE_LINEAR_PLASTICITY_TITLE
roof middle
$#     mid        ro         e        pr      sigy      etan      fail      tdel
   4000006 7.8900E-9 2.1000E+5  0.300000  380.0000     0.000  0.200000     0.000
$#       c         p      lcss      lcsr        vp
    2211.9      2.38   4000006         0     0.000
$#    eps1      eps2      eps3      eps4      eps5      eps6      eps7      eps8
     0.000     0.000     0.000     0.000     0.000     0.000     0.000     0.000
$#     es1       es2       es3       es4       es5       es6       es7       es8
     0.000     0.000     0.000     0.000     0.000     0.000     0.000     0.000
*DEFINE_CURVE
$#    lcid      sidr       sfa       sfo      offa      offo    dattyp
   4000006         0  1.000000  1.000000     0.000     0.000         0
$#                a1                  o1
               0.000             380.000
               0.003             387.617
               0.012             437.788
               0.020             457.696
               0.029             472.965
               0.037             483.997
               0.046             492.519
               0.054             500.039
               0.063             506.096
               0.071             511.232
               0.079             516.029
               0.087             520.563
               0.095             524.326
               1.000             530.000
```

D Additional pictures and graphs of the simulations

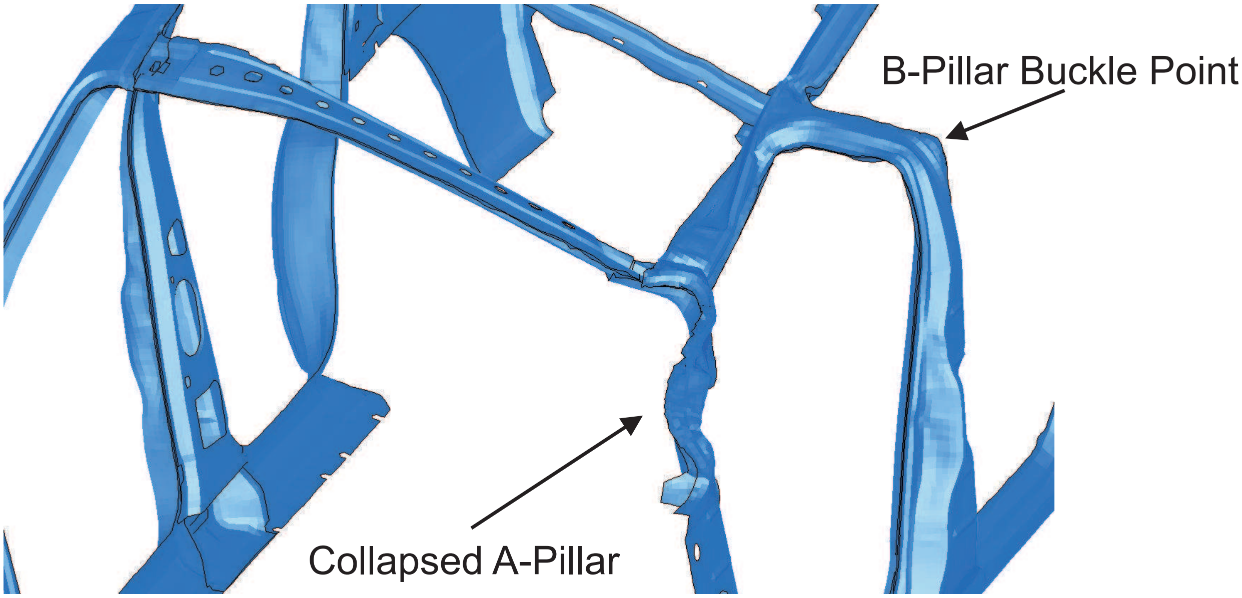

Figure D.1: Structural components of the collapsed roof in the baseline simulation

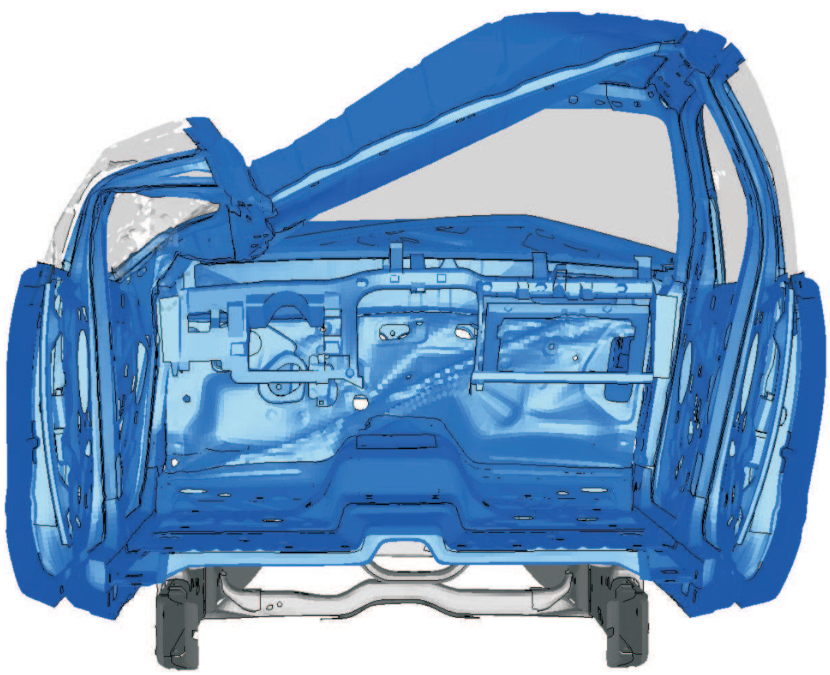

Figure D.2: Interior view of the baseline simulation

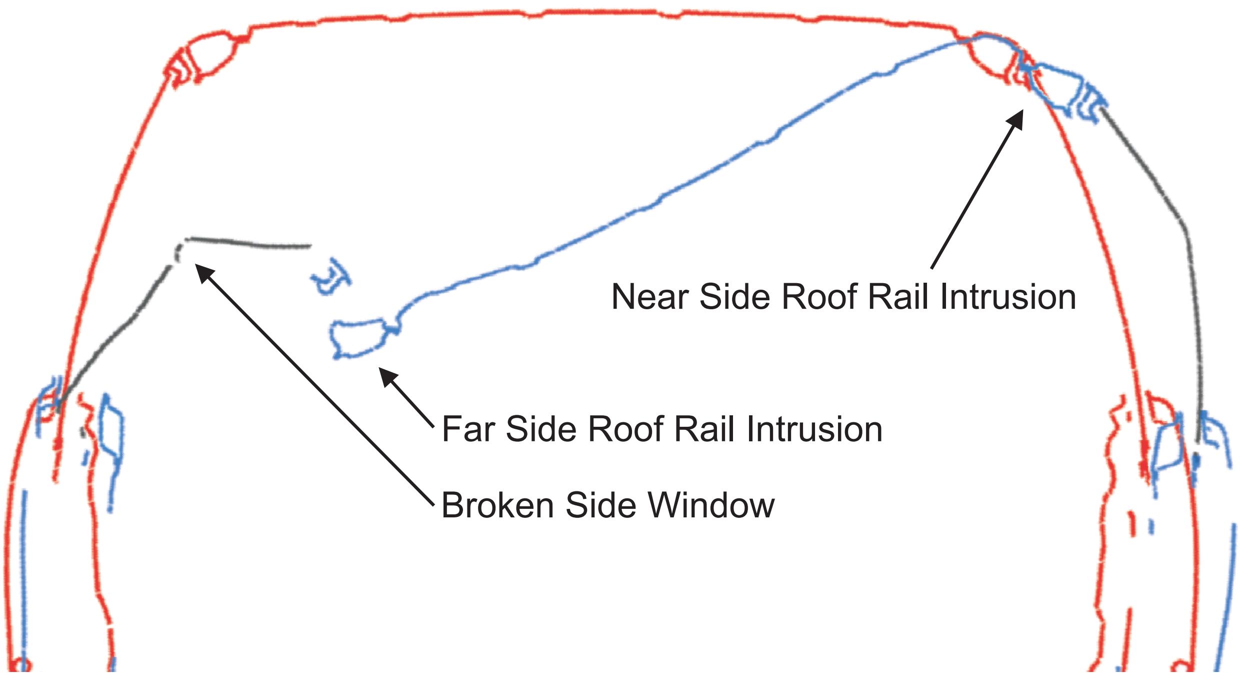

Figure D.3: Section cut at the position of a driver's body

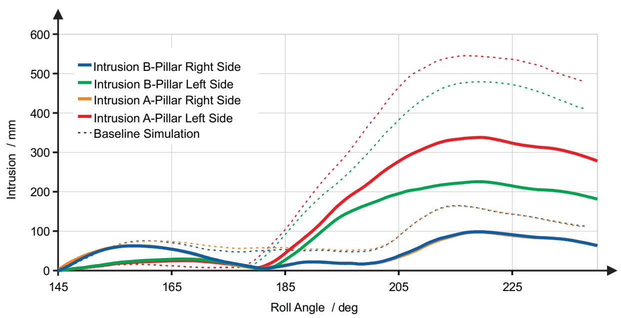

Graph D.1: Roof intrusion of near side elastic impact

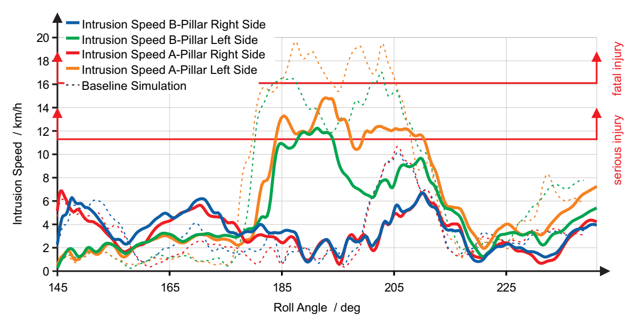

Graph D.2: Roof intrusion velocity of near side elastic impact

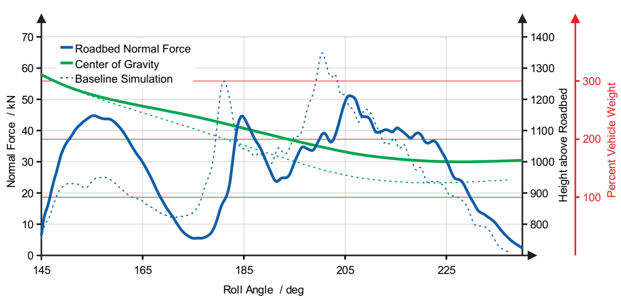

Graph D.3: Roadbed load and center of gravity of near side elastic impact

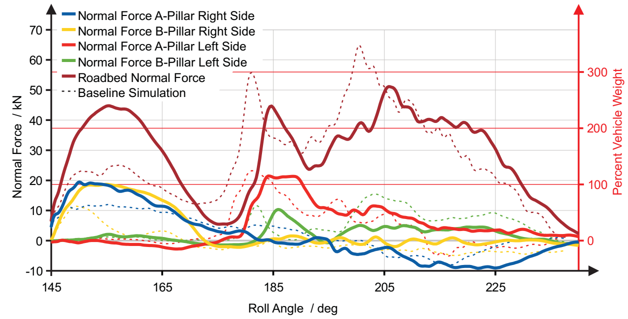

Graph D.4: Section forces of near side elastic impact

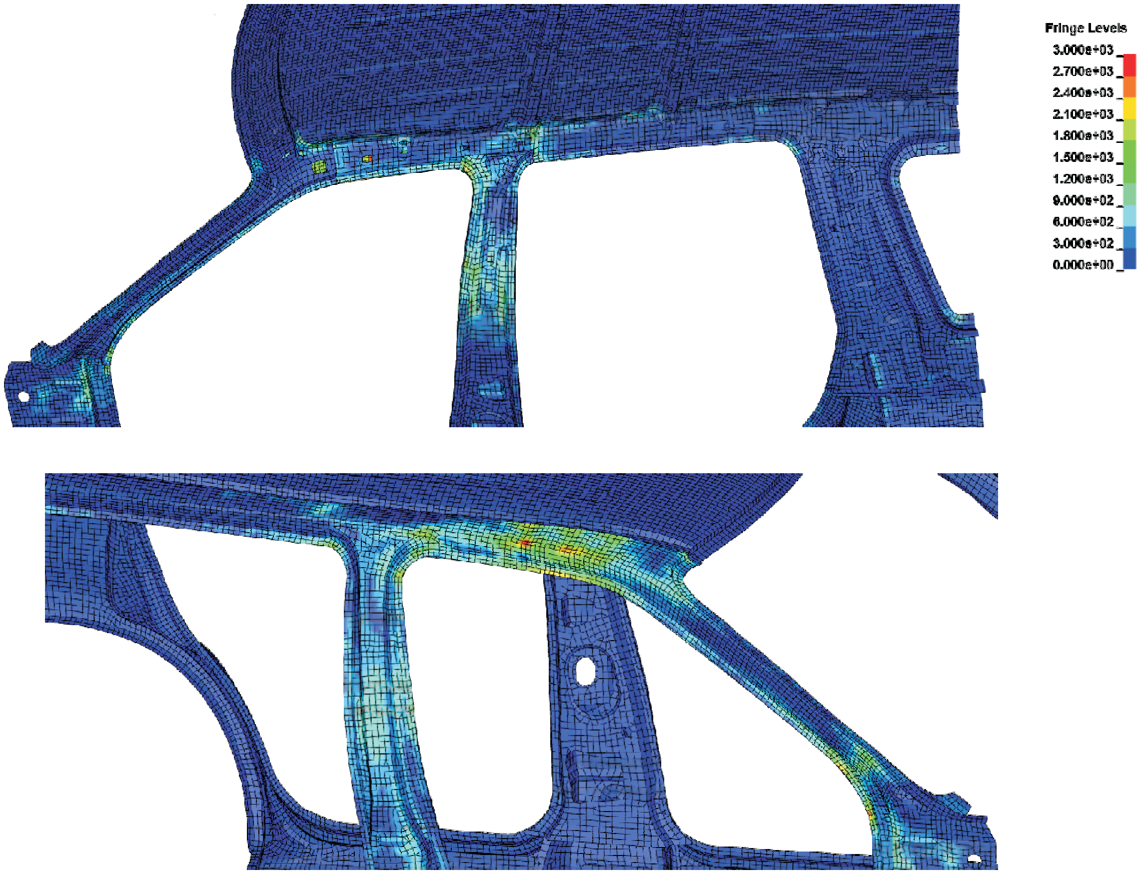

Figure D.4: Von Mises stress fringe plot of the near side roof structural components at peak load

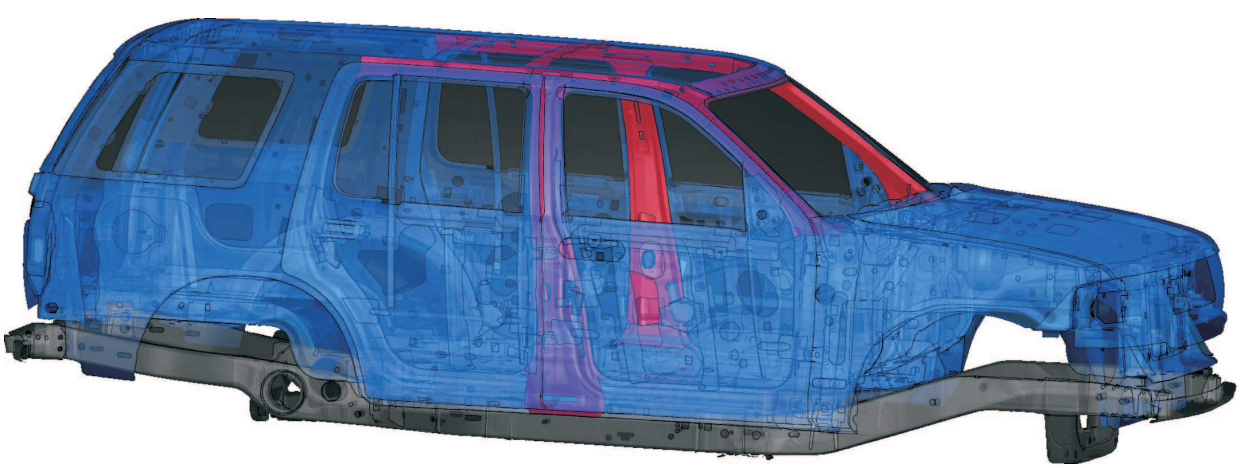

Figure D.5: Upgraded and upgaged parts (red) for the material upgrade simulation

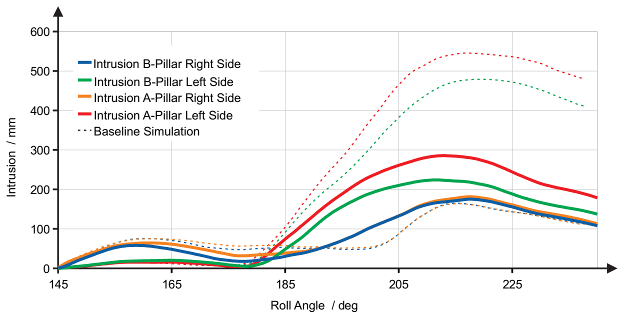

Graph D.5: Roof intrusion of material upgrade simulation

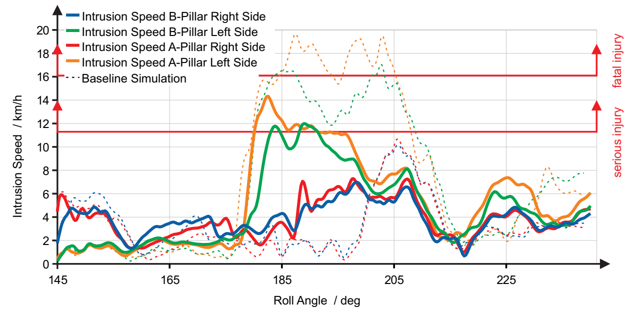

Graph D.6: Roof intrusion velocity of material upgrade simulation

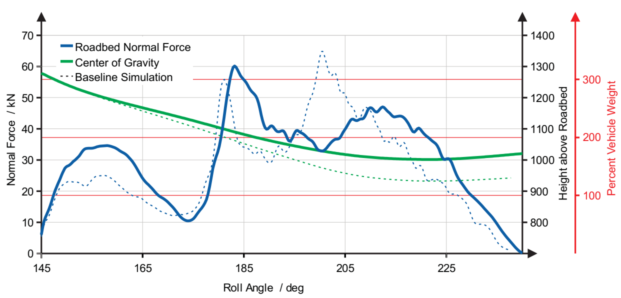

Graph D.7: Roadbed load and center of gravity of material upgrade simulation

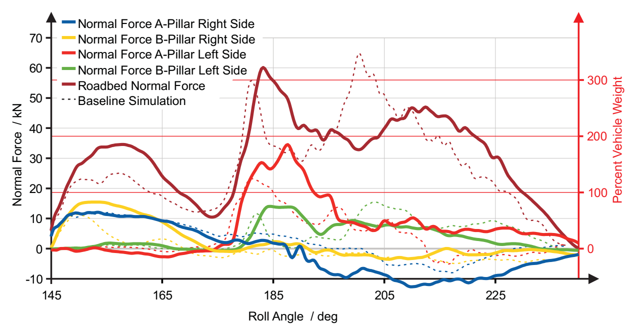

Graph D.8: Section forces of material upgrade simulation

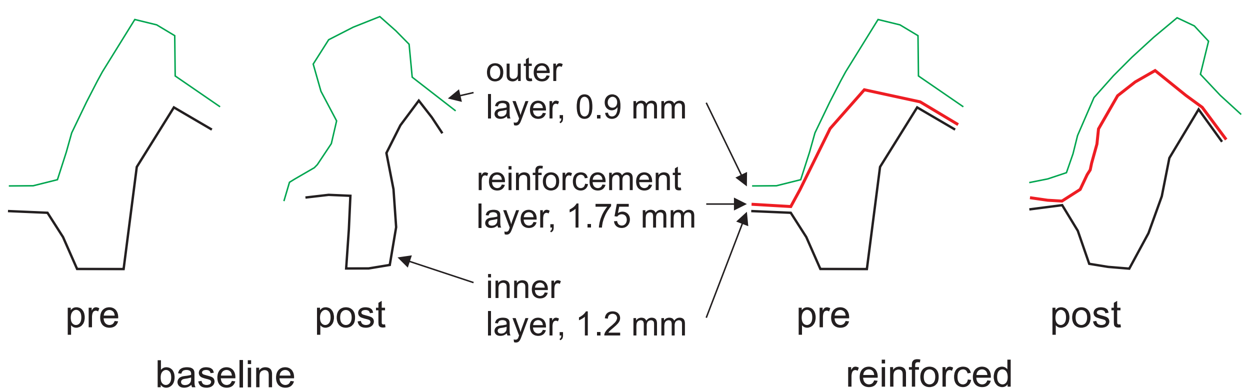

Figure D.6: Comparison of the baseline and reinforced A-pillar crosssection

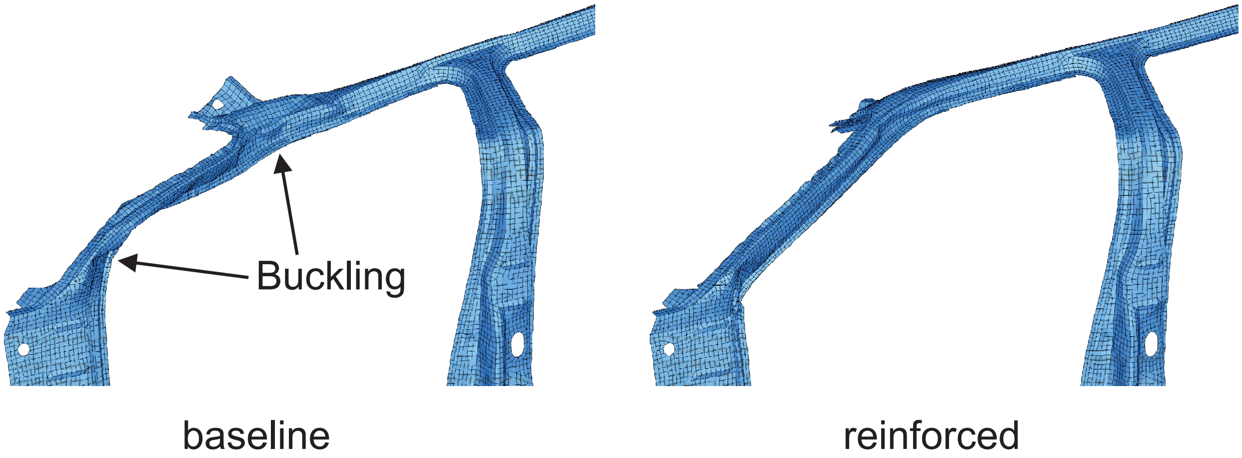

Figure D.7: Structure of the baseline and reinforced roof, points of buckling marked

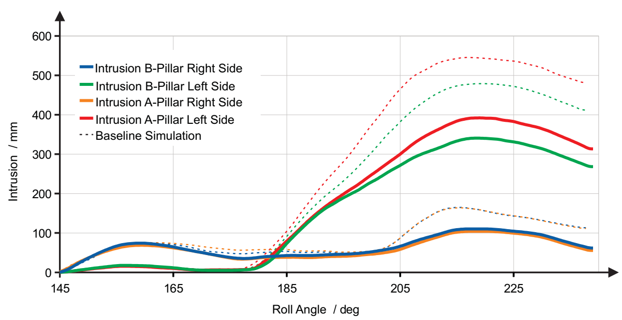

Graph D.9: Roof intrusion (JRS rollover test) of A-pillar reinforced simulation

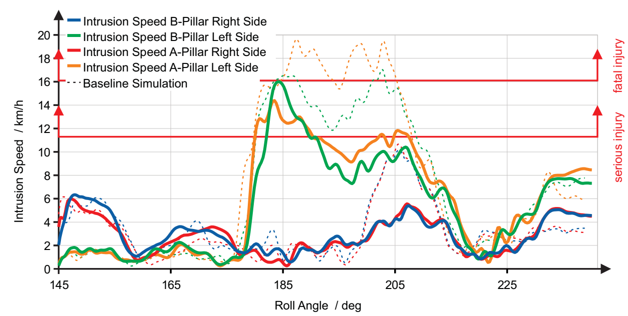

Graph D.10: Roof intrusion velocity (JRS rollover test) of A-pillar reinforced simulation

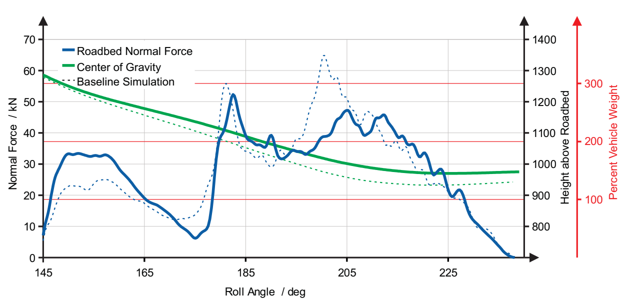

Graph D.11: Roadbed load and center of gravity (JRS rollover test) of A-pillar reinforced simulation

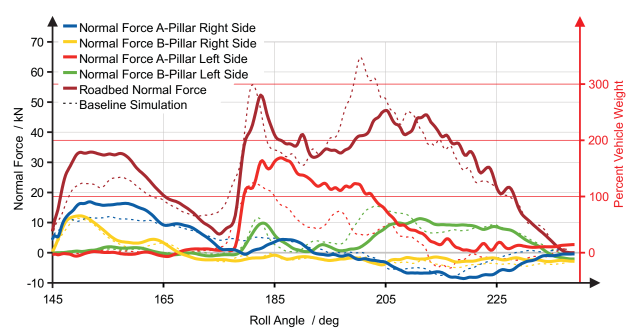

Graph D.12: Section forces (JRS rollover test) of A-pillar reinforced simulation

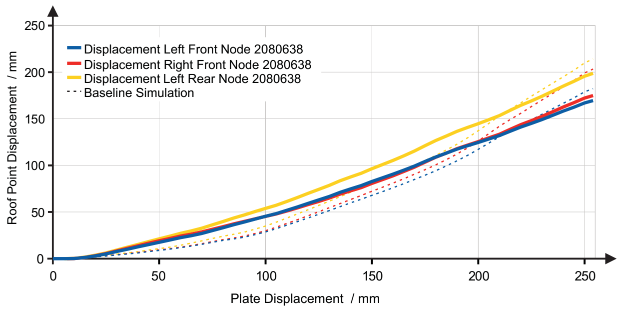

Graph D.13: Dummy head point displacement (static roof crush test) of A-pillar reinforced simulation

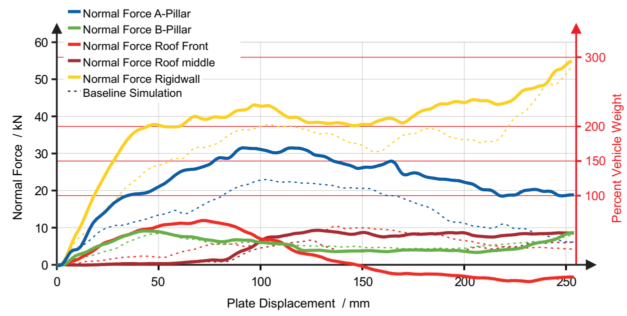

Graph D.14: Section forces (static roof crush test) of A-pillar reinforced simulation

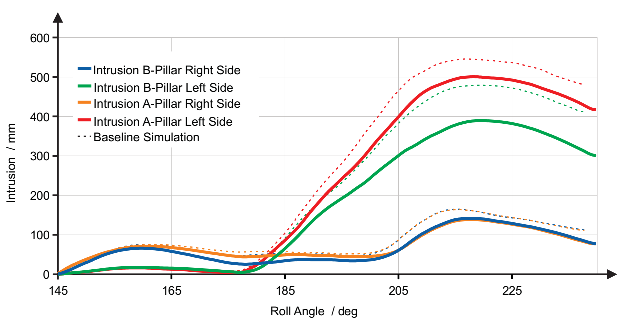

Graph D.15: Roof intrusion (JRS rollover test) of B-pillar reinforced simulation

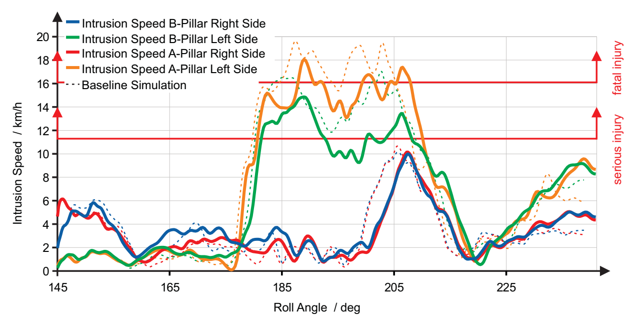

Graph D.16: Roof intrusion velocity (JRS rollover test) of B-pillar reinforced simulation

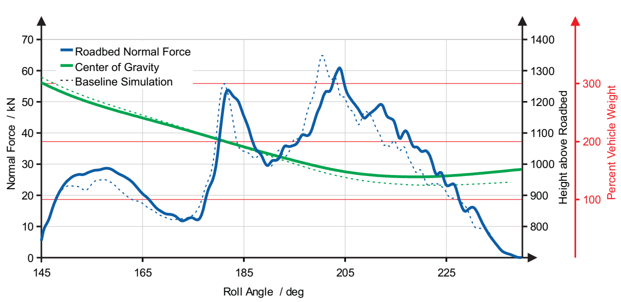

Graph D.17: Roadbed load and center of gravity (JRS rollover test) of B-pillar reinforced simulation

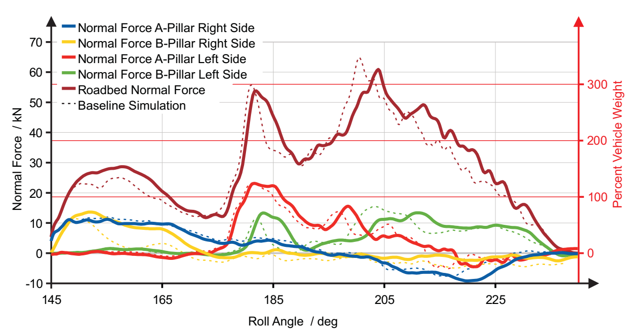

Graph D.18: Section forces (JRS rollover test) of B-pillar reinforced simulation

Figure D.8: Exploded view of the reinforced B-pillar. Second layer from left is the added reinforcement

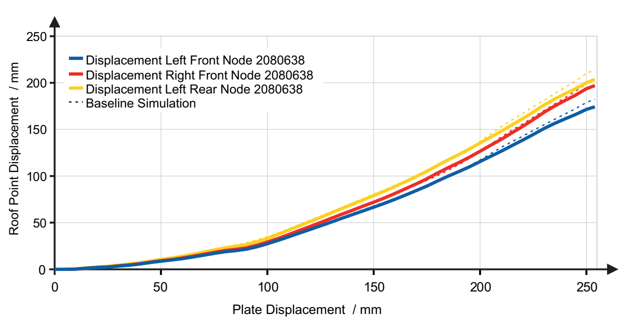

Graph D.19: Dummy head point displacement (static roof crush test) of B-pillar reinforced simulation

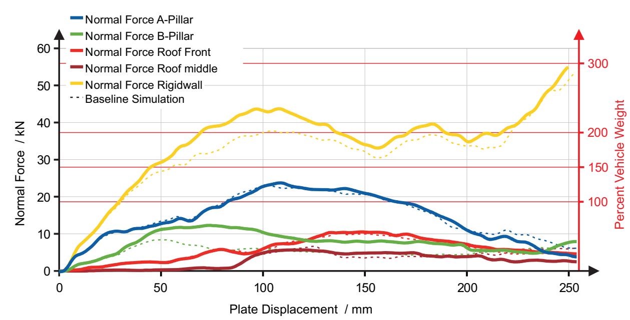

Graph D.20: Section forces (static roof crush test) of B-pillar reinforced simulation

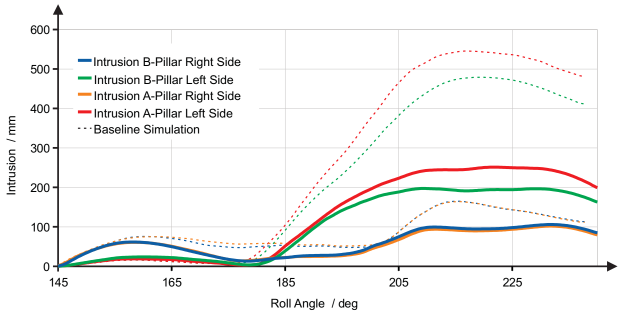

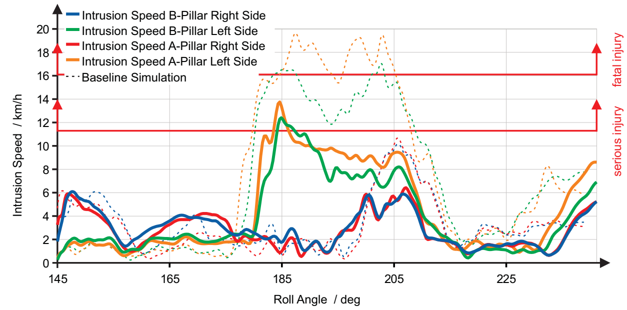

Graph D.21: Roof intrusion (JRS rollover test) of A-pillar and B-pillar reinforced simulation

Graph D.22: Roof intrusion velocity (JRS rollover test) of A-pillar and B-pillar reinforced simulation

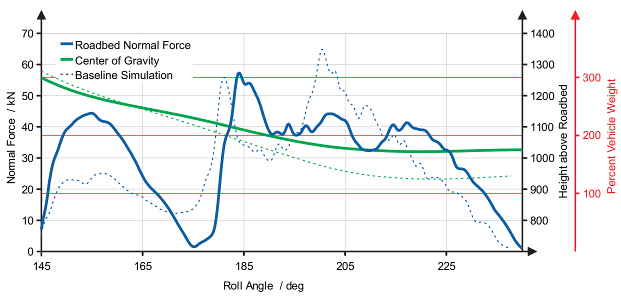

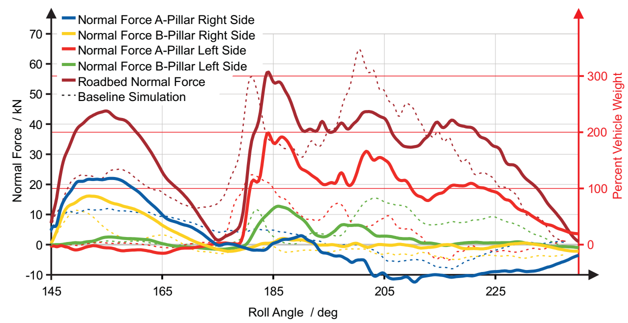

Graph D.23: Roadbed load and center of gravity (JRS rollover test) of A-pillar and B-pillar reinforced simulation

Graph D.24: Section forces (JRS rollover test) of A-pillar and B-pillar reinforced simulation

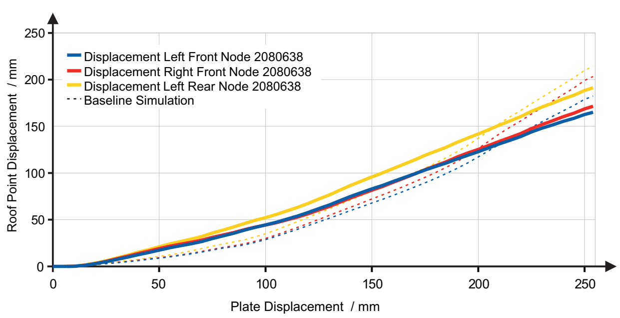

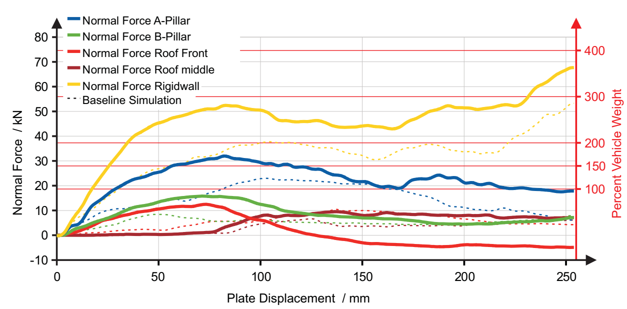

Graph D.25: Dummy head point displacement (static roof crush test) of A-pillar and B-pillar reinforced simulation

Graph D.26: Section forces (static roof crush test) of A-pillar and B-pillar reinforced simulation

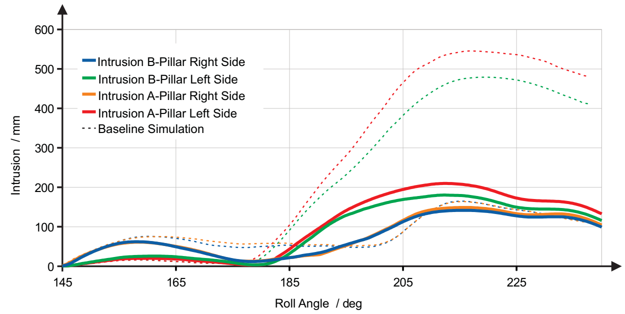

Graph D.27: Roof intrusion (JRS rollover test) of A-/B-pillar and window header reinforced simulation

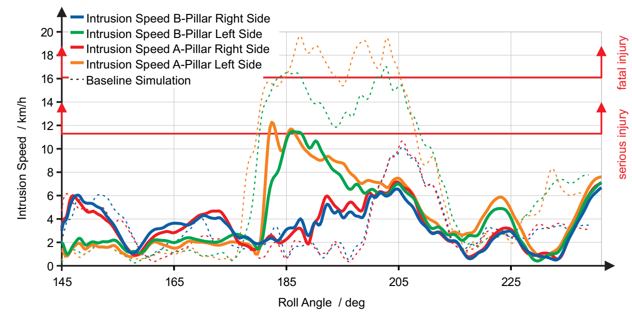

Graph D.28: Roof intrusion velocity (JRS rollover test) of A-/B-pillar and window header reinforced simulation

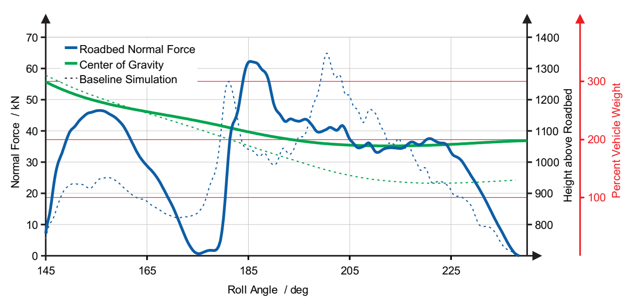

Graph D.29: Roadbed load and center of gravity (JRS rollover test) of A-/B-pillar and window header reinforced simulation

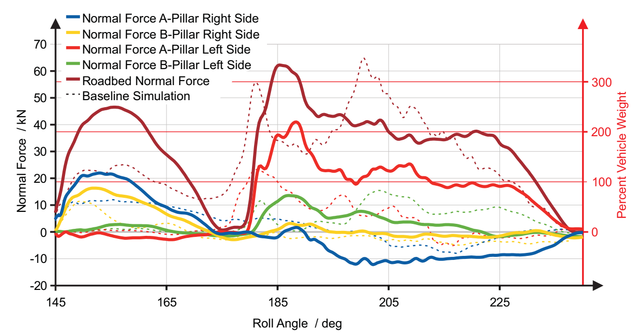

Graph D.30: Section forces (JRS rollover test) of A-/B-pillar and window header reinforced simulation

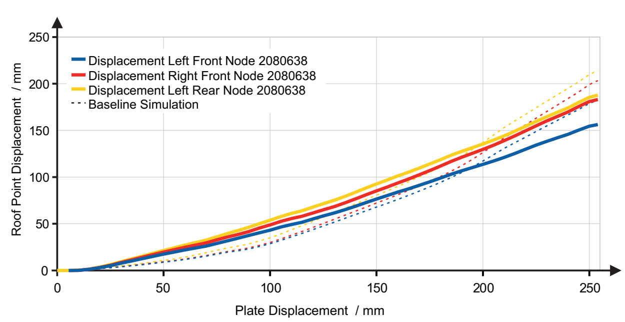

Graph D.31: Dummy head point displacement (static roof crush test) of A-/B-pillar and window header reinforced simulation

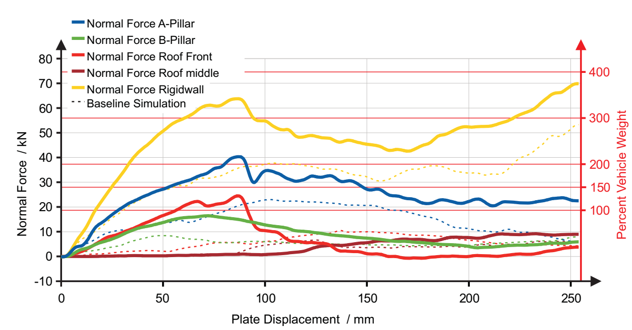

Graph D.32: Section forces (static roof crush test) of A-/B-pillar and window header reinforced simulation

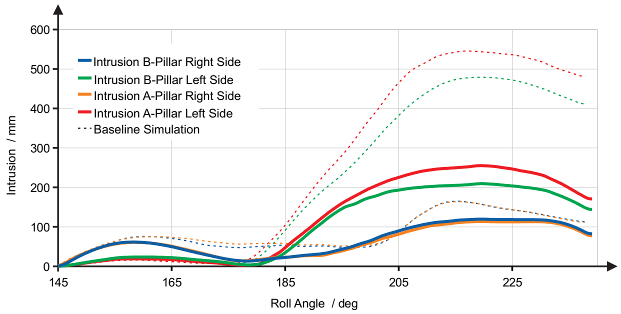

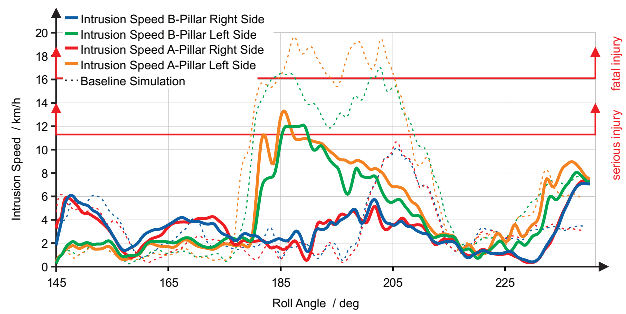

Graph D.33: Roof intrusion (JRS rollover test) of A-/B-pillar reinforced simulation with enlarged A-pillar

Graph D.34: Roof intrusion velocity (JRS rollover test) of A-/B-pillar reinforced simulation with enlarged A-pillar

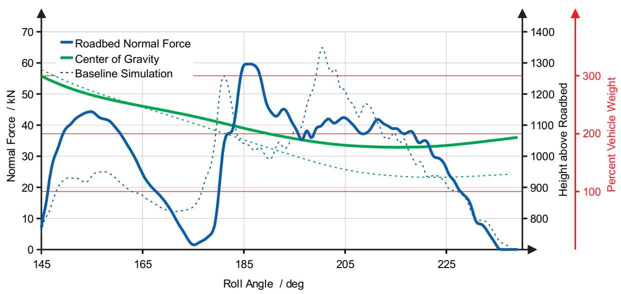

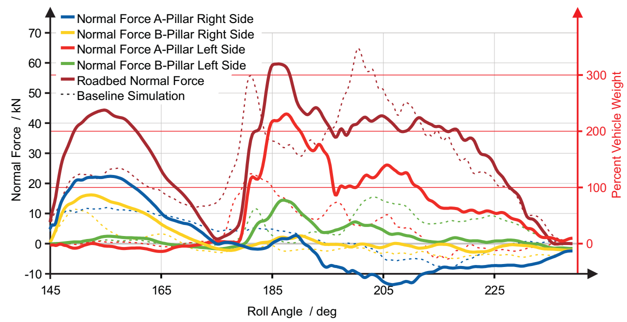

Graph D.35: Roadbed load and center of gravity (JRS rollover test) of A-/B-pillar reinforced simulation with enlarged A-pillar

Graph D.36: Section forces (JRS rollover test) of A-/B-pillar reinforced simulation with enlarged A-pillar

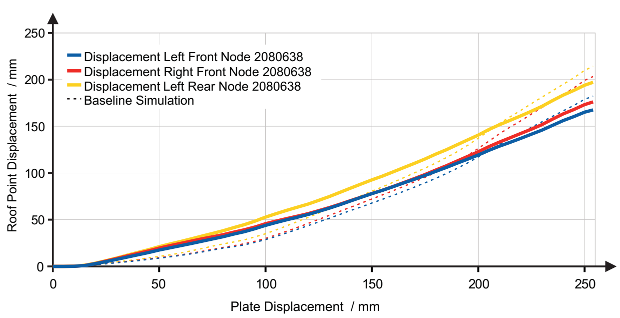

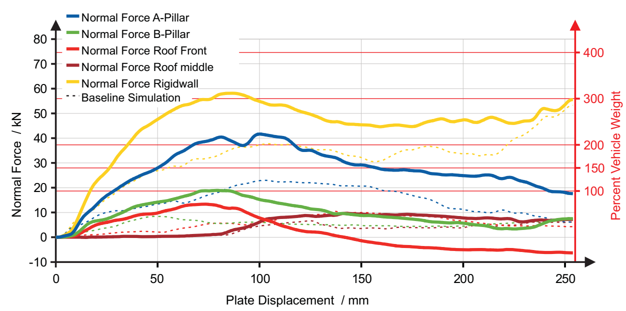

Graph D.37: Dummy head point displacement (static roof crush test) of A-/B-pillar reinforced simulation with enlarged A-pillar

Graph D.38: Section forces (static roof crush test) of A-/B-pillar reinforced simulation with enlarged A-pillar

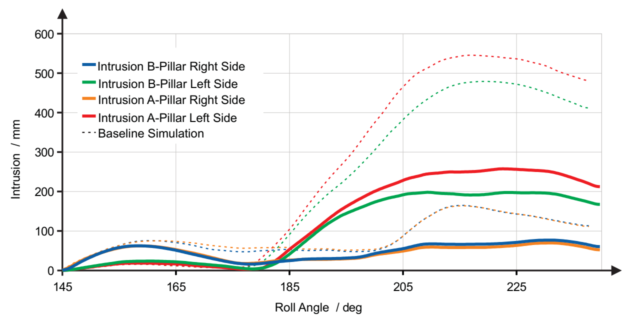

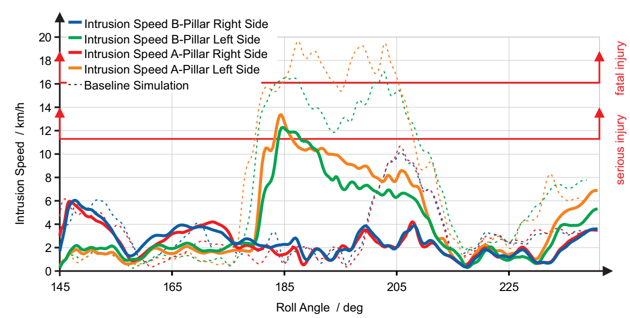

Graph D.39: Roof intrusion (JRS rollover test) of A-/B-pillar reinforced simulation with VW Tiguan material data

Graph D.40: Roof intrusion velocity (JRS rollover test) of A-/B-pillar reinforced simulation with VW Tiguan material data

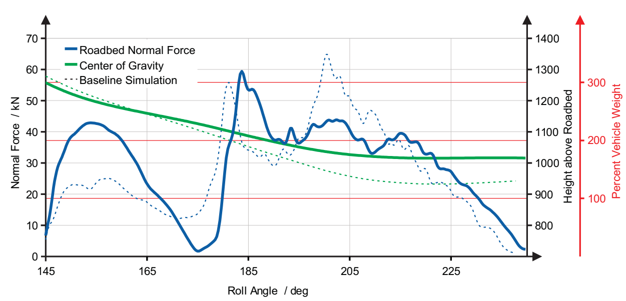

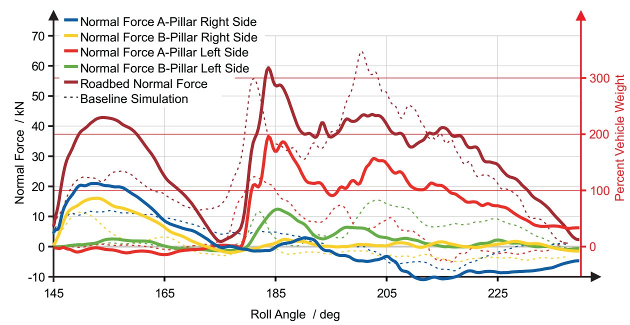

Graph D.41: Roadbed load and center of gravity (JRS rollover test) of A-/B-pillar reinforced simulation with VW Tiguan material data

Graph D.42: Section forces (JRS rollover test) of A-/B-pillar reinforced simulation with VW Tiguan material data

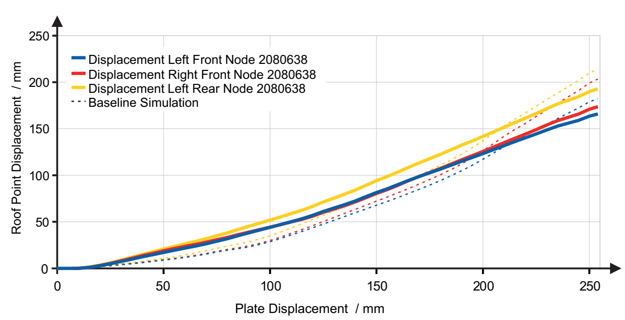

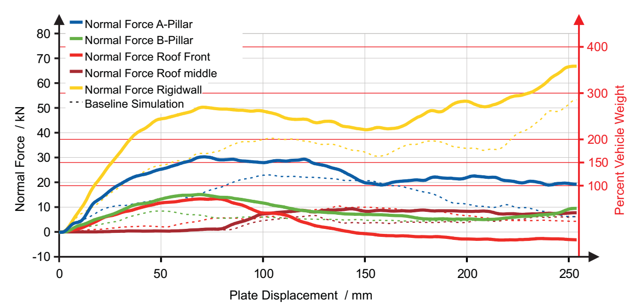

Graph D.43: Dummy head point displacement (static roof crush test) of A-/B-pillar reinforced simulation with VW Tiguan material data

Graph D.44: Section forces (static roof crush test) of A-/B-pillar reinforced simulation with VW Tiguan material data

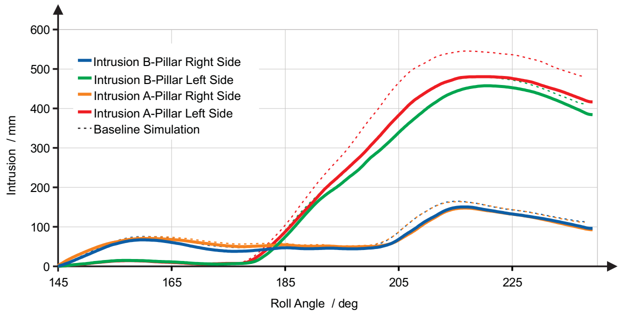

Graph D.45: Roof intrusion (JRS rollover test) of laser welded baseline simulation

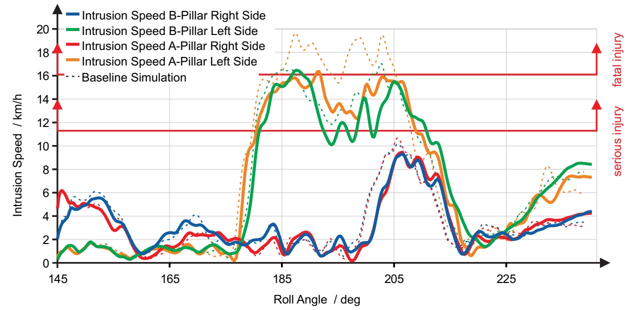

Graph D.46: Roof intrusion velocity (JRS rollover test) of laser welded baseline simulation

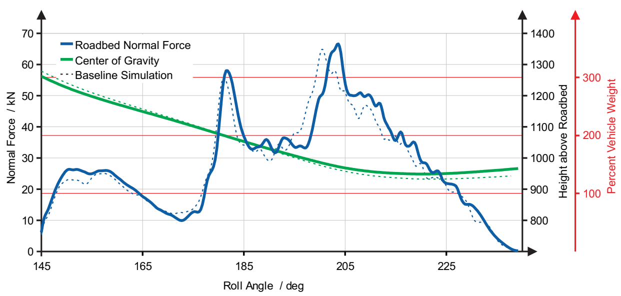

Graph D.47: Roadbed load and center of gravity (JRS rollover test) of laser welded baseline simulation

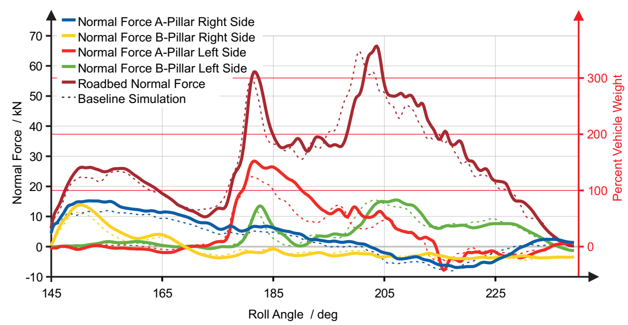

Graph D.48: Section forces (JRS rollover test) of laser welded baseline simulation

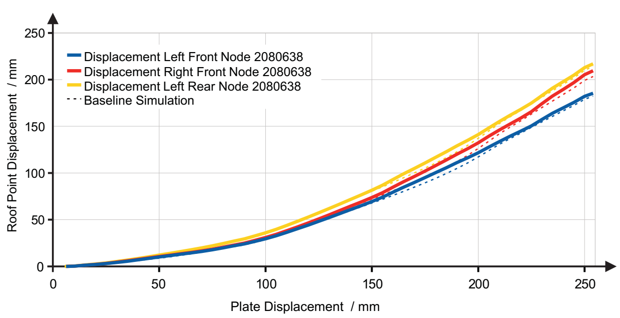

Graph D.49: Dummy head point displacement (static roof crush test) of laser welded baseline simulation

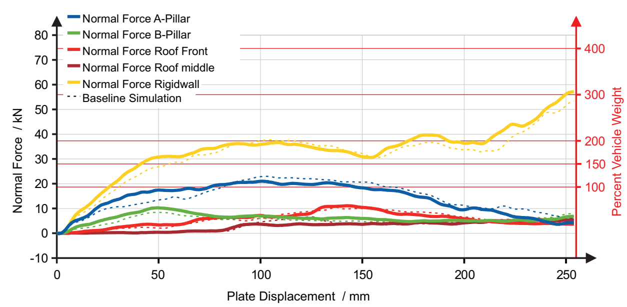

Graph D.50: Section forces (static roof crush test) of laser welded baseline simulation

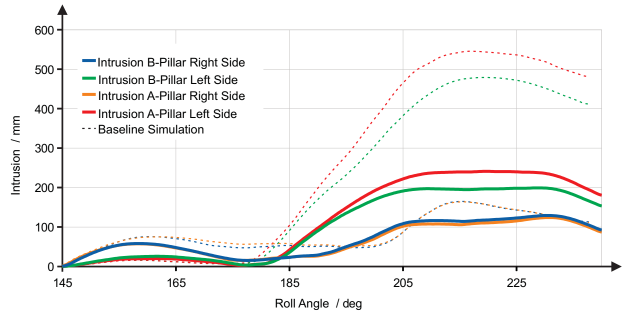

Graph D.51: Roof intrusion (JRS rollover test) of laserwelded A-/B-pillar reinforced simulation

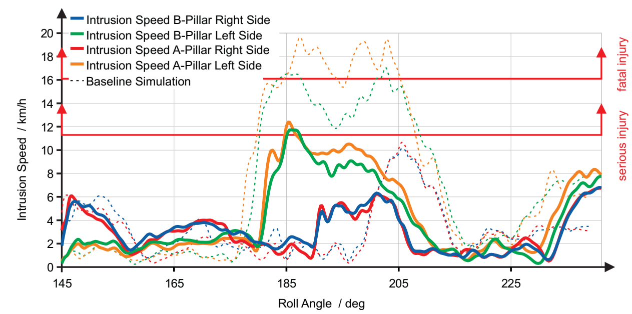

Graph D.52: Roof intrusion velocity (JRS rollover test) of laserwelded A-/B-pillar reinforced simulation

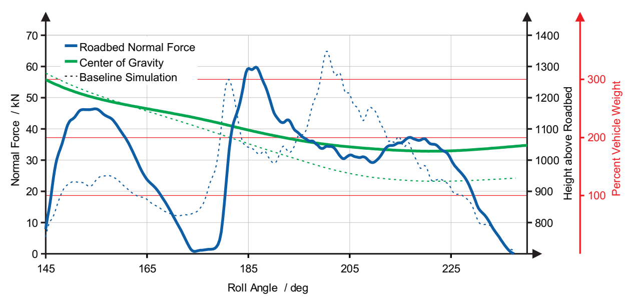

Graph D.53: Roadbed load and center of gravity (JRS rollover test) of laserwelded A-/B-pillar reinforced simulation

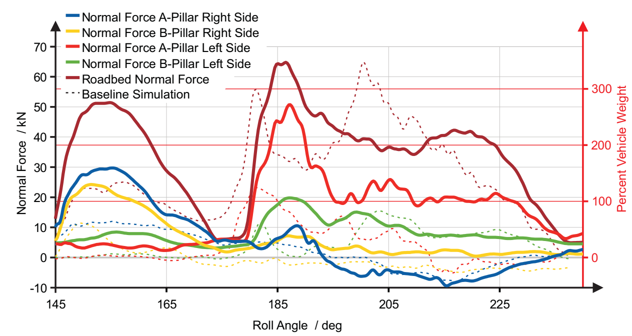

Graph D.54: Section forces (JRS rollover test) of laserwelded A-/B-pillar reinforced simulation

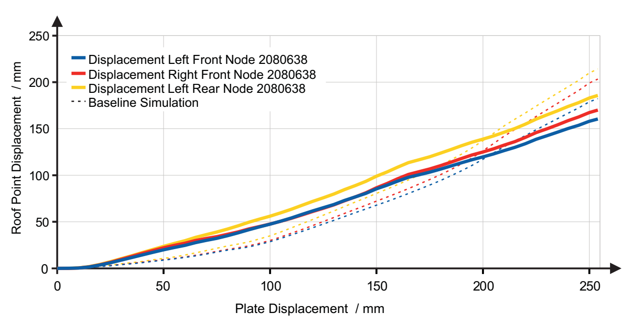

Graph D.55: Dummy head point displacement (static roof crush test) of laserwelded A-/B-pillar reinforced simulation

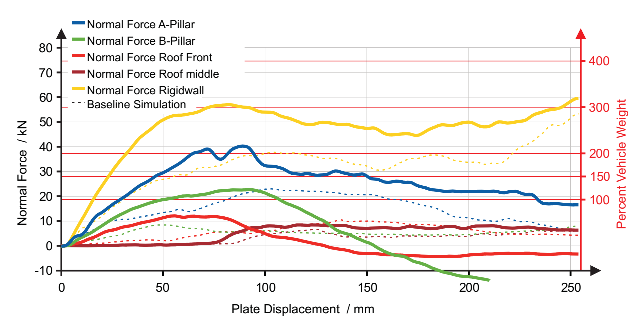

Graph D.56: Section forces (static roof crush test) of laserwelded A-/B-pillar reinforced simulation

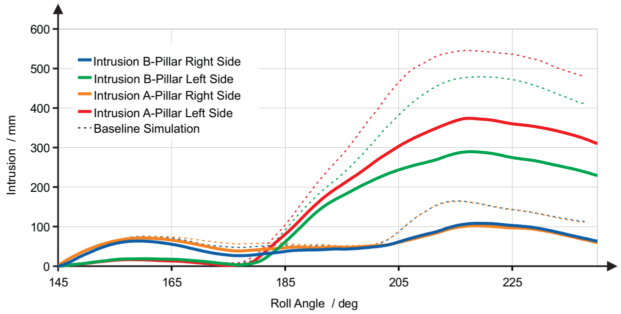

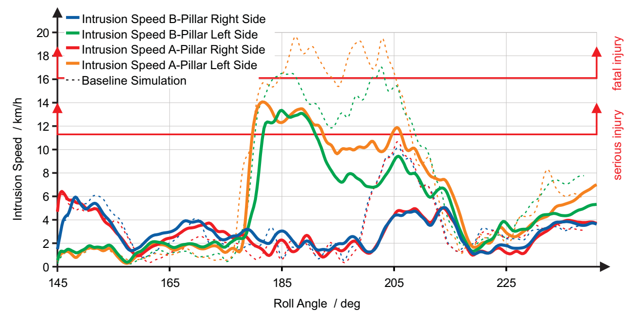

Graph D.57: Roof intrusion (JRS rollover test) of foam enhanced simulation

Graph D.58: Roof intrusion velocity (JRS rollover test) of foam enhanced simulation

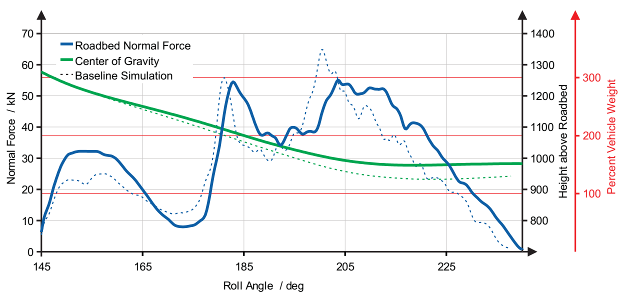

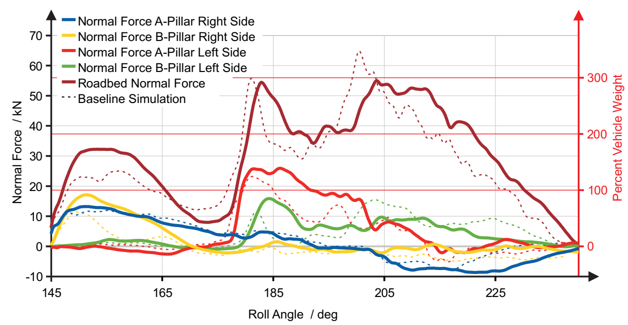

Graph D.59: Roadbed load and center of gravity (JRS rollover test) of foam enhanced simulation

Graph D.60: Section forces (JRS rollover test) of foam enhanced simulation

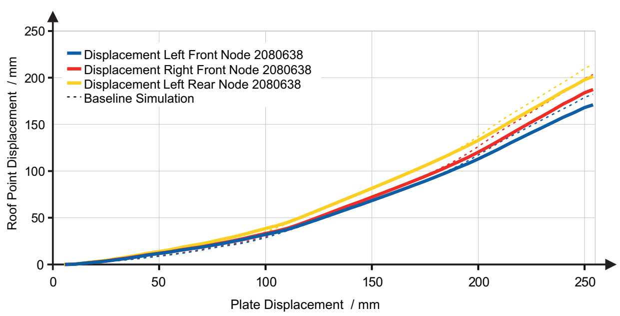

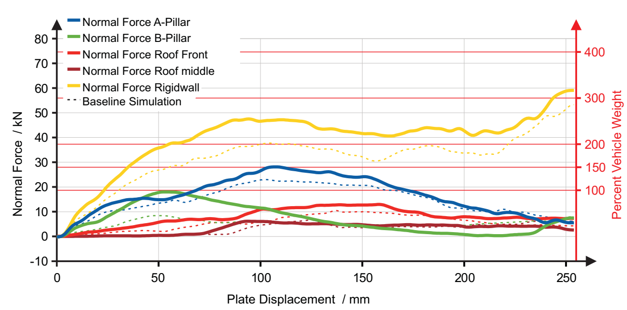

Graph D.61: Dummy head point displacement (static roof crush test) of foam enhanced simulation

Graph D.62: Section forces (static roof crush test) of foam enhanced simulation

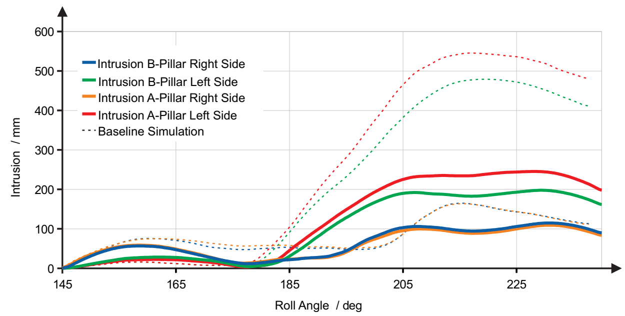

Graph D.63: Roof intrusion (JRS rollover test) of foam enhanced, A-/B-reinforced simulation

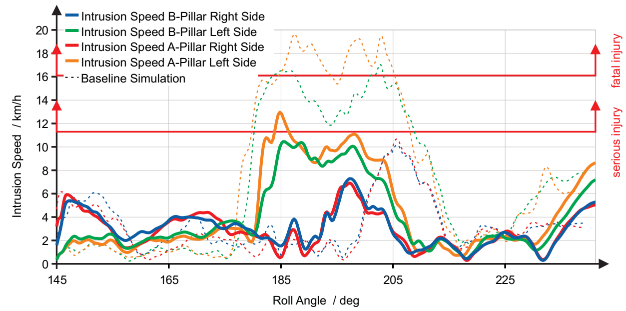

Graph D.64: Roof intrusion velocity (JRS rollover test) of foam enhanced, A-/B-reinforced simulation

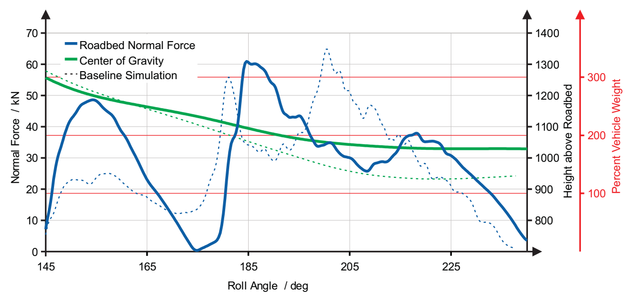

Graph D.65: Roadbed load and center of gravity (JRS rollover test) of foam enhanced, A-/B-reinforced simulation

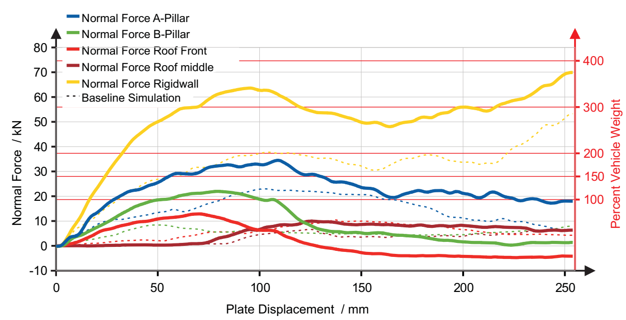

Graph D.66: Section forces (JRS rollover test) of foam enhanced, A-/B-reinforced simulation

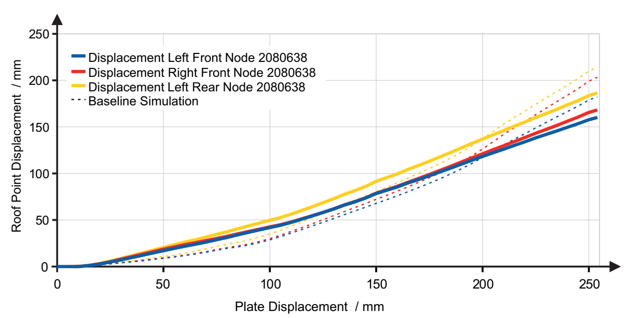

Graph D.67: Dummy head point displacement (static roof crush test) of foam enhanced, A-/B-reinforced simulation

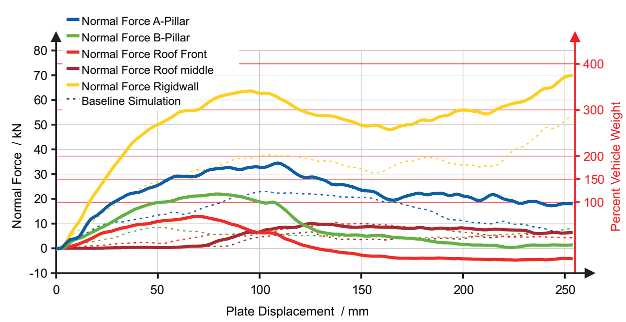

Graph D.68: Section forces (static roof crush test) of foam enhanced, A-/B-reinforced simulation

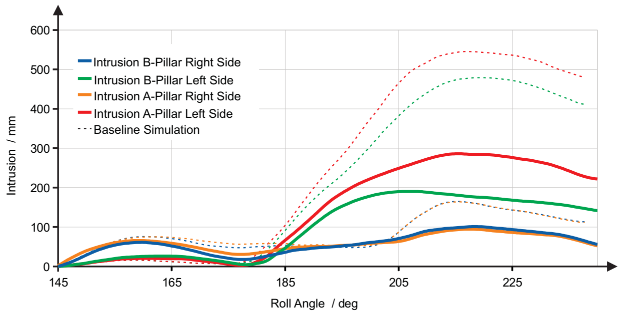

Graph D.69: Roof intrusion (JRS rollover test) of roll cage, 2 mm simulation

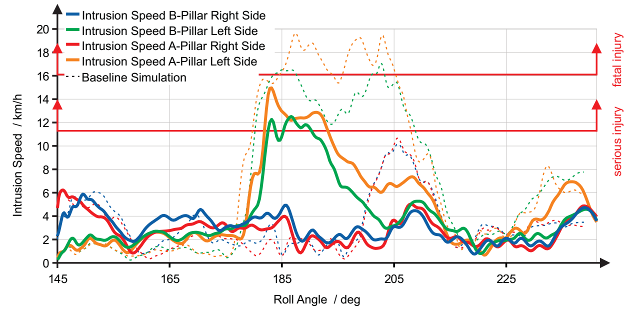

Graph D.70: Roof intrusion velocity (JRS rollover test) of roll cage, 2 mm simulation

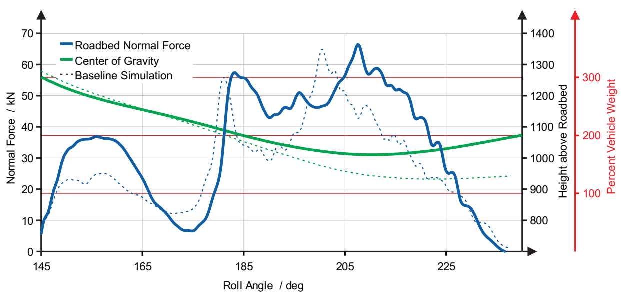

Graph D.71: Roadbed load and center of gravity (JRS rollover test) of roll cage, 2 mm simulation

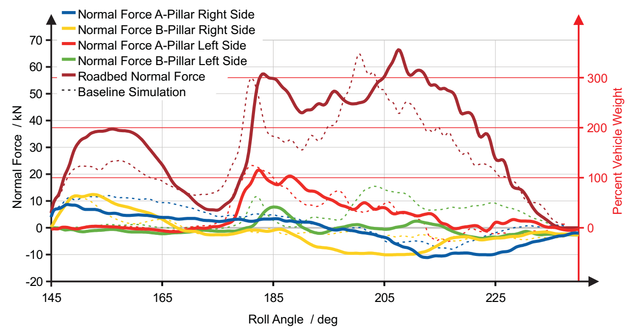

Graph D.72: Section forces (JRS rollover test) of roll cage, 2 mm simulation, without rollcage

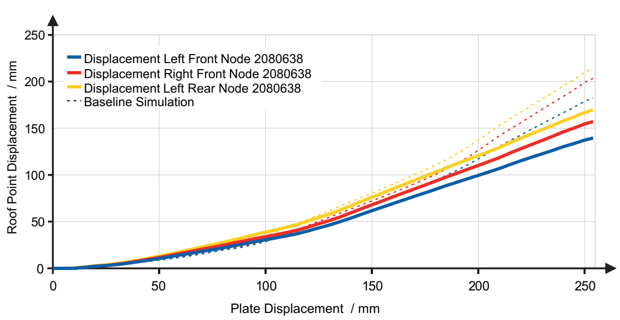

Graph D.73: Dummy head point displacement (static roof crush test) of roll cage, 2 mm simulation

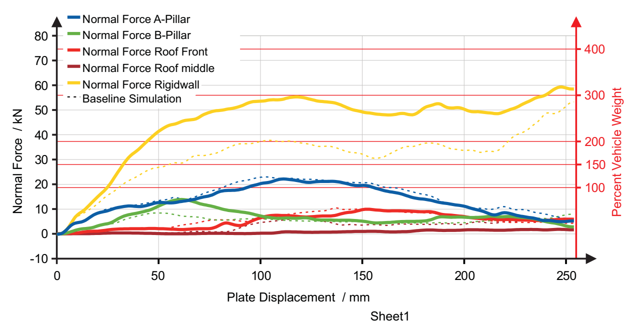

Graph D.74: Section forces (static roof crush test) of roll cage, 2 mm simulation, without rollcage

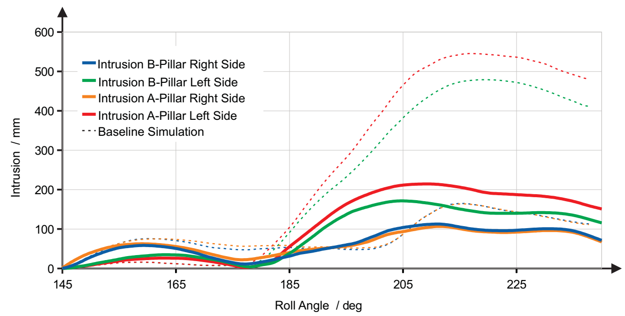

Graph D.75: Roof intrusion (JRS rollover test) of roll cage, 4 mm simulation

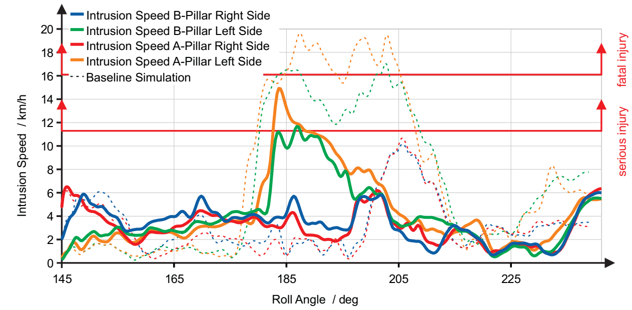

Graph D.76: Roof intrusion velocity (JRS rollover test) of roll cage, 4 mm simulation

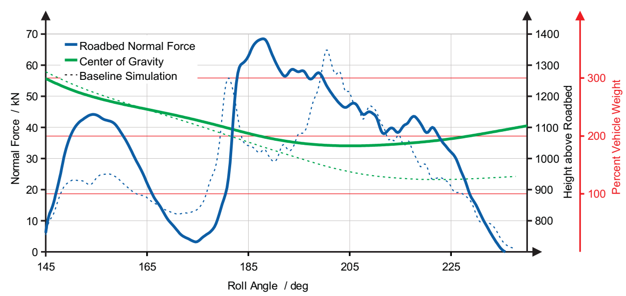

Graph D.77: Roadbed load and center of gravity (JRS rollover test) of roll cage, 4 mm simulation

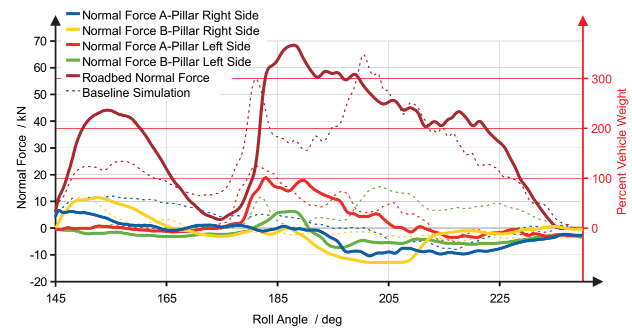

Graph D.78: Section forces (JRS rollover test) of roll cage, 4 mm simulation, without rollcage

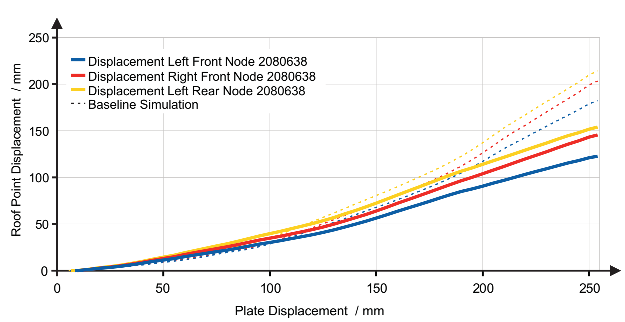

Graph D.79: Dummy head point displacement (static roof crush test) of roll cage, 4 mm simulation

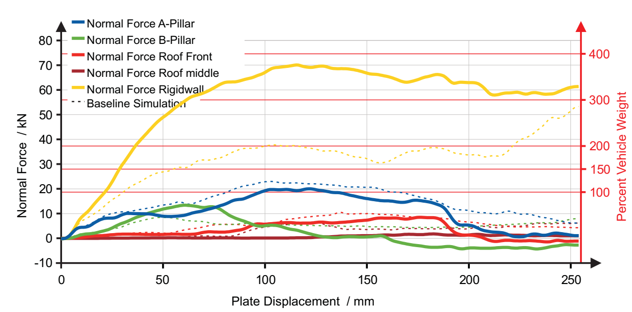

Graph D.80: Section forces (static roof crush test) of roll cage, 4 mm simulation, without rollcage

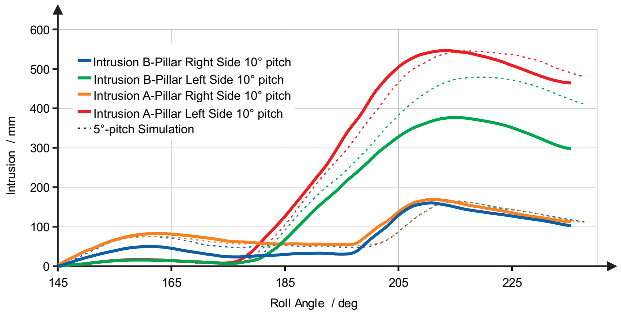

Graph D.81: Roof intrusion comparison of 10°-pitch JRS rollover baseline simulation

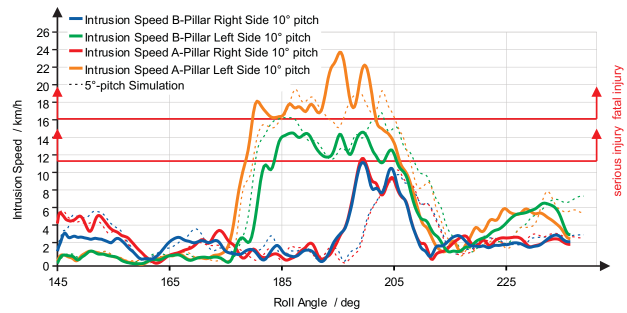

Graph D.82: Roof intrusion velocity comparison of 10°-pitch JRS rollover baseline simulation

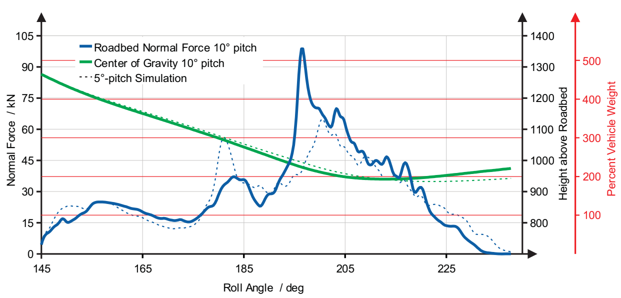

Graph D.83: Roadbed load and center of gravity comparison of 10°-pitch JRS rollover baseline simulation

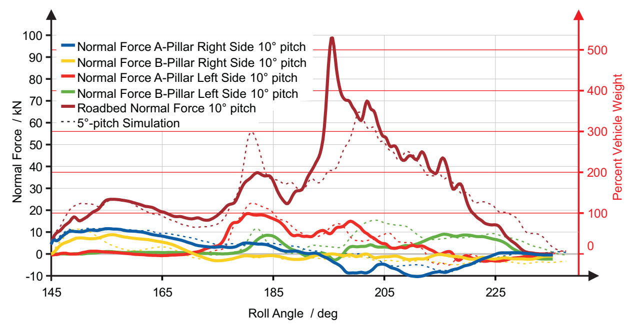

Graph D.84: Section forces comparison of 10°-pitch JRS rollover baseline simulation

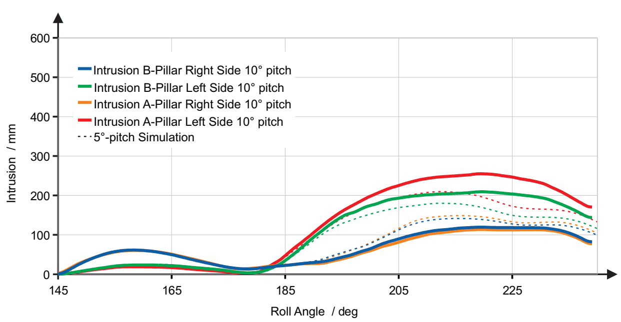

Graph D.85: Roof intrusion comparison of 10°-pitch JRS rollover reinforced simulation

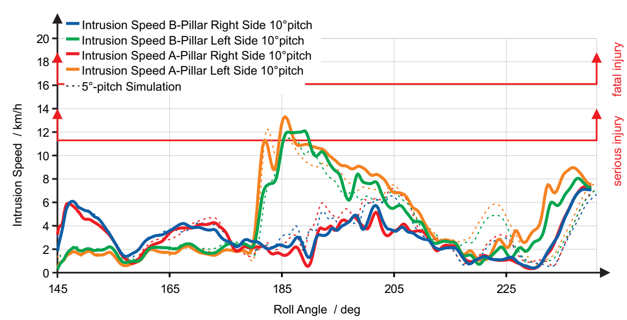

Graph D.86: Roof intrusion velocity comparison of 10°-pitch JRS rollover reinforced simulation

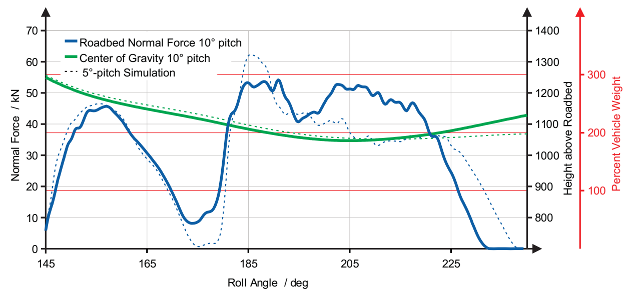

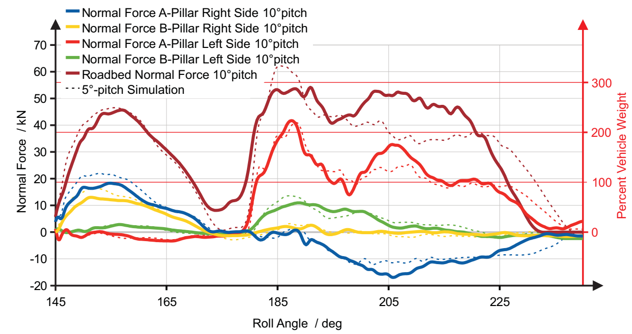

Graph D.87: Roadbed load and center of gravity comparison of 10°-pitch JRS rollover reinforced simulation

Graph D.88: Section forces comparison of 10°-pitch JRS rollover reinforced simulation

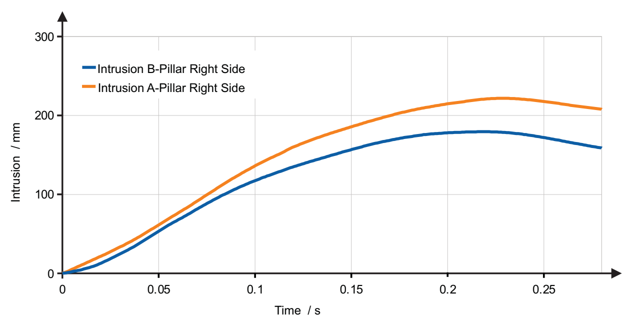

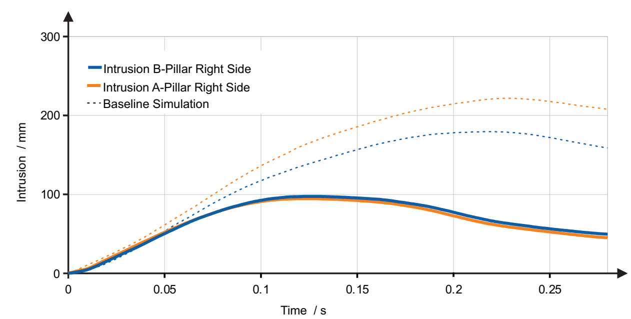

Graph D.89: Drop test simulation intrusion, baseline simulation

Graph D.90: Drop test simulation intrusion, A-/B-pillar + window header reinforced simulation

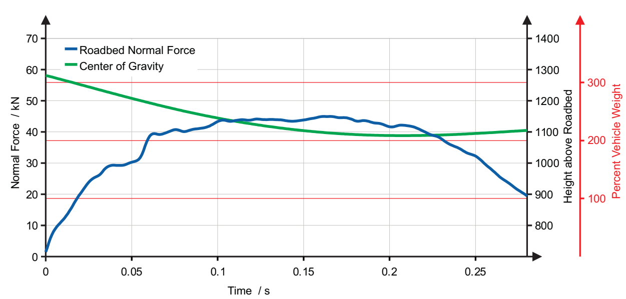

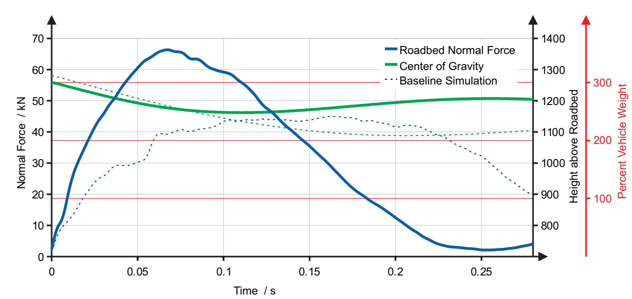

Graph D.91: Roadbed load and center of gravity plot of baseline drop test simulation

Graph D.92: Roadbed load and center of gravity plot of A-/B-pillar + window header reinforced drop test simulation